University of Maribor Press

ISSN 1854-0171

ACTA GEOTECHNICA SLOVENICA

2019/2
VOL. 16

ISSN: 1854-0171

ACTA GEOTECHNICA SLOVENICA

Ustanovitelji | Founders

Univerza v Mariboru, Fakulteta za gradbeništvo, prometno inženirstvo in arhitekturo
University of Maribor, Faculty of Civil Engineering, Transportation Engineering and Architecture

Univerza v Ljubljani, Fakulteta za gradbeništvo in geodezijo
University of Ljubljana, Faculty of Civil and Geodetic Engineering

Univerza v Ljubljani, Naravoslovnotehniška fakulteta
University of Ljubljana, Faculty of Natural Sciences and Engineering

Slovensko geotehniško društvo
Slovenian Geotechnical Society

Društvo za podzemne in geotehniške konstrukcije
Society for Underground and Geotechnical Constructions

Izdajatelj | Publisher

Univerza v Mariboru, Fakulteta za gradbeništvo, prometno inženirstvo in arhitekturo
Faculty of Civil Engineering, Transportation Engineering and Architecture

Odgovorni urednik | Editor–in–Chief

Borut Macuh — University of Maribor

Tehnična urednica | Technical Editor

Tamara Bračko — University of Maribor

Uredniki | Co–Editors

Jakob Likar	Geoportal d.o.o.
Janko Logar	University of Ljubljana
Primož Jelušič	University of Maribor
Stanislav Škrabl	University of Maribor
Milivoj Vulić	University of Ljubljana
Bojan Žlender	University of Maribor

Posvetovalni uredniki | Advisory Editors

Heinz Brandl	Vienna University of Technology
Chandrakant. S. Desai	University of Arizona
Bojan Majes	University of Ljubljana
Pedro Seco e Pinto	National Laboratory of Civil Eng.

Lektor | Proof–Reader

Paul McGuiness

Naklada | Circulation

200 izvodov - issues

Cena | Price

25 EUR/letnik - 25 EUR/vol.; (50 EUR for institutions/za institucije)

Tisk | Print

Rolgraf

Revija redno izhaja dvakrat letno. Članki v reviji so recenzirani s strani priznanih mednarodnih strokovnjakov. Baze podatkov v katerih je revija indeksirana: SCIE - Science Citation Index Expanded, JCR – Journal Citation Reports / Science Edition, ICONDA - The international Construction database, GeoRef. Izid publikacije je finančno podprla Javna agencija za raziskovalno dejavnost Republike Slovenije iz naslova razpisa za sofinanciranje domačih periodičnih publikacij.

Založnik | Published by

Univerzitetna založba Univerze v Mariboru
Slomškov trg 15, 2000 Maribor, Slovenija
e-pošta: zalozba@um.si, http://press.um.si/, http://journals.um.si/

University of Maribor Press
Slomškov trg 15, 2000 Maribor, Slovenia
e-mail: zalozba@um.si, http://press.um.si/, http://journals.um.si/

Naslov uredništva | Address

ACTA GEOTECHNICA SLOVENICA
Univerza v Mariboru, Fakulteta za gradbeništvo, prometno inženirstvo in arhitekturo
Smetanova ulica 17, 2000 Maribor, Slovenija
Telefon / Telephone: +386 (0)2 22 94 300
Faks / Fax: +386 (0)2 25 24 179
E-pošta / E-mail: ags@um.si

Spletni naslov | web Address

http://zalozba.um.si/index.php/ags/index

The journal is published twice a year. Papers are peer reviewed by renowned international experts. Indexation data bases of the journal: SCIE - Science Citation Index Expanded, JCR – Journal Citation Reports / Science Edition, ICONDA- The international Construction database, GeoRef. The publication was financially supported by Slovenian Research Agency according to the Tender for co-financing of domestic periodicals.

UNDRAINED BEARING CAPACITY OF A SKIRTED STRIP FOUNDATION USING UPPER-BOUND LIMIT ANALYSIS

NOSILNOST PASOVNIH TEMELJEV S KRILI V NEDRENIRANIH POGOJIH S POMOČJO ANALIZE ZGORNJE MEJNE VREDNOSTI

Priyanka Ghosh *(corresponding author)*
Indian Institute of Technology, Kanpur,
Department of Civil Engineering
Kanpur – 208 016, India
E-mail: priyog@iitk.ac.in

Alok Pal
Indian Institute of Technology, Kanpur,
Department of Civil Engineering
Kanpur – 208 016, India
E-mail: alok.besu2188@gmail.com

DOI https://doi.org/10.18690/actageotechslov.16.2.2-11.2019

Keywords

footings, limit analysis, plane strain, plasticity, skirted foundation

Ključne besede

temelji, mejna analiza, ravninsko deformacijski stanje, plastičnost, temelj s krili

Abstract

Skirted foundations are assumed to be a wise selection in offshore geotechnical engineering. In this paper the bearing-capacity factors for a vertically loaded skirted strip foundation resting on uniform c-ϕ soil were obtained using an upper-bound limit analysis. The analysis is performed by choosing a kinematically admissible failure mechanism comprising multiple triangular rigid blocks. The effect of the embedment depth of the skirts on the bearing capacity is studied based on the dimensionless embedment ratio D_f/B_f. A detailed parametric study is carried out by varying the D_f/B_f ratio and ϕ for both the smooth and rough surface of the skirts. The results obtained from the present theoretical analysis are compared with the available theoretical and experimental data reported in the literature.

Izvleček

V geotehničnem inženirstvu na morju so temelji s krili praviloma primeren izbor temeljenja. V tem prispevku smo s pomočjo analize zgornje mejne vrednosti določili faktorje nosilnosti za vertikalno obremenjen pasovni temelj na enakomerni c-ϕ zemljini. Analiza je izvedena z izbiro kinematično dopustnega porušnega mehanizma, ki je sestavljen iz več trikotnih togih blokov. Vpliv globine vpetja kril na nosilnost je preučevana na podlagi brezdimenzijskega razmerja vpetosti, D_f/B_f. Izvedena je bila podrobna parametrična študija s spreminjanjem razmerja D_f/B_f in ϕ za gladko in grobo površino kril. Rezultati, dobljeni na osnovi predlagane teoretične analize, so bili primerjani z razpoložljivimi teoretičnimi in eksperimentalnimi podatki, ki so navedeni v literaturi.

List of symbols:

B_f	width of the skirted strip foundation
D_f	embedment depth of the skirts
D_f/B_f	non-dimensional embedment ratio
N_{csk}	bearing-capacity factor for an isolated skirted strip foundation with respect to the cohesion of the soil
N_γ	bearing-capacity factor for surface strip foundation with respect to the unit weight of the soil
$N_{\gamma sk}$	bearing-capacity factor for an isolated skirted strip foundation with respect to the unit weight of the soil
P_{usk}	ultimate failure load of the skirted foundation
V_i	absolute velocity of the i^{th} triangular rigid block in the radial shear zone of the skirted foundation

$V_{i,i+1}$	velocity of the block i+1 relative to the block i in the radial shear zone of the skirted foundation
l_i, d_i	length of two arms of the i^{th} triangular rigid block in the radial shear zone of the skirted foundation
n	number of triangular rigid blocks in the radial shear zone of the skirted foundation
q_{usk}	ultimate bearing capacity of the skirted foundation
α_i, β_i	internal angles of the i^{th} triangular rigid block in the radial shear zone of the skirted foundation
α^a	adhesion factor for the soil
ϕ	angle of internal friction of the soil

1 INTRODUCTION

To improve the bearing-capacity and reduce settlement, skirted foundations are reported as a popular choice in geotechnical engineering. The skirts provide confinement in which the soil is stringently enclosed and perform as a single unit with the overlain foundation to transmit the superstructure load to the soil essentially at the level of the skirt tip. Skirted foundations are generally installed to increase the effective depth of the offshore foundation where scouring seems, by all accounts, to be a noteworthy concern [1-4]. Besides that, for several coastal and near-shore structures resting on granular soils with high water tables as well as for the enhancement of the bearing capacity under normal situations, skirted foundations can be an economical option. The major application of skirted foundations is affiliated with jack-up unit structures, oil and petrol gas plants, tension leg platforms, wind-turbine foundations, bridge foundations, etc. Several studies [2-21] are available to determine the bearing capacity of the skirted foundation assuming a rigid soil plug within the skirts. Having considered an equivalent embedded rigid foundation, Yun and Bransby [21] determined the bearing capacity of the skirted foundation embedded in uniform soil. The soil plug is generally presumed to act as a rigid body with uniform shear strength along the depth [14]. Keawsawasvong and Ukritchon [2] and Ukritchon and Keawsawasvong [3] determined the undrained pullout capacity of suction caissons using both upper- and lower-bound limit analyses. A number of investigations [22-28] reported in the literature address the bearing-capacity aspect of the foundation under different field conditions using various solution techniques, such as upper- and lower-bound limit analyses, and finite-element analysis. However, the few studies [13, 21] available in the literature are restricted to the experimental investigation of the skirted foundation considering the plane-strain condition and a perfectly rough foundation-soil interface. Finite-element analyses were performed by Mana et al. [14] to determine the bearing capacity of a circular skirted foundation as a function of the skirt depth, the foundation-soil interface roughness and the heterogeneity in soil strength. However, except for a few studies on suction caissons [2-4], no work is available in the literature to understand the failure of the skirted foundation through a kinematically admissible collapse mechanism along with a properly defined velocity field under the framework of a limit analysis. Therefore, there is an obvious need to develop a proper failure mechanism for exploring the bearing capacity of a skirted foundation theoretically.

This study aims to determine the bearing capacity of a skirted strip foundation resting on a homogeneous soil deposit using upper-bound limit analysis [2-3, 22]. The upper-bound theorem, which assumes a perfectly plastic soil model with an associated flow rule, states that the rate of internal energy dissipation by any kinematically admissible velocity field can be equated with the rate of work done by external forces to enable a strict upper bound on the true limit load [29]. In association with the collapse mechanism similar to Pal et al. [17], a multi-block failure mechanism along with upper-bound limit analysis has been adopted to determine the bearing-capacity factors. The bearing-capacity factors with respect to the cohesion (N_{csk}) and unit weight (N_{ysk}) of the soil are obtained using a kinematically admissible velocity field. Both smooth and rough skirts are considered in the analysis. The effect of the skirt depth on the bearing capacity is studied based on the dimensionless embedment ratio. The results obtained from the analysis are suitably compared with the available data reported in the literature.

2 PROBLEM DEFINITION

A single, isolated, skirted strip foundation with width B_f and depth of skirts D_f rests on a uniform c-ϕ soil deposit. The objective is to determine the bearing-capacity factors N_{csk} and N_{ysk} considering an upper-bound limit analysis along with a multi-block failure mechanism. The collapse mechanism, as shown in Fig. 1, is supposed to determine the bearing-capacity factors for the skirted foundation. It is assumed: 1) foundation, skirt and connection between the foundation and the skirt behave as a rigid structure; 2) the analysis does not consider the effect of the installation of the skirted foundation on the surrounding soil; 3) the behavior of the soil is considered to be pressure independent, i.e., the undrained condition.

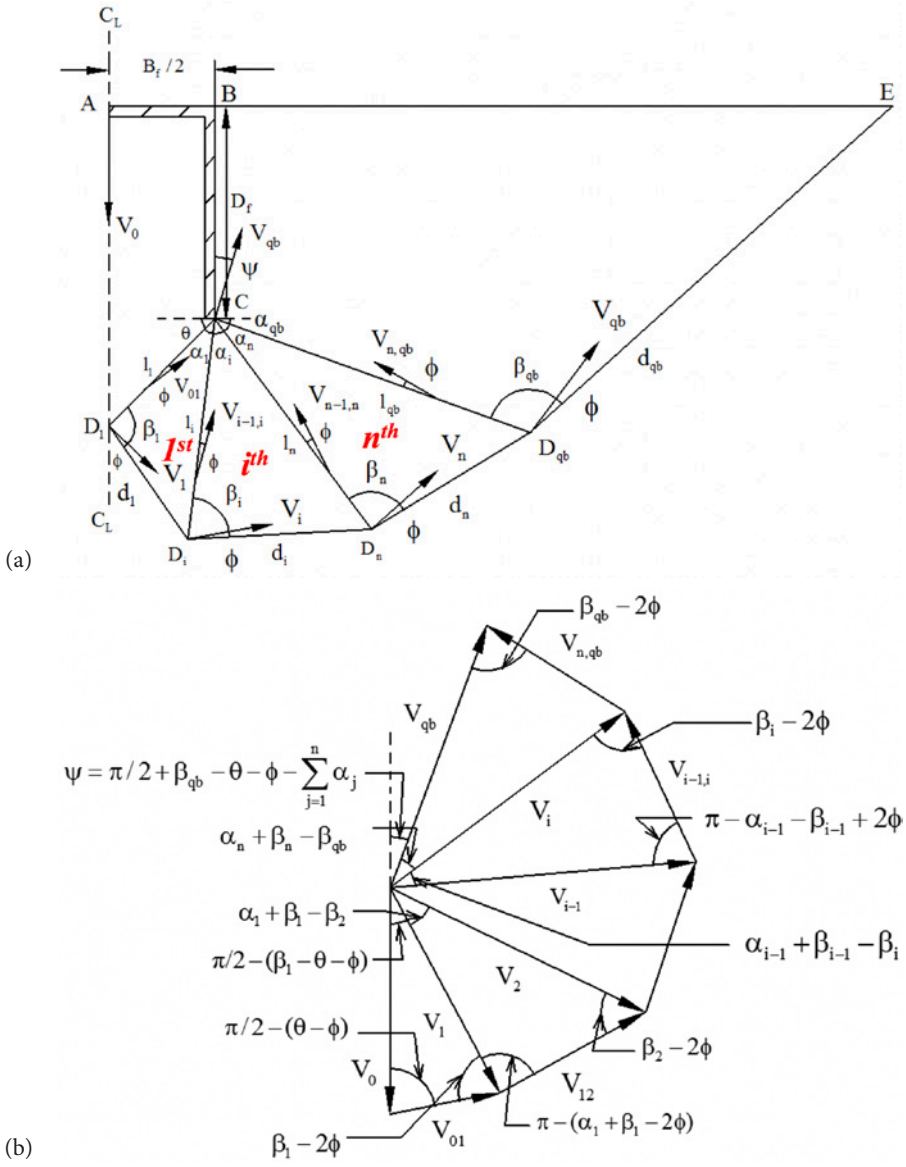

Figure 1. (a) Geometry of rigid blocks and velocity vectors, (b) velocity hodograph for failure mechanism.

3 FAILURE MECHANISM

The collapse mechanism, as shown in Fig. 1a, is a kinematically admissible, symmetrical, multi-block failure mechanism with three kinematic variables (α_i, β_i and θ) to define the collapse mechanism. For the sake of clarity, only the right portion of the center line of the foundation is shown in Fig. 1a, where AB and BC are the half width of the foundation and the right skirt, respectively. The wedge $ABCD_1$ is assumed to move vertically as a rigid body with the same downward velocity V_0 as that of the footing. The downward movement of the footing and the wedge $ABCD_1$ is accommodated by a lateral movement of the adjacent two radial shear zones on both the left and right sides. The radial shear zones on the right side $CD_1D_2\ldots D_i\ldots D_nD_{qb}C$ are discretized into n number of triangular rigid blocks along with the last quadrilateral rigid block $BCD_{qb}E$. The wedge $ABCD_1$ includes a part of the soil plug formed between two skirts (left and right) and the triangular wedge shaped below the skirts, which makes an angle θ with the horizontal. Each triangular rigid block within the radial shear zone can be defined by the internal angles α_i and β_i, and by two arms l_i and d_i, whereas the last quadrilat-

eral rigid block, $BCD_{qb}E$ can be defined by the angles $(\pi/2 + \alpha_{qb})$ and β_{qb}, and the arm length l_{qb}, where $l_{qb} = CD_{qb}$. The velocity hodograph for the failure mechanism and other associated geometric parameters are shown in Fig. 1b.

At collapse, it is assumed that the footing and the underlying rigid block $ABCD_1$ move as a single rigid unit in the vertical direction with a velocity V_0. The number (n) of triangular rigid blocks is kept equal to 30 based on the convergence study. $V_1, V_2, \ldots V_i \ldots V_n$ are the absolute velocities of all the triangular rigid blocks within the radial shear zone, whereas V_{01} is the velocity of the block CD_1D_2 relative to the block $ABCD_1$; $V_{i,i+1}$ is the velocity of the block i+1 relative to the block i and so on. The interfaces of all the triangular blocks are treated as the velocity-discontinuity lines. The soil mass is assumed to obey the Mohr–Coulomb failure criterion and an associated flow rule. Hence, the direction of the velocity vectors $V_1, V_2, \ldots V_i \ldots V_n$ makes an angle ϕ with the corresponding rupture lines. The relative velocities $V_{01}, V_{12}, \ldots V_{i-1,i} \ldots V_{n-1,n}$ are also inclined at an angle ϕ with the velocity discontinuity lines $CD_1, CD_2 \ldots CD_i \ldots CD_n$, respectively. The quadrilateral block moves with an absolute velocity V_{qb}, , which makes an angle ϕ with $D_{qb}E$ and an angle $\psi = \left(\frac{\pi}{2} + \beta_{qb} - \theta - \phi - \sum_{j=1}^{n} \alpha_j\right)$ with the skirt BC, as shown in Fig. 1b. It is worth noting that in the presence of soil cohesion, an adhesion factor (α^a) is assumed to determine the internal energy dissipation along the skirt surface, which ensures no separation between the skirt and the soil. All the velocities can be computed in terms of V_0 following the velocity hodograph, as shown in Fig. 1b.

4 ANALYSIS

Various parameters along with the velocity vectors associated with the radial shear zone around the edge of the foundation can be obtained following the collapse mechanism as well as the velocity hodograph. The magnitude of P_{usk} can be obtained by equating the total external work done to the total internal dissipation of energy, which in turn determines the ultimate bearing capacity of the skirted foundation, $q_{usk} = P_{usk}/B_f$. The work done by various external forces and the internal dissipation of energy along the lines of discontinuity can be obtained by following the equations provided in Appendix I and II, respectively. Among the various possible solutions obtained with different input parameters, the least upper-bound value of P_{usk} reveals the target solution. Hence, the objective function (the bearing capacity) is optimized with respect to different variables (geometrical parameters of the failure mechanism) to obtain the minimum value of the bearing capacity and can be expressed as

$$q_{usk} = \frac{P_{usk}}{B_f} = cN_{csk} + 0.5\gamma B_f N_{\gamma sk} \qquad (1)$$

The bearing-capacity factors for the smooth skirts can be expressed as

$$N_{\gamma sk} = -(f_1 + f_2 + f_3 + f_4 + f_5) \qquad (2a)$$

$$N_{csk} = (f_6 + f_7 + f_8 + f_9 + f_{10}) \qquad (2b)$$

where the functions $f_1 - f_{10}$ are defined in Appendix I and II. However, for a detailed formulation of these functions, Chen [29] can be referred to.

Similarly, the bearing-capacity factors for the rough skirts can be expressed as

$$N_{\gamma sk} = -(f_1 + f_2 + f_3 + f_4 + f_5) \qquad (3a)$$

$$N_{csk} = (f_6 + f_7 + f_8 + f_9 + f_{10} + f_{11}) \qquad (3b)$$

where the function f_{11} is defined in Appendix II.

From Eqs. (2) and (3) it can be observed that $N_{\gamma sk}$ is same for the foundation with smooth as well as rough skirts, whereas N_{csk} varies with the roughness of the skirts. The method of superposition is employed to determine the bearing-capacity factor for the skirted foundation i.e., the $c = 0$, $\gamma \neq 0$ condition is considered to determine $N_{\gamma sk}$; whereas N_{csk} is obtained by considering the $c \neq 0$, $\gamma = 0$ condition and hence, in the process, a true upper-bound solution might not be guaranteed. The minimum value of the bearing capacity, q_{usk} is obtained after performing a nonlinear constrained optimization of Eq. (1) with the help of the 'fmincon' solver in MATLAB.

The constraints considered in the optimization process are

a) $\theta + \sum_{j=1}^{n+1} \alpha_j + \alpha_{qb} = \pi$, which is based on the geometry of the failure mechanism.

b) $\alpha_i + \beta_i > \beta_{i+1}$, which ensures a kinematically admissible failure mechanism.

c) $\alpha_i + \beta_i < \pi$, which ensures that all the rigid blocks within the radial shear zone are triangular.

d) $10° < \theta < 85°$, $1° < \alpha_i < 85°$, $10° < \beta_i < 170°$, which are the upper and lower limits of the parameters θ, α_i and β_i.

e) $V_i > 0$ and $V_{i-1} < V_i$, which ensure that all the velocity vectors are positive and the collapse mechanism is kinematically admissible.

5 RESULTS AND DISCUSSION

5.1 Smooth and rough skirts

The variation of N_{csk} with D_f/B_f for both smooth and rough skirts is shown in Fig. 2 for different values of α^a and ϕ. For smooth skirts, there is no energy dissipation along the skirts; whereas in the case of rough skirts the magnitude of N_{csk} depends on the adhesion factor α^a, which is varied from 1/3 to 1.0. From Fig. 2 it is clear that the magnitude of N_{csk} increases with an increase in the D_f/B_f ratio for a particular value of ϕ. It can also be observed that the value of N_{csk} increases as the roughness of the skirts i.e., the adhesion factor (α^a), increases. However, for a lower embedment ratio (D_f/B_f) the roughness of the skirts has little influence on N_{csk}. Hence, it is evident from Fig. 2 that the effectiveness of the skirted foundation increases with an increase in the embedment depth of the skirt.

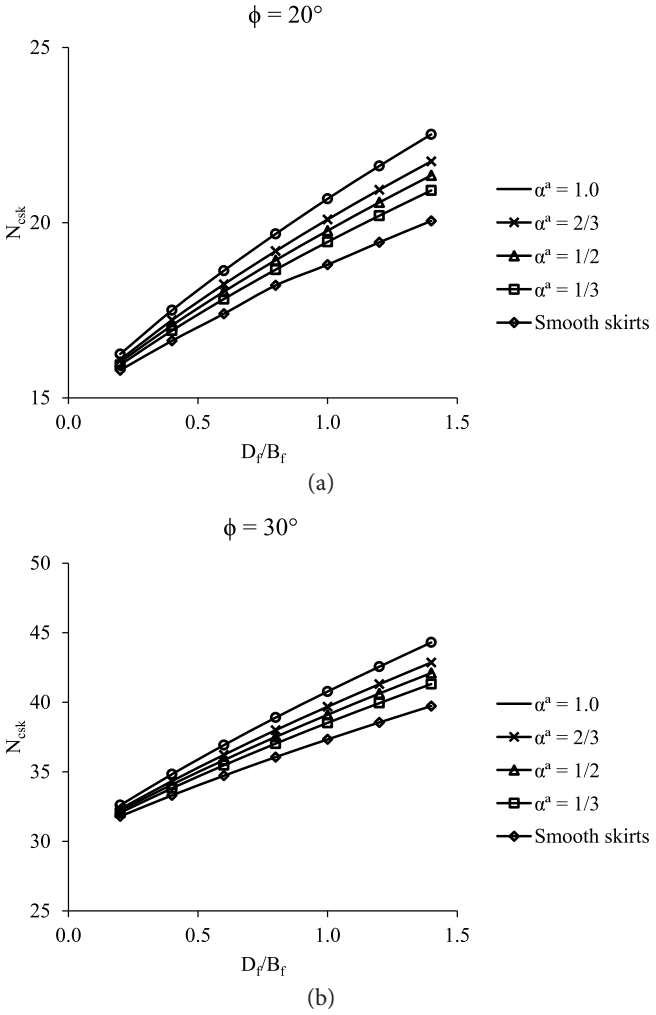

Figure 2. (a) Variation of N_{csk} with D_f/B_f with different α^a for (a) $\phi = 20°$, (b) $\phi = 30°$.

The variation of N_{ysk} with D_f/B_f for different values of ϕ is shown in Fig. 3. The magnitude of N_{ysk} is found to increase significantly with the D_f/B_f ratio due to an increase in the confinement provided by the skirts. The roughness of the skirts does not affect the bearing-capacity factor N_{ysk} as the internal energy dissipation is considered to be zero ($c = 0$) in the determination of N_{ysk}. The rate of increase of N_{ysk} is seen to be more predominant in the case of a higher angle of internal friction, which can be attributed to the larger failure domain developed in the surrounding soil.

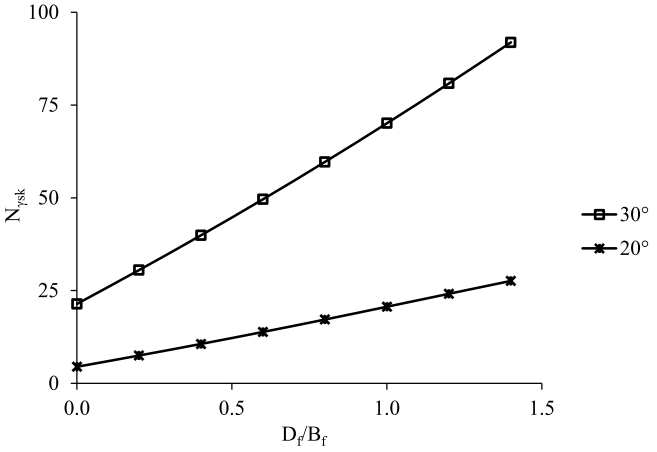

Figure 3. Variation of N_{ysk} with D_f/B_f for different values of ϕ.

5.2 Critical failure surface

The critical failure surface obtained from the optimization of the collapse mechanism is shown in Fig. 4 for $\phi = 30°$ and different D_f/B_f ratios. It is clear that the size of the critical failure zone considerably increases with an increase in the D_f/B_f ratio, which in turn causes an increase in the bearing capacity of the skirted foundation. Similarly, the critical failure surface for different values of α^a and ϕ is presented in Figs. 5 and 6, respectively. It is clear from Figs. 5 and 6 that the failure zone expands with an increase in α^a and ϕ, resulting in an enhancement of the bearing capacity with an increasing roughness of the skirts and the angle of internal friction of the surrounding soil.

6 COMPARISON

In Table 1 the present values of N_{csk} obtained for smooth skirts with $\phi = 0°$ are compared with those reported by Mana et al. [15], who obtained N_{csk} for the foundation with smooth skirts employing finite-element limit

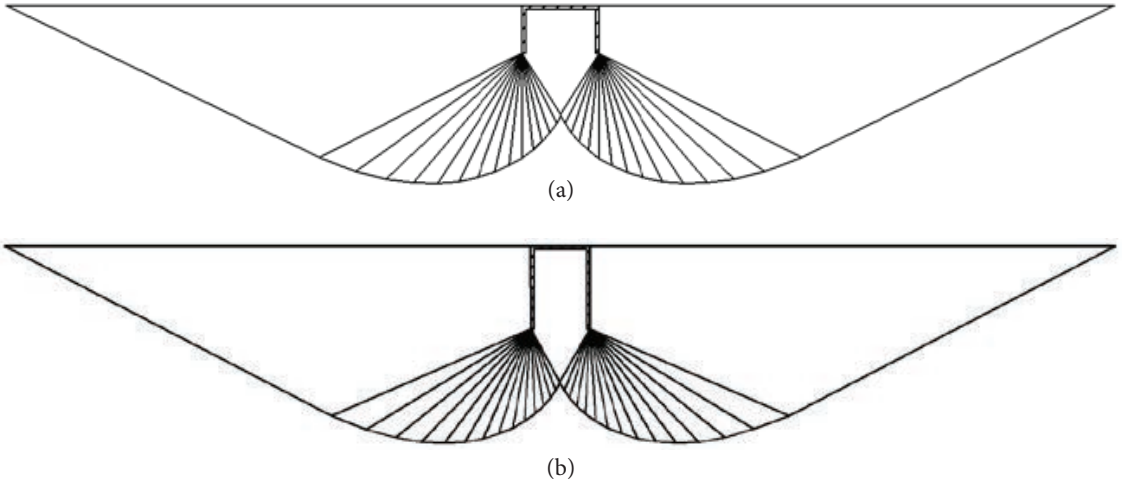

Figure 4. Critical collapse surface for $\phi = 30°$ and $\alpha^a = 1.0$ with (a) $D_f/B_f = 0.6$, (b) $D_f/B_f = 1.4$.

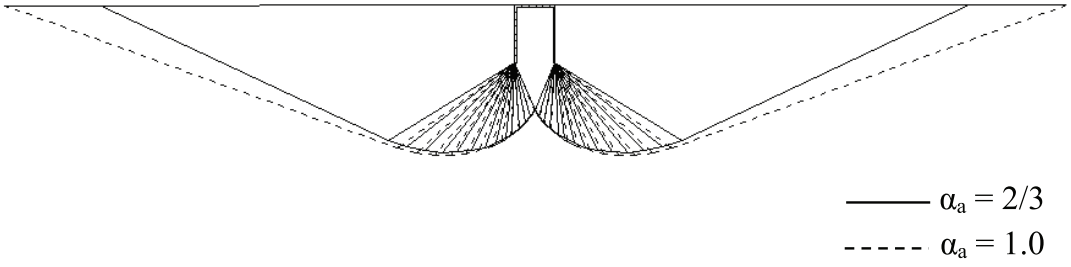

Figure 5. Critical collapse surface for $\phi = 30°$and $D_f/B_f = 1.4$ with different α^a.

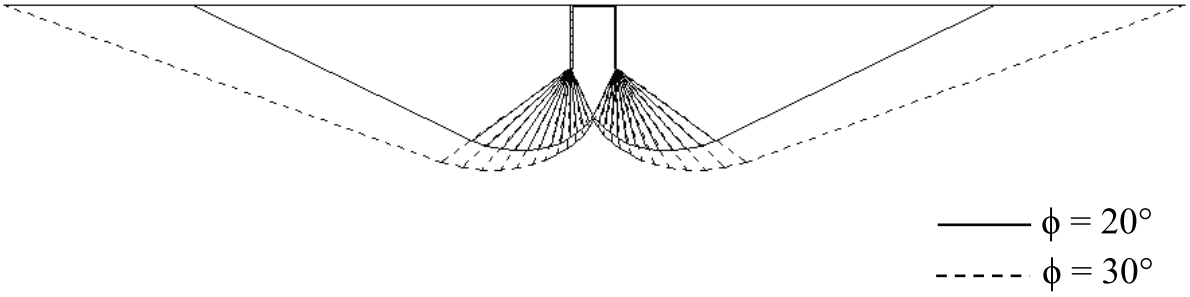

Figure 6. Critical collapse surface for $\alpha^a = 1.0$ and $D_f/B_f = 1.4$ with different ϕ.

analysis. The present results are found to be the lowest, but compare reasonably well with those proposed by Mana et al. [15]. In Table 2, the values of N_{csk} obtained from the present analysis for rough skirts with $\phi = 0°$ are compared with those provided by Yun and Bransby [21] and Mana et al. [14]. The latter determined the bearing-capacity of a skirted strip foundation resting on uniform clay soil ($\phi = 0°$) using the finite-element method. The present analysis predicts a lower value of N_{csk} as compared with the existing values reported in the literature and hence it can be considered as a better solution for the skirted foundation.

In Table 3, the ratio of N_{ysk}/N_γ obtained from the present analysis for different magnitudes of the D_f/B_f ratio is compared with the numerical as well as the experimental results reported by Eid [11]. Eid [11] proposed the N_{ysk}/N_γ ratio in cohesionless soil through experimental

Table 1. Comparison of N_{csk} for smooth skirts with $\phi = 0°$.

D_f/B_f	Present analysis	Mana et al. [15]
0.1	5.33	5.48
0.2	5.50	5.74
0.3	5.63	5.92
0.4	5.77	6.10
0.5	5.90	6.22

Table 2. Comparison of N_{csk} for rough skirts with $\phi = 0°$.

D_f/B_f	Present analysis	Yun and Bransby [21]	Mana et al. [14]
0.00	5.14	5.20	5.22
0.20	5.65	6.00	6.10
0.30	5.86	6.35	6.50
0.50	6.23	7.00	7.25
0.75	6.62	7.70	8.00
1.00	6.95	8.50	8.80
1.20	7.19	9.00	-

Table3. Comparison of N_{ysk}/N_γ ratio for different D_f/B_f.

ϕ(°)	D_f/B_f	N_{ysk}/N_γ		
		Present analysis	Eid [11]	
			Numerical	Experimental
35.0	0.5	1.87	1.5	-
	1.0	2.80	1.8	-
	1.5	3.81	2.6	-
	2.0	4.88	3.2	-
38.5	0.5	1.74	-	2.10
	1.0	2.52	-	3.10
	1.5	3.36	-	4.05
	2.0	4.25	-	5.50
40.0	0.5	1.70	1.4	1.85
	1.0	2.41	2.1	2.60
	1.5	3.18	2.6	3.50
	2.0	4.00	3.2	4.70
45.0	0.5	1.53	1.6	1.50
	1.0	2.10	2.2	2.20
	1.5	2.66	2.7	2.95
	2.0	3.27	3.3	4.00

as well as numerical analyses. Three different values of relative density (44%, 57% and 71%) were considered in the experimental study of Eid [11], which correspond to three different magnitudes of ϕ , such as 38.5°, 40° and 45° [30]. It is worth noting that the corresponding value of ϕ is selected as the mean value within the range of ϕ as proposed by Eid et al. [30]. For lower values of ϕ, the present values of the N_{ysk}/N_γ ratio are seen to be a little higher than those determined from the numerical study of Eid [11], whereas the experimental results of Eid [11] for all values of ϕ are the highest.

7 CONCLUSIONS

The bearing-capacity factors for a skirted strip foundation are determined using an upper-bound limit analysis for various soil-friction angles and the embedment ratio of the skirts. The magnitude of N_{csk} is found to increase with an increase in the roughness of the skirts. However, for a lower value of the D_f/B_f ratio, the roughness of the skirts has little influence on the N_{csk} values. It was clear that the magnitude of N_{csk} increases with an increase in the D_f/B_f ratio for a particular value of ϕ. The magnitude of N_{ysk} was found to increase significantly with theD_f/B_f ratio due to an increase in the confinement provided by the skirts. The roughness of the skirts does not affect N_{ysk} as the internal energy dissipation is considered to be zero ($c = 0$) during the calculation of N_{ysk}.

APPENDIX I: EXTERNAL WORK DONE

a) The external work done by the self-weight of the quadrilateral block $ABCD_1$ below the footing (Fig. 1a) can be expressed as,

$$\Delta W_{ABCD_1} = \frac{\gamma B_f^{\,2}}{2}[f_1(\alpha_i, \beta_i, \theta)]V_0 \qquad (4)$$

where,

$f_1 = \frac{\tan\theta}{2} + 2\left(\frac{D_f}{B_f}\right)$

b) The external work done by the self-weight of the $2n$ triangular rigid blocks on either side of the footing can be expressed as,

$$\sum_{j=1}^{2n}[\Delta W]_j = \frac{\gamma B_f^{\,2}}{2}[f_2(\alpha_i, \beta_i, \theta)]V_0 \qquad (5)$$

where,

$$f_2 = \frac{\cos(\theta-\phi)}{2\cos^2\theta\sin(\beta_1-2\phi)}\sum_{i=1}^{n}\left[\frac{\sin\alpha_i\sin\beta_i}{\sin(\alpha_i+\beta_i)}\right.$$

$$\left.\sin\left(\beta_i-\theta-\phi-\sum_{j=1}^{i-1}\alpha_j\right)\prod_{j=1}^{i-1}\frac{\sin^2\beta_j}{\sin^2(\alpha_j+\beta_j)}\frac{\sin(\alpha_j+\beta_j-2\phi)}{\sin(\beta_{j+1}-2\phi)}\right]$$

c) The external work done by the self-weight of the quadrilateral rigid block $BCD_{qb}E$ (Fig. 1a) can be expressed as,

$$\Delta W_{qb} = \frac{\gamma B_f^{\,2}}{2}[f_3(\alpha_i, \beta_i, \theta) + f_4(\alpha_i, \beta_i, \theta) + f_5(\alpha_i, \beta_i, \theta)]V_0 \quad (6)$$

where,

$$f_3 = \left[\frac{cos(\theta-\phi)\, sin\,\alpha_{qb}\, sin\,\beta_{qb}}{2\, cos^2\theta\, sin(\alpha_{qb}+\beta_{qb})\, sin(\beta_1-2\phi)}\right.$$
$$\left. sin\left(\beta_{qb}-\theta-\phi-\sum_{j=1}^{n}\alpha_j\right)\prod_{j=1}^{n}\frac{sin^2\beta_j\, sin(\alpha_j+\beta_j-2\phi)}{sin^2(\alpha_j+\beta_j)\, sin(\beta_{j+1}-2\phi)}\right]$$

$$f_4 = \left[\frac{2D_f}{B_f}\frac{cos(\theta-\phi)\, sin\,\beta_{qb}}{cos\,\theta\, sin(\beta_1-2\phi)\, sin(\alpha_{qb}+\beta_{qb})}\right.$$
$$\left. sin\left(\beta_{qb}-\theta-\phi-\sum_{j=1}^{n}\alpha_j\right)\prod_{j=1}^{n}\frac{sin\,\beta_j\, sin(\alpha_j+\beta_j-2\phi)}{sin(\alpha_j+\beta_j)\, sin(\beta_{j+1}-2\phi)}\right]$$

$$f_5 = \left[\frac{2D_f^{\,2}}{B_f^{\,2}}\frac{cos(\theta-\phi)\, sin\left[(\alpha_{qb}+\beta_{qb})-\pi/2\right]}{sin(\beta_1-2\phi)\, sin(\alpha_{qb}+\beta_{qb})}\right.$$
$$\left. \cdot sin\left(\beta_{qb}-\theta-\phi-\sum_{j=1}^{n}\alpha_j\right)\prod_{j=1}^{n}\frac{sin(\alpha_j+\beta_j-2\phi)}{sin(\beta_{j+1}-2\phi)}\right]$$

d) The external work done by the foundation load P_{usk} can be expressed as,

$$\Delta W_f = P_{usk} V_0 \quad (7)$$

APPENDIX II: INTERNAL DISSIPATION OF ENERGY

Considering the complete failure mechanism, the internal dissipation of energy can be derived as follows

a) The internal dissipation of energy along the line of discontinuity CD_1 can be expressed as (Fig. 1a),

$$\Delta IWD_{CD_1} = cB_f[f_6(\alpha_i, \beta_i, \theta)]V_0 \quad (8)$$

where,

$$f_6 = \frac{cos\,\phi\, cos(\beta_1-\theta-\phi)}{cos\,\theta\, cos(\beta_1-2\phi)}$$

b) The internal dissipation of energy along d_i (i = 1, 2, 3…..n) can be expressed as,

$$\Delta IWD_d = cB_f[f_7(\alpha_i, \beta_i, \theta)]V_0 \quad (9)$$

where,

$$f_7 = \frac{cos(\theta-\phi)\, cos\,\phi}{cos\theta\, sin(\beta_1-2\phi)}$$
$$\sum_{i=1}^{n}\left[\frac{sin\alpha_i}{sin(\alpha_i+\beta_i)}\prod_{j=1}^{i-1}\frac{sin\,\beta_j}{sin(\alpha_j+\beta_j)}\frac{sin(\alpha_j+\beta_j-2\phi)}{sin(\beta_{j+1}-2\phi)}\right]$$

c) The internal dissipation of energy along l_i (i = 2, 3, 4….n) can be expressed as,

$$\Delta IWD_l = cB_f[f_8(\alpha_i, \beta_i, \theta)]V_0 \quad (10)$$

where,

$$f_8 = \frac{cos(\theta-\phi)\, cos\,\phi}{cos\theta\, sin(\beta_1-2\phi)}$$
$$\sum_{i=2}^{n+1}\left[\frac{sin(\beta_{i-1}-\beta_i+\alpha_{i-1})}{sin(\beta_i-2\phi)}\prod_{j=1}^{i-1}\frac{sin\,\beta_j}{sin(\alpha_j+\beta_j)}\prod_{j=1}^{i-2}\frac{sin(\alpha_j+\beta_j-2\phi)}{sin(\beta_{j+1}-2\phi)}\right]$$

d) The internal dissipation of energy along the discontinuity line $D_{qb}E$ for the last quadrilateral block (Fig. 1a) can be expressed as,

$$\Delta IWD_{D_{qb}E} = cB_f[f_9(\alpha_i, \beta_i, \theta) + f_{10}(\alpha_i, \beta_i, \theta)]V_0 \quad (11)$$

where,

$$f_9 = \frac{cos(\theta-\phi)\, cos\,\phi\, sin\,\alpha_{qb}}{cos\theta\, sin(\beta_1-2\phi)\, sin(\alpha_{qb}+\beta_{qb})}$$
$$\prod_{j=1}^{n}\frac{sin\,\beta_j}{sin(\alpha_j+\beta_j)}\frac{sin(\alpha_j+\beta_j-2\phi)}{sin(\beta_{j+1}-2\phi)}$$

$$f_{10} = \frac{2D_f}{B_f}\frac{cos(\theta-\phi)\, cos\,\phi}{sin(\beta_1-2\phi)\, sin(\alpha_{qb}+\beta_{qb})}\prod_{j=1}^{n}\frac{sin(\alpha_j+\beta_j-2\phi)}{sin(\beta_{j+1}-2\phi)}$$

e) The internal dissipation of energy along the skirts i.e., along BC (Fig. 1a), can be expressed as,

$$\Delta IWD_{BC} = cB_f[f_{11}(\alpha_i, \beta_i, \theta)]V_0 \quad (12)$$

where,

$$f_{11} = \alpha^a\frac{D_f}{B_f}\frac{cos(\theta-\phi)}{sin(\beta_1-2\phi)}$$
$$cos\left(\frac{\pi}{2}+\beta_{qb}-\theta-\phi-\sum_{j=1}^{n}\alpha_j\right)\prod_{j=1}^{n}\frac{sin(\alpha_j+\beta_j-2\phi)}{sin(\beta_{j+1}-2\phi)}$$

REFERENCES

[1] Alemi, M., Maia, R. 2018. Numerical simulation of the flow and local scour process around single and complex bridge piers. International Journal of Civil Engineering 16(5), 475-487. DOI: https://doi.org/10.1007/s40999-016-0137-8

[2] Keawsawasvong, S., Ukritchon, B. 2016. Finite element limit analysis of pullout capacity of planar caissons in clay. Computers and Geotechnics 75, 12-17. DOI: https://doi.org/10.1016/j.compgeo.2016.01.015

[3] Ukritchon, B., Keawsawasvong, S. 2016. Undrained pullout capacity of cylindrical suction caissons by finite element limit analysis. Computers

and Geotechnics 80, 301-311. DOI: https://doi.org/10.1016/j.compgeo.2016.08.019

[4] Ukritchon, B., Wongtoythong, P., Keawsawasvong, S. 2018. New design equation for undrained pullout capacity of suction caissons considering combined effects of caisson aspect ratio, adhesion factor at interface, and linearly increasing strength. Applied Ocean Research 75, 1-14. DOI: https://doi.org/10.1016/j.apor.2018.03.007

[5] Al-Aghbari, M.Y., Dutta, R.K. 2008. Performance of square footing with structural skirt resting on sand. Geomechanics and Geoengineering 3(4), 271–277. DOI: https://doi.org/10.1080/17486020802509393

[6] Al-Aghbari, M.Y., Zein, Y.E. 2004. Bearing capacity of strip foundations with structural skirts. Geotechnical and Geological Engineering 22(1), 43-57. DOI: 10.1023/B:GEGE.0000013997.79473.e0

[7] Azzam, W.R. 2015. Finite element analysis of skirted foundation adjacent to sand slope under earthquake loading. HBRC Journal, 11(2), 231-239. DOI: https://doi.org/10.1016/j.hbrcj.2014.04.001

[8] Bienen, B., Gaudin, C., Cassidy, M.J., Rausch, L., Purwana, O.A., Krisdani, H. 2012. Numerical modelling of a hybrid skirted foundation under combined loading. Computers and Geotechnics 45, 127-139. DOI: https://doi.org/10.1016/j.compgeo.2012.05.009

[9] Bransby, M.F., Randolph, M.F. 1998. Combined loading of skirted foundations. Géotechnique 48(5), 637–655. DOI: https://doi.org/10.1680/geot.1998.48.5.637

[10] Bransby, M.F., Randolph, M.F. 1999. The effect of embedment depth on the undrained response of skirted foundations to combined loading. Soils and Foundations 39(4), 19–33. DOI: https://doi.org/10.3208/sandf.39.4_19

[11] Eid, H.T. 2013. Bearing capacity and settlement of skirted shallow foundations on sand. International Journal of Geomechanics 13(5), 645–652. DOI: https://doi.org/10.1061/(ASCE)GM.1943-5622.0000237

[12] Gourvenec, S. 2008. Effect of embedment on the undrained capacity of shallow foundations under general loading. Géotechnique 58(3), 177–185. DOI: https://doi.org/10.1680/geot.2008.58.3.177

[13] Gourvenec. S., Barnett, S. 2011. Undrained failure envelope for skirted foundations under general loading. Géotechnique 61(3), 263–270. DOI: https://doi.org/10.1680/geot.9.T.027

[14] Mana, D.S.K., Gourvenec, S.M., Randolph, M.F. 2010. A numerical study of the vertical bearing capacity of skirted foundations. Proceeding of 2nd International Symposium on Frontiers in Offshore Geotechnics (ISFOG), Perth, Australia, pp. 433–438.

[15] Mana, D.S.K., Gourvenec, S., Martin, C.M. 2013. Critical skirt spacing for shallow foundations under general loading. Journal of Geotechnical and Geoenvironmental Engineering 139(9), 1554-1566. DOI: https://doi.org/10.1061/(ASCE)GT.1943-5606.0000882

[16] Martin, C.M. 2001. Vertical bearing capacity of skirted circular foundations on Tresca soil. Proceeding of 15th International Conference on Soil Mechanics and Geotechnical Engineering, Istanbul, Turkey, 1, pp. 743–746.

[17] Pal, A., Ghosh, P., Majumder, M. 2017. Interaction effect of two closely spaced skirted strip foundations in cohesionless soil using upper-bound limit analysis. International Journal of Geomechanics 17(2), 06016022. DOI: https://doi.org/10.1061/(ASCE)GM.1943-5622.0000755

[18] Punrattanasin, P., Izawa, J., Kusakabe, O., Murata, O., Koda, M., Nishioka, H. 2003. The behavior of sheet pile foundations on sand. Proceeding of British Geotechnical Association (BGA) International Conference on Foundations, T. A. Newson, ed., MPG Books, Bodmin, U.K., pp. 723–732.

[19] Punrattanasin, P., Gasaluck, W., Muktabhant, C., Angsuwotai, P., Patjanasuntorn, A. 2009. The effect of sheet pile length on the capacity of sheet pile foundation. Proceeding of 17th International Conference on Soil Mechanics and Geotechnical Engineering, Millpress Science Publishers, Rotterdam, Netherlands, 1, pp. 598–601.

[20] Villalobos, F., Byrne, B.W., Houlsby, G.T., Martin, C.M. 2003. Bearing capacity tests of scale suction caisson footings on sand: Experimental data. Data Rep. FOT005/1, Department of Engineering Science, University of Oxford, Oxford, U.K.

[21] Yun, G., Bransby, M.F. 2007. The undrained vertical bearing capacity of skirted foundations. Soils and Foundations 47(3), 493–505. DOI: https://doi.org/10.3208/sandf.47.493

[22] Ghosh, P. 2008. Upper bound solutions of bearing capacity of strip footing by pseudo-dynamic approach. Acta Geotechnica 3(2), 115 -123. DOI: https://doi.org/10.1007/s11440-008-0058-z

[23] Kaya, N., Ornek, M. 2013. Experimental numerical studies of T-shaped footings. Acta Geotechnica Slovenica 10(1), 43-58.

[24] Shukla, R.P., Jakka, R.S. 2017. Critical setback distance for a footing resting on slopes. Acta Geotechnica Slovenica 14(2), 19-31.

[25] Ukritchon, B., Keawsawasvong, S. 2016. A practical method for the optimal design of continuous foot-

ing using ant-colony optimization. Acta Geotechnica Slovenica 13(2), 45-55.

[26] Ukritchon, B., Keawsawasvong, S. 2017. Unsafe error in conventional shape factor for shallow circular foundations in normally consolidated clays. Journal of Geotechnical and Geoenvironmental Engineering 143(6), 02817001. DOI: https://doi.org/10.1061/(ASCE)GT.1943-5606.0001670

[27] Ukritchon, B., Keawsawasvong, S. 2018. Lower bound limit analysis of an anisotropic undrained strength criterion using second-order cone programming. International Journal for Numerical and Analytical Methods in Geomechanics 42(8), 1016-1033. DOI: https://doi.org/10.1002/nag.2781

[28] Ukritchon, B., Yoang, S., Keawsawasvong, S. 2018. Bearing capacity of shallow foundations in clay with linear increase in strength and adhesion factor. Marine Georesources and Geotechnology 36(4), 438-451. DOI: 10.1080/1064119X.2017.1326991

[29] Chen, W.F. 1975. Limit analysis and soil plasticity. Elsevier, Amsterdam, Netherland.

[30] Eid, H.T., Alansari, O.A., Odeh, A.M., Nasr, M.N., Sadek, H.A. 2009. Comparative study on the behavior of square foundations resting on confined sand. Canadian Geotechnical Journal 46(4), 438–453. DOI: https://doi.org/10.1139/T08-134

SEISMIC ACTIVE EARTH PRESSURE ON RIGID RETAINING WALLS UNDER ROTATION ABOUT BASE CONSIDERING PRINCIPAL-STRESS ROTATIONS BY PSEUDO-STATIC METHODS

SEIZMIČNI AKTIVNI ZEMELJSKI PRITISK NA TOGE PODPORNE STENE OB ROTACIJI OKOLI OSNOVE OB UPOŠTEVANJU ROTACIJE GLAVNE NAPETOSTI S PSEVDO-STATIČNO METODO

Yan-Yan Cai
Fujian Research Center for Tunneling and Urban Underground Space Engineering, Huaqiao University, No. 668 Jimei Road, Xiamen 361021, China
State Key Laboratory of Geohazard Prevention and Geoenvironment Protection, Chengdu University of Technology, No.1 Erxianqiao Road, Chengdu 610059, China
E-mail: yycai@hqu.edu.cn

Yi-Tao Zhou *(corresponding author)*
Hebei University of Water Resources and Electric Engineering, School of Civil Engineering
No.1 Chongqing Road, Cangzhou 061001, China
E-mail: zhouytwr@163.com

Wen-Ping Zhang
Huaqiao University,
School of Civil Engineering
No. 668 Jimei Road., Xiamen 361021, China
E-mail: zhangwxwz@163.com

Xiao-Yan Zhang
China University of Mining and Technology,
School of Mechanics and Civil Engineering
Ding No. 11 Xueyuan Road, Beijing 100083, China
E-mail: 899210@qq.com

Jin Yu
Huaqiao University,
School of Civil Engineering
No. 668 Jimei Road, Xiamen 361021, China
E-mail: bugyu0717@163.com

DOI https://doi.org/10.18690/actageotechslov.16.2.12-24.2019

Keywords
principal stress rotation; rigid retaining wall; rotation about base; seismic active earth pressure; seismic active rupture angle; pseudo-static method

Ključne besede
rotacija glavne napetosti, toga podporna stena; vrtenje okoli osnove, seizmični aktivni zemeljski tlak, seizmični aktivni kot razpoke, psevdo-statična metoda

Abstract

In this paper, new formulae for seismic active pressure on rigid retaining walls under the rotation about bases (RB) are derived by the pseudo–static method with the consideration of the principal stresses rotation. The calculation of seismic active earth pressure by pseudo-static method is transforming into that of static active earth pressure by the rotating calculation model. The seismic active rupture angle is obtained by Coulomb earth pressure theory. According to Mohr stress circle and the assuming the circular arc trajectory of minor principal stresses as a circular arch, the coefficient of the lateral seismic active earth

Izvleček

V tem prispevku so podane nove enačbe za izračun seizmičnega aktivnega tlaka na toge podporne zidove ob rotaciji okoli osnove (RB), izvedene s psevdo-statično metodo ob upoštevanju rotacije glavnih napetosti. Izračun seizmičnega aktivnega zemeljskega pritiska s psevdo-statično metodo je preoblikovan v statični aktivni zemeljski tlak z rotacijskim računskim modelom. Kot potresne aktivne razpoke dobimo s teorijo Coulombovega zemeljskega pritiska. Na osnovi Mohrove krožnice napetosti in ob predpostavki, da je trajektorija manjših glavnih napetosti krožni lok, sta, ob rotaciji okoli osnove, predlagana koefi-

pressure and the horizontal interfacial friction coefficient are proposed under RB mode. Then based on the force equilibrium of the differential sliding backfill element, the formula for the seismic active earth pressure on the rigid retaining wall under RB mode is obtained, as well as the formulae for the resultant of the seismic active earth pressure and the height of its application. Meanwhile, the effects of influence parameters on the seismic active rupture angle, the lateral seismic active earth pressure and its coefficient, the horizontal interfacial friction coefficient, the resultant of the seismic active earth pressure and the height of its application are discussed. Moreover, the comparisons of predicted values by the proposed method and M-O method are carried out as well as model tests. The result shows that the proposed method is more reasonable and effective than the M-O method.

cient bočnega seizmičnega aktivnega zemeljskega tlaka in medploskovni horizontalni koeficient trenja. S pomočjo ravnotežja sil diferenčnega drsnega zalednega elementa dobimo enačbo za seizmični aktivni zemeljski tlak, delujoč na togo podporno steno, ob rotaciji okoli osnove, kot tudi enačbi za rezultanto seizmičnega aktivnega zemeljskega tlaka in njeno ročico delovanja. V nadaljevanju obravnavamo vplive parametrov na seizmični aktivni kot razpoke, bočni seizmični aktivni zemeljski tlak in njegov koeficient, medploskovni horizontalni koeficient trenja, rezultanto seizmičnih aktivnih zemeljskih tlakov in njeno ročico delovanja. Poleg tega so izvedene primerjave napovedanih vrednosti po predlagani metodi z vrednostmi po metodi M-O ter modelnimi preizkusi. Rezultat kaže, da je predlagana metoda primernejša in bolj učinkovita kot metoda M-O.

1 INTRODUCTION

Retaining walls as a common retaining structure are widely used in geotechnical engineering of building foundations, highways, railways, riverbanks, etc. The distribution of the earth pressure is an important parameter in the design of retaining walls, and it is also the most fundamental and important problem in geotechnical engineering. For the frequent earthquake in the world scope, the analyses of various architectural structures under earthquake have been gradually becoming a hot subject. So, it is very necessary to consider the effects of seismic on earth pressures for the design of retaining structures. The pseudo-static and pseudo--dynamic methods are popularly used to calculate the seismic earth pressure. However, the pseudo-static method, which is first extended from Coulomb earth pressure theory, is more favored than the pseudo-dynamic method.

The most popular method of estimation the active earth pressure during earthquakes is the M-O method. Okabe [1] and Mononobe & Matsuo [2] firstly extended the Coulomb theory to seismic earth pressures by the pseudo-static method. The distribution of the seismic earth pressure on a rigid retaining wall by M-O method is linear along the wall height. However, some experiments [3, 4, 5] have shown that this distribution is nonlinear. In recent decades, many researchers improved the calculation of the seismic earth pressure by the pseudo–static method [6-13] and the pseudo–dynamic theory [14-17]. Based on the limit equilibrium theory, Azad et al. [18] applied the pseudo-dynamic method into the horizontal slice method of analysis with the consideration of the effect of earthquake on the lateral earth pressure. Utilizing a composite logarithmic spiral failure surface at which the Mohr-Coulomb failure criterion is enforced and a limit-equilibrium approach, a slice method for estimating seismic earth pressures based on the pseudo-static method was put forward by Shamsabadi et al. [19]. Chen et al. [20] used the limit equilibrium variational method to study the seismic active earth pressure under general conditions. For the friction stress on the wall, the directions of the major and minor principal stresses are rotated. So, some researchers [21-27] took into account the effect of the principal-stress rotation on static active earth pressures for translating rigid retaining walls, and Li et al. [27] took into account this effect on static active earth pressures for rigid retaining walls under the rotation about bases. And other researchers [12,13, 17] considered the effect of principal-stress rotations on seismic active and passive earth pressures for the translating retaining wall by the pseudo-static and pseudo-dynamic methods. But in these studies of seismic active earth pressures, the rotation of principal stresses which is a well-established phenomenon in geotechnical engineering is seldom considered.

In this paper, by rotating the pseudo-static calculation model for seismic active earth pressure under earthquakes, the seismic active rupture angle is derived according to Coulomb static earth pressure theory. Then, according to the Mohr stress circle, stresses of the backfill behind the rigid retaining wall under the earthquake are were obtained. And by assuming the trajectory of the minor principal stress as a circular arc, the coefficient of the lateral seismic active earth pressure under RB mode and the horizontal interfacial friction coefficient is proposed by integrating shear stress and vertical stress on the

horizontal in the sliding backfill. Furthermore, by force equilibrium of the differential sliding backfill element, analytical solutions for the seismic active earth pressure are obtained. In addition, to check the accuracy of the proposed solutions, comparisons of seismic active earth pressures by the proposed method and M-O method are carried out with the experimental results. Furthermore, parametric studies are investigated.

2 PSEUDO-STATIC ANALYSIS OF THE SEISMIS LOAD

The pseudo-static method is generally applied to the calculation of the seismic earth pressure. The horizontal and vertical inertia forces F_h and F_v of the backfill under the seismic load are calculated by the pseudo-static method as follows:

$$F_h = k_h \rho g \qquad (1)$$

$$F_v = \left(1 - k_v\right) \rho g \qquad (2)$$

where k_h is the horizontal seismic coefficient; k_v is the vertical seismic coefficient; ρ is the density of soil; g is the gravitational acceleration.

According to Fig.1, the seismic angle between the direction of the total acceleration and the plumb line is obtained as follows:

$$\eta = \arctan\frac{F_h}{F_v} = \arctan\frac{k_h \rho g}{\left(1 - k_v\right)\rho g} = \arctan\frac{k_h}{1 - k_v} \qquad (3)$$

Then the total inertia force composed of the gravity and the seismic force can be calculated as follows:

$$F = \frac{\left(1 - k_v\right)\rho g}{\cos\eta} \qquad (4)$$

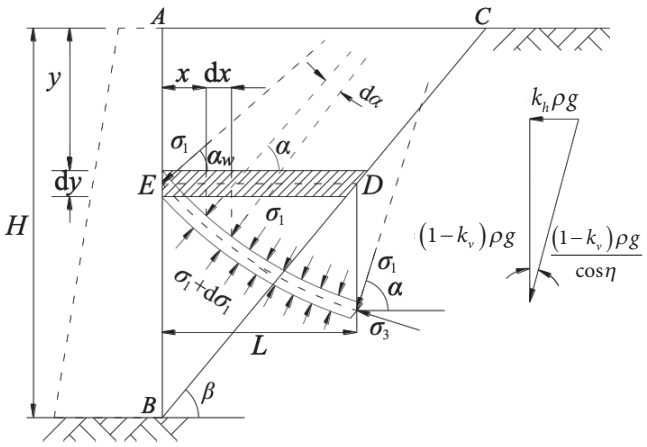

Figure 1. Principal stresses of sliding backfill under seismic load.

3 THEORETICAL ANALYSIS

A vertical rigid retaining wall with height H is analyzed with a cohesionless backfills as shown in Fig. 1. The unit weight of backfills is γ, the wall-soil friction angle is δ, the friction angle of backfills is φ, and the horizontal and vertical seismic accelerations are respectively $k_h g$ and $k_v g$. A sliding surface exists in the backfill behind the rigid retaining wall under the limit equilibrium state, which is approximates to a plane at an angle of β to the horizontal.

3.1 Seismic active rupture angle

To obtain the seismic active rupture angle by Coulomb static earth pressure, rotating the original model calculated seismic earth pressures shown in Fig. 1 with the counterclockwise angle η yields a new inclined rigid retaining wall as shown in Fig. 2. Then the seismic active earth pressure on the vertical rigid retaining wall by pseudo-static mothed is equal to the static active earth pressure on the rigid retaining wall with an inclined angle of η, a height of $H' = H\cos\eta$ and an unit weight of $\gamma' = \gamma(1 - k_v)/\cos\eta$. According to Coulomb static earth pressure theory, the seismic active earth pressure can be obtained by analyzing the static active earth pressure on this inclined rigid retaining wall as shown in Fig.2:

$$E = \frac{\left(1 - k_v\right)\gamma H^2 \cos\left(\beta' - \eta\right)\sin\left(\beta' - \varphi\right)}{2\cos\eta\sin\left(\beta' - \eta\right)\cos\left(\beta' - \varphi - \delta - \eta\right)} \qquad (5)$$

$$\beta' = \beta + \eta \qquad (6)$$

where β' is the pseudo-static seismic active rupture angle.

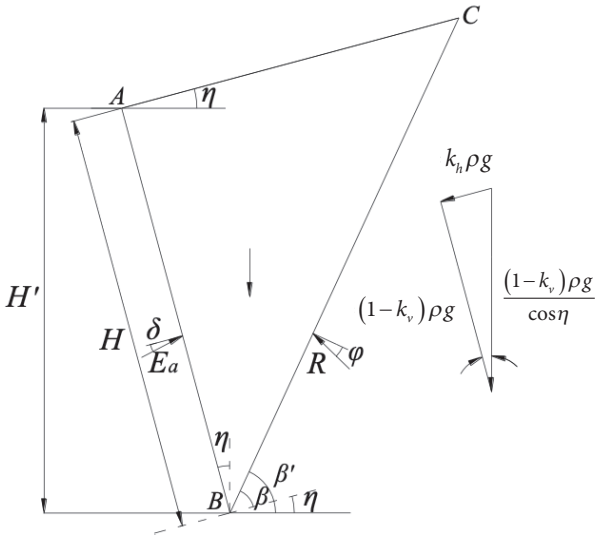

Figure 2. The calculation model of seismic active rupture angle.

From Eqs. (5 and 6), solving $dE/d\beta' = 0$ yields the seismic active rupture angle:

$$\beta = \beta' - \eta = \arctan\left\{\tan(\varphi-\eta)\left[1+\sqrt{1+\cot(\varphi+\delta)\cot(\varphi-\eta)}\right]\right\} \tag{7}$$

3.2 Stresses of the differential sliding backfill element

The relationship between the stresses and the principal stresses at any point of the horizontal in the differential sliding backfill element can be expressed by the Mohr stress circle as shown in Fig.3(a), and the stresses of the backfill at the wall surface and sliding surface are respectively shown as Fig.3(b) and Fig.3(c).

From Fig.3(a), the lateral and vertical earth stresses at any point of a distance x from the wall and a depth y from the backfill surface can be obtained as follows:

$$\sigma_h = \sigma_1 \cos^2\alpha + \sigma_3 \sin^2\alpha \tag{8}$$

$$\sigma_v = \sigma_1 \sin^2\alpha + \sigma_3 \cos^2\alpha \tag{9}$$

where α is the rotational angle of principal stresses at any point in sliding backfills; σ_1 and σ_3 are the major and minor principal stresses, respectively.

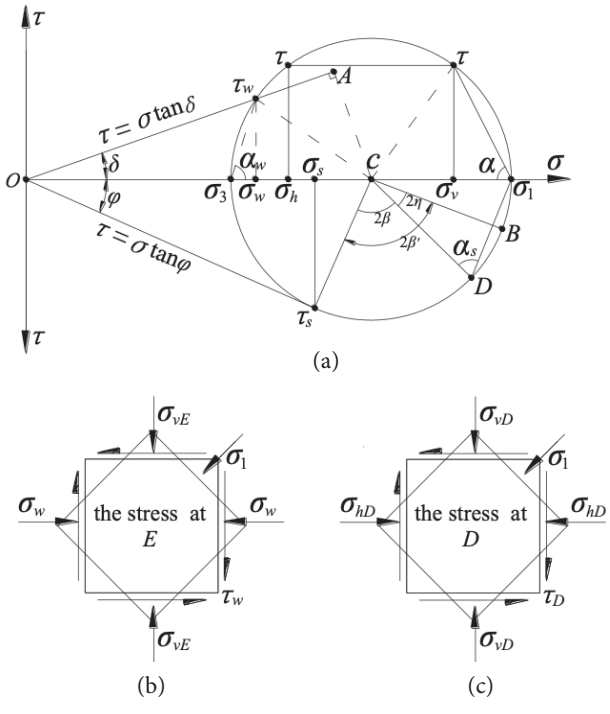

Figure 3. Stresses of sliding backfill (a) Mohr stress circle. (b) The stresses of the backfill at the wall surface. (c) The stresses of the backfill at the sliding surface.

The shear stress at any point of a distance x from the wall and a depth y from the backfill surface can be calculated as follows:

$$\tau = \frac{\sigma_1 - \sigma_3}{2}\sin 2\alpha \tag{10}$$

Similarly, according to Fig.3(a), the lateral earth stress and shear stress on the wall at a depth y can be obtained as follows:

$$\sigma_w = \sigma_1 \cos^2\alpha_w + \sigma_3 \sin^2\alpha_w \tag{11}$$

$$\tau_w = \sigma_w \tan\delta \tag{12}$$

The shear stress and normal stress on the sliding surface at a depth y can be calculated as follows:

$$\tau_s = \frac{(\sigma_1 - \sigma_3)\cos\varphi}{2} \tag{13}$$

$$\sigma_s = \frac{\tau_s}{\tan\varphi} = \frac{(\sigma_1 - \sigma_3)\cos^2\varphi}{2\sin\varphi} \tag{14}$$

From the geometry knowledge in Fig.1, the rotational angle of the principal stress at the wall can be obtained from the equation:

$$\alpha_w = \frac{\pi}{4} + \frac{\delta}{2} + \frac{1}{2}\arccos\frac{\sin\delta}{\sin\varphi} \tag{15}$$

The angle of the minor principal stress plane to the sliding surface can be calculated as follows:

$$\alpha_\beta = \frac{\pi}{4} + \frac{\varphi}{2} \tag{16}$$

From the geometry knowledge in Fig.1, the rotational angle of the principal stress at the sliding surface can be obtained as follows:

$$\alpha_s = \frac{\pi}{2} - \alpha_\beta + \beta = \frac{\pi}{4} - \frac{\varphi}{2} + \beta = \frac{\pi}{4} - \frac{\varphi}{2} + \arctan\left\{\tan(\varphi-\eta)\left[1+\sqrt{1+\cot(\varphi+\delta)\cot(\varphi-\eta)}\right]\right\} \tag{17}$$

3.3 Seismic active stress coefficients

The trajectory of the principal stresses has been observed or inferred to be elliptic, catenary [23, 28], circular arc [29-32] and parabolic [22, 25]. In this study, it is assumed that the trajectory of the minor principal stresses is a circular arc as shown in Fig.1. According to Fig.1, the following expressions can be obtained:

$$dx = R\sin\alpha\, d\alpha \tag{18}$$

$$\alpha = \arccos\left(\cos\alpha_w - \frac{x}{R}\right) \tag{19}$$

The horizontal width L of the differential sliding backfill element at a depth y from the backfill surface can be calculated as follows:

$$L = R\left(\cos\alpha_w - \cos\alpha_s\right) \qquad (20)$$

The gravity of the differential sliding backfill element is obtained as follows:

$$\mathrm{d}G = \gamma\left(H - y\right)\cot\beta\,\mathrm{d}y \qquad (21)$$

The average vertical stress σ_{av} and the average shear stress τ_a on the horizontal of the sliding backfill at a depth y can be respectively calculated as follows:

$$\begin{aligned}\sigma_{av} &= \frac{\int_0^L \sigma_v \mathrm{d}x}{L} = \frac{\int_{\alpha_w}^{\alpha_s} \sigma_1\left(\sin^2\alpha + k_a\cos^2\alpha\right)R\sin\alpha\,\mathrm{d}\alpha}{L} \\ &= \sigma_1\left[1 - \frac{1-k_a}{3}\left(\cos^2\alpha_s + \cos\alpha_w\cos\alpha_s + \cos^2\alpha_w\right)\right]\end{aligned} \qquad (22)$$

$$\begin{aligned}\tau_a &= \frac{\int_0^L \tau\,\mathrm{d}x}{L} = \frac{\int_{\alpha_w}^{\alpha_s} \frac{1-k_a}{2}\sigma_1\sin 2\alpha R\sin\alpha\,\mathrm{d}\alpha}{L} \\ &= \frac{\sigma_1\left(1-k_a\right)\left(\sin^3\alpha_s - \sin^3\alpha_w\right)}{3\left(\cos\alpha_w - \cos\alpha_s\right)}\end{aligned} \qquad (23)$$

where

$$k_a = \frac{\sigma_3}{\sigma_1} = \frac{1-\sin\varphi}{1+\sin\varphi} \qquad (24)$$

Dividing Eq. (11) by Eq. (22) yields the coefficient of the lateral seismic active earth pressure under RB mode:

$$k_{aw} = \frac{\sigma_w}{\sigma_{av}} = \frac{\cos^2\alpha_w + k_a\sin^2\alpha_w}{1 - \frac{1-k_a}{3}\left(\cos^2\alpha_s + \cos\alpha_w\cos\alpha_s + \cos^2\alpha_w\right)} \qquad (25)$$

From Eq. (25), the coefficient of the lateral seismic active earth pressure k_{aw} is similar to the coefficient of the lateral static active earth pressure calculated by Rao et al. [30], but the α_s in the two coefficients are different.

Dividing Eq. (23) by Eq. (22) gives the horizontal interfacial friction coefficient under RB mode:

$$\tan\varphi' = \frac{\tau_a}{\sigma_{av}} = \frac{\left(1-k_a\right)\left(\sin^3\alpha_s - \sin^3\alpha_w\right)}{3\left(\cos\alpha_w - \cos\alpha_s\right) - \left(1-k_a\right)\left(\cos^3\alpha_w - \cos^3\alpha_s\right)} \qquad (26)$$

where φ' is the horizontal interfacial friction angle.

3.4 Seismic active earth pressure

The analytic model of the differential sliding backfill element behind the rigid retaining wall under RB mode is shown in Fig. 4.

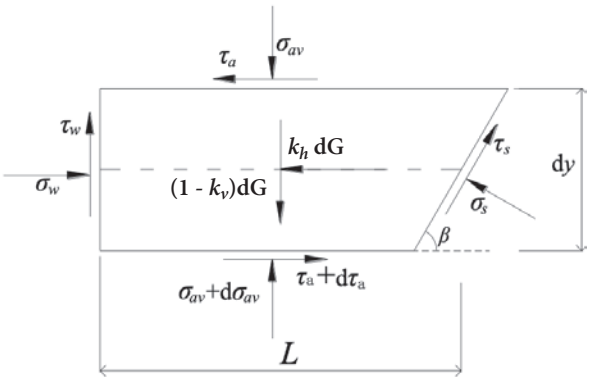

Figure 4. Stresses on differential sliding backfill element.

Analyzing the horizontal and vertical force equilibrium of the differential sliding backfill element yield the following equations:

$$\begin{aligned}&\sigma_w + \tau_s\cot\beta + \left(H-y\right)\frac{\mathrm{d}\tau_a}{\mathrm{d}y}\cot\beta \\ &\quad - k_h\gamma\left(H-y\right)\cot\beta - \sigma_s - \tau_a\cot\beta = 0\end{aligned} \qquad (27)$$

$$\begin{aligned}&\tau_w + \left(H-y\right)\frac{\mathrm{d}\sigma_{av}}{\mathrm{d}y}\cot\beta + \tau_s + \sigma_s\cot\beta \\ &\quad - \left(1-k_v\right)\gamma\left(H-y\right)\cot\beta - \sigma_{av}\cot\beta = 0\end{aligned} \qquad (28)$$

where dy is the thickness of the differential sliding backfill element.

By Eqs. (12, 14, 25 and 26), the following expressions can be got:

$$\begin{aligned}\tau_w &= \sigma_w\tan\delta & \tau_s &= \sigma_s\tan\varphi \\ \sigma_w &= k_{aw}\sigma_{av} & \tau_a &= \sigma_{av}\tan\varphi'\end{aligned} \qquad (29)$$

From Eqs. (27 and 29), the differential equation of the average vertical stress can be obtained as follows:

$$\frac{\mathrm{d}\sigma_{av}}{\mathrm{d}y} = \frac{1-A}{H-y}\sigma_{av} + B\gamma \qquad (30)$$

where

$$A = k_{aw}\tan\beta\frac{1+\tan\left(\beta-\varphi\right)\tan\delta}{\tan\left(\beta-\varphi\right)+\tan\varphi'} \qquad (31)$$

$$B = \frac{\cos\varphi'}{\sin(\beta-\varphi+\varphi')}\left[\left(1-k_v\right)\sin(\beta-\varphi) + k_h\cos(\beta-\varphi)\right] \qquad (32)$$

Integrating Eq. (30) yields the average vertical stress as follows:

$$\sigma_{av} = \frac{\gamma B(H-y)}{A-2} + C(H-y)^{(A-1)} \qquad (33)$$

where C is the integration constant.

By the boundary conditions $\sigma_{av} = 0$ at $y = 0$, substituting $\sigma_{av} = 0$ and $y = 0$ into Eq. (33) gives C as follows:

$$C = \frac{B\gamma}{2-A} H^{(2-A)} \qquad (34)$$

Substituting Eq. (34) into Eq. (33) yields the average vertical stress:

$$\sigma_{av} = \frac{\gamma HB}{A-2}\left[\frac{H-y}{H} - \left(\frac{H-y}{H}\right)^{(A-1)}\right] \qquad (35)$$

From Eqs. (29 and 35), the lateral seismic active earth pressure can be obtained:

$$\sigma_w = k_{aw}\sigma_{av} = k_{aw}\frac{\gamma HB}{A-2}\left[\frac{H-y}{H} - \left(\frac{H-y}{H}\right)^{(A-1)}\right] \qquad (36)$$

Integrating Eq. (36) yields the resultant of the lateral seismic active earth pressure:

$$E_h = \int_0^H \sigma_w \mathrm{d}y = k_{aw}\frac{\gamma H^2}{2}\frac{B}{A} \qquad (37)$$

From Eq. (37), the resultant of the seismic active earth pressure can be calculated:

$$E_a = \frac{E_h}{\cos\delta} = \frac{k_{aw}}{\cos\delta}\frac{\gamma H^2}{2}\frac{B}{A} \qquad (38)$$

Substituting Eqs. (31 and 32) into Eq. (38) yields:

$$E_a = \frac{(1-k_v)\gamma H^2 \sin(\beta+\eta-\varphi)}{2\cos\eta\tan\beta\cos(\beta-\varphi-\delta)} \qquad (39)$$

Substituting Eq. (6) into Eq. (5) also yields Eq. (39), this verifies it is correct that the derivation of the seismic active earth pressure under RB mode considering principal stress rotation by pseudo-static method.

From Eq. (36), the moment M of the resultant of the lateral seismic active earth pressure about the wall base is obtained by integrating $\sigma_w(H-y)$ with respect to y as follows:

$$M = \int_0^H \sigma_w (H-y)\mathrm{d}y = k_{aw}\frac{\gamma H^3 B}{3(A+1)} \qquad (40)$$

Dividing Eq. (40) by Eq. (37) gives the height of the application of the E_h:

$$h = \frac{M}{E_h} = \frac{H}{3}\frac{2A}{A+1} \qquad (41)$$

Letting $A = 1$ in Eq. (41), the height of the application of the seismic active earth pressure is equal to that of the static active earth pressure obtained by Rankine and Coulomb.

4 COMPARISONS

To check the applicability of the proposed method, the calculated values of the lateral seismic active earth pressure under RB mode by Eq. (36) are compared with those by M-O method and the experimental results under RB mode by Ishibashi and Fang [4], as shown in Fig. 5. The parameters considered in the field test by Ishibashi and Fang [4] were: $\varphi = 40°$, $\delta = 20°$, $k_h = 0.215$ and $k_v = 0$.

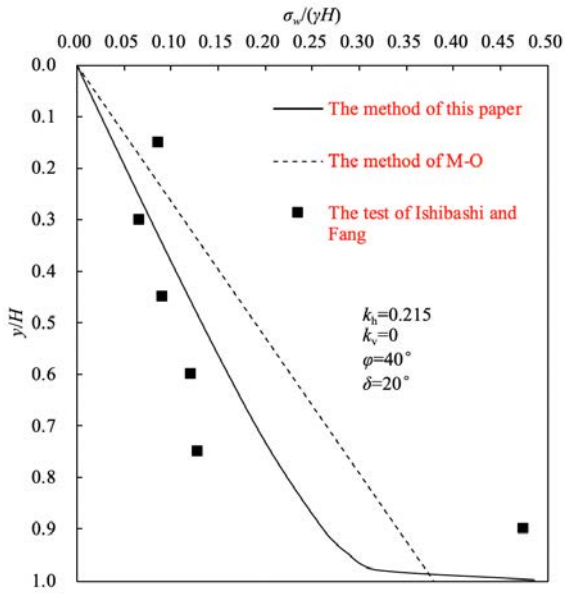

Figure 5. Comparison of the lateral seismic active earth pressure.

It can be seen clearly from Fig. 5 that the distributions of the lateral seismic active earth pressure by the proposed method and by field test are non-linear, but this distribution by M-O method is linear. This is because in the M-O method the distribution of the lateral seismic active earth pressure was assumed to be linear, and the displacement mode of the retaining wall and the principal-stresses rotation were not considered. Fig. 5 shows that the results obtained by the proposed method is closer to the measured values than those by M-O method. Therefore, it is proved that the seismic active

earth pressure predicted by the proposed method is feasible and reasonable for the design of retaining walls under RB mode.

5 PARAMETRIC STUDY

5.1 Seismic active rupture angle

Figs. 6 and 7 show the variations of the seismic active rupture angle β under RB mode with the horizontal and vertical seismic coefficients, internal friction angle of backfills and wall–soil friction angle.

Figs. 6 and 7 show that the seismic active rupture angles β are always smaller than $\pi/4+\varphi/2$. The β increases with the increase of φ, but it decreases with the increase of k_h and k_v respectively, and it almost decreases linearly with the increase of δ. Moreover, the effect of φ on β is greater than that of δ.

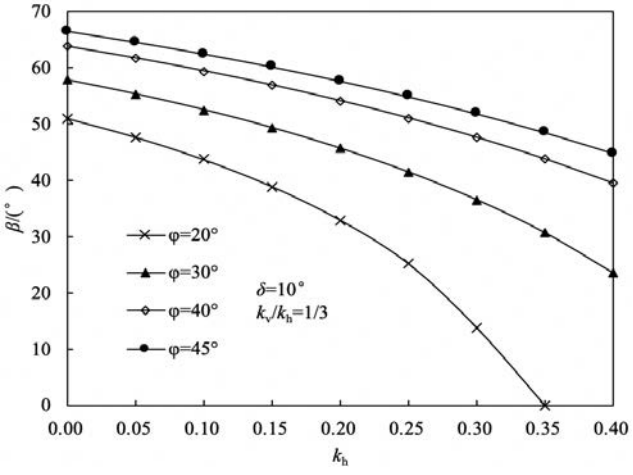

Figure 6. Effect of the horizontal seismic coefficient on β under different φ.

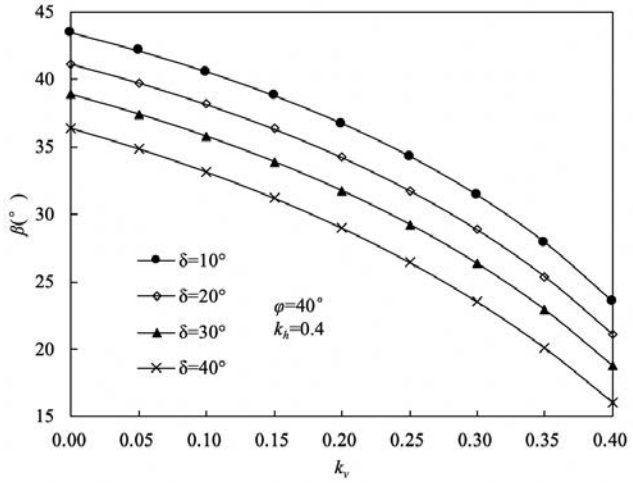

Figure 7. Effect of the vertical seismic coefficient on β under different δ.

5.2 Coefficient of lateral seismic active earth pressure

Figs. 8-11 show the variations of the coefficient k_{aw} of the lateral seismic active earth pressure under RB mode with the horizontal and vertical seismic coefficients, internal friction angle of backfills and wall–soil friction angle.

From Figs. 8-11, the k_{aw} is smaller than 0.5, and non-linearly decreases with the increase of φ. But k_{aw} non-linearly increases with the increases of δ, k_h and k_v, respectively.

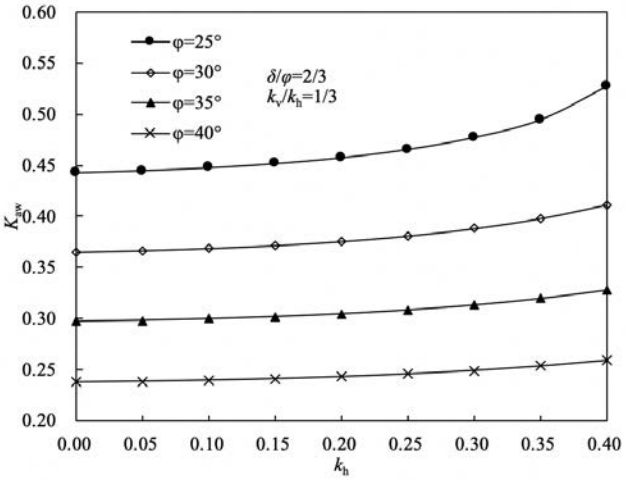

Figure 8. Effect of the horizontal seismic coefficient on k_{aw} under different φ.

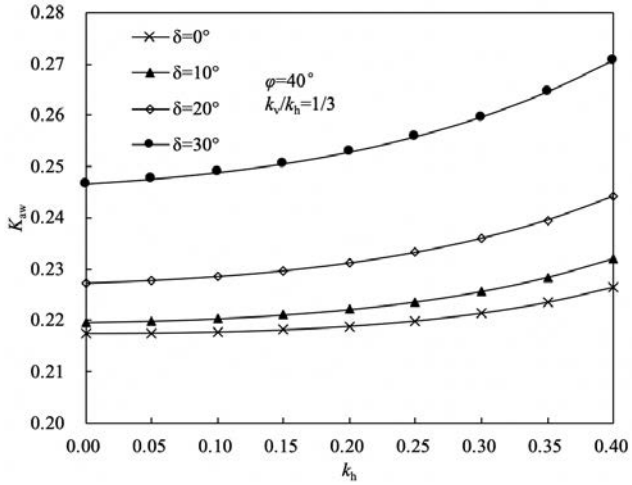

Figure 9. Effect of the horizontal seismic coefficient on k_{aw} under different δ.

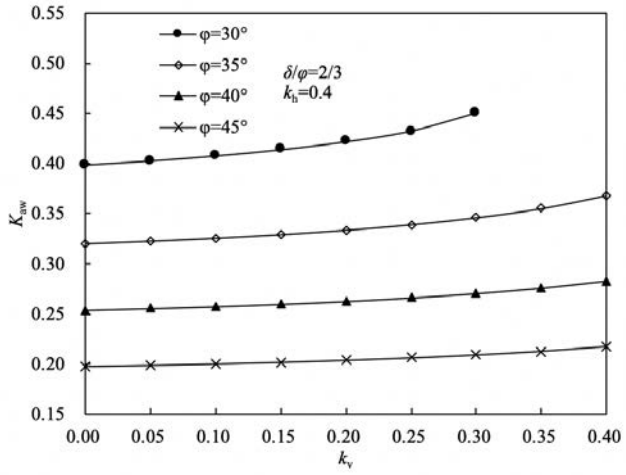

Figure 10. Effect of the vertical seismic coefficient on k_{aw} under different φ.

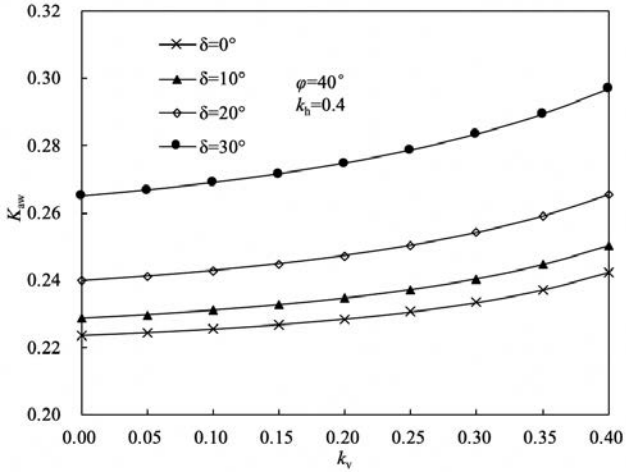

Figure 11. Effect of the vertical seismic coefficient on k_{aw} under different δ.

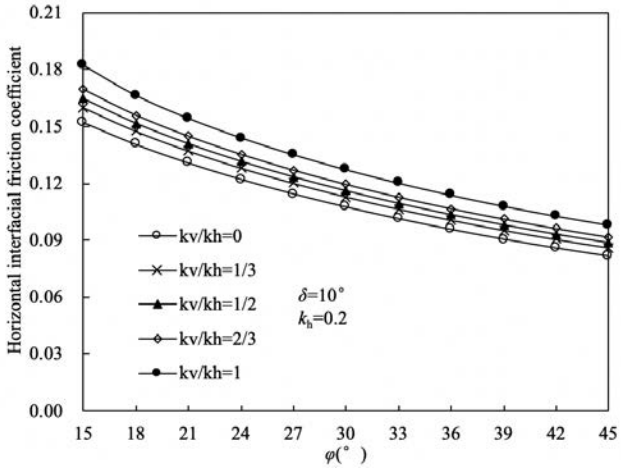

Figure 12. Effects of the internal friction angle on tanφ' under different k_v/k_h.

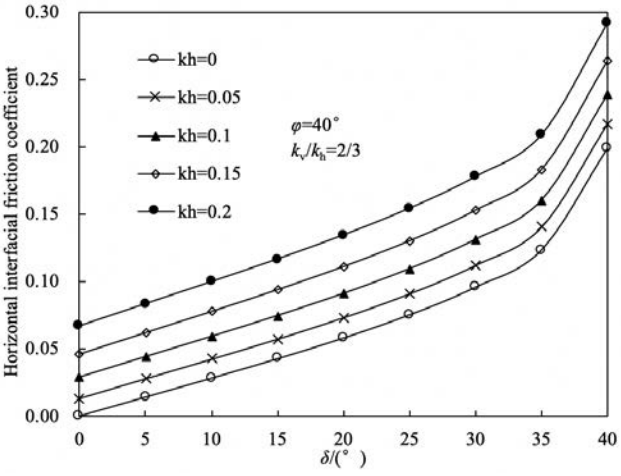

Figure 13. Effects of the wall–soil friction angle on tanφ' under different k_h.

5.3 Horizontal interlayer friction coefficient

Figs. 12 and 13 show the variations of the horizontal interfacial friction coefficient with these influence parameters (i.e. the internal friction angle φ, horizontal seismic coefficient k_h and vertical seismic coefficient k_v).

From Fig. 12, the horizontal interlayer friction coefficient tanφ' decreases from 0.18 to 0.09 with the increase of φ from 15° to 45° and with the decrease of k_v from 0 to k_h. From Fig. 13, the tanφ' increase from 0 to 0.3 with the increase of δ from 0 to φ and k_h from 0 to 0.2, and it is smaller than tanφ = tan40° = 0.839. Moreover from Fig. 12 and Fig. 13, it can be seen obviously that influence of k_h on tanφ' is more significant than that of k_v on tanφ', and the influence of δ on tanφ' is more significant than that of φ on tanφ'.

5.4 Lateral seismic active earth pressure

Figs. 14-17 show the distributions of the normalized lateral seismic active earth pressure $\sigma_w/(\gamma H)$ along the normalized wall height with φ, δ, k_h and k_v.

From Figs. 14-17, the maximum value of the lateral seismic active earth pressure is located near the wall toe,that is consistent with the experimental results [4] for rigid retaining walls under RB mode. Moreover, the lateral seismic active earth pressure σ_w is concave nonlinear distribution along the wall height except for k_h<0.1, and the distribution of σ_w varies from right-convex to concave with increase of k_h from 0 to 0.2. The σ_w decreases with the increase of φ, δ and k_v, respectively. But the σ_w increases with the increase of k_h.

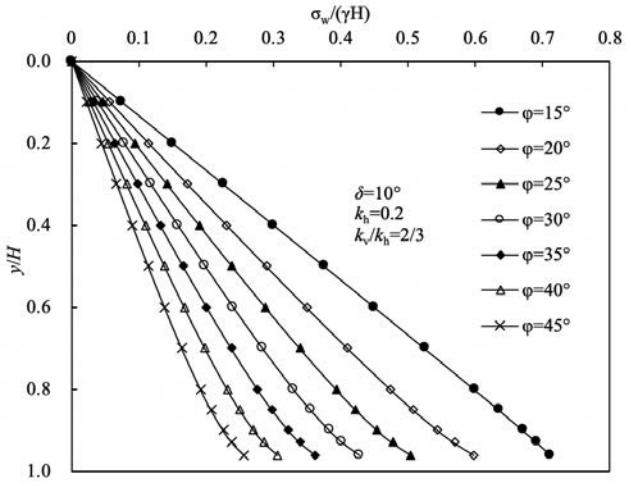

Figure 14. Effect of the internal friction angle on $\sigma_w/(\gamma H)$.

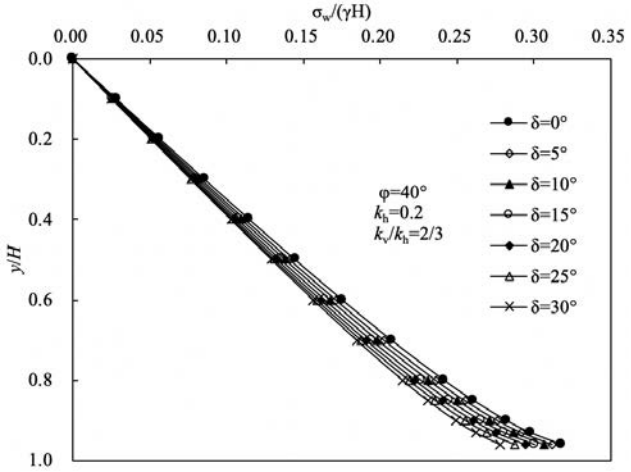

Figure 15. Effect of the wall–soil friction angle on $\sigma_w/(\gamma H)$.

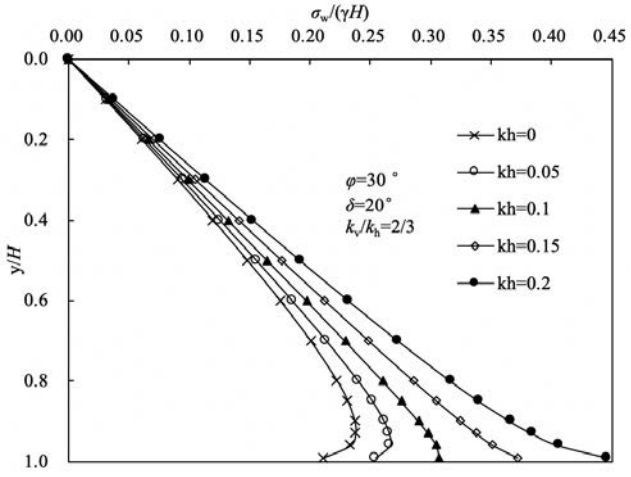

Figure 16. Effect of the horizontal seismic coefficient on $\sigma_w/(\gamma H)$.

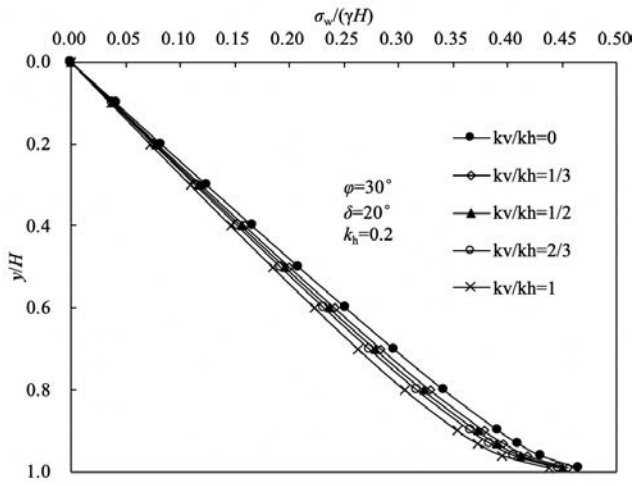

Figure 17. Effect of the ratio between the vertical and horizontal seismic coefficients on $\sigma_w/(\gamma H)$.

From Figs. 14-17, the resultant of the seismic active earth pressure respectively decreases with the increase ofφ, δ and k_v, but increases with the increase of k_h.

5.5 Height of the application of the seismic active earth pressure

Figs. 18-19 show the variations of the normalized height of the application of the seismic active earth pressure h/H with φ, δ/φ, k_h and k_v/k_h.

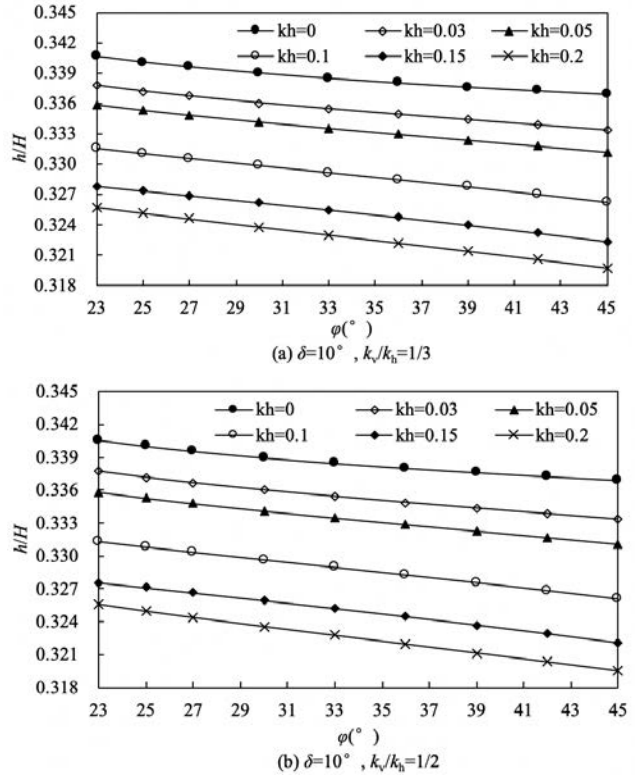

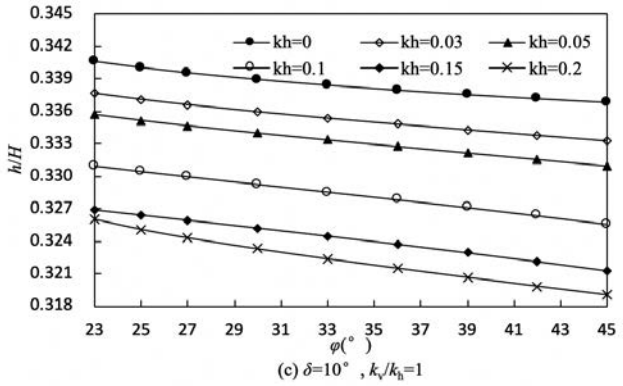

Figure 18. Change of the height of the application of the lateral seismic active earth pressure with φ under different k_h.

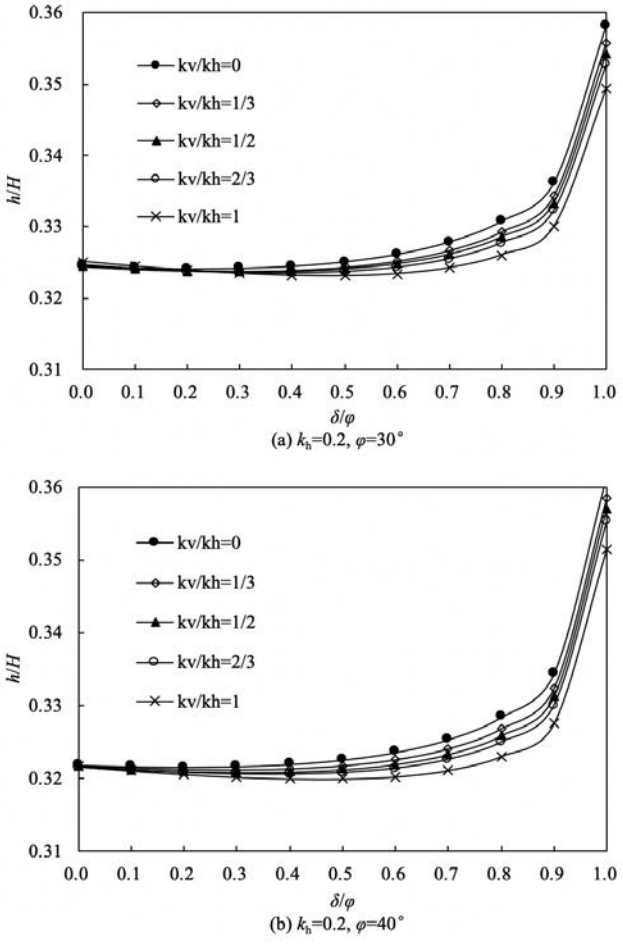

Figure 19. Change of the height of the application of the lateral seismic active earth pressure with δ/φ under different k_v/k_h.

From Figs. 18 and 19, the normalized height of the application of the lateral seismic active earth pressure h/H approximately decreases linearly with the increase of φ, and first decreases and then increases with the increase of δ/φ, but it non-linearly decreases with the increase of k_h. Moreover, the h/H increases with the increase of k_v/k_h for $\delta/\varphi \le 0.1$ and $\varphi \le 28°$, but decreases with the increase of k_v/k_h for $\delta/\varphi \ge 0.6$.

The h/H is greater than 1/3 and smaller than 0.3406 for $k_h \le 0.03$, but it is smaller than 1/3 and greater than 0.319 for $k_h \ge 0.1$. Moreover, the h/H is smaller than 1/3 and greater than 0.3311 for $\varphi > 33°$ and $k_h = 0.05$, and it is smaller than 1/3 and greater 0.3199 for $\delta/\varphi \le 0.8$ and $k_h > 0$, but it is greater than 1/3 and smaller than 0.3359 for $23° \le \varphi \le 33°$ and $k_h = 0.05$.

6 CONCLUSIONS

In the proposed method, the seismic problem was simplified to the static problem using the pseudo-static method. By rotating, the seismic angle is added to the inclined angles of the wall and backfill surface in the formula of Coulomb static earth pressure, then the seismic active rupture angle was obtained according to Coulomb static earth pressure theory. Moreover, the basic equations of the seismic active earth pressure under RB mode were established by stress analysis and the static equilibrium. Then, the theoretical formulae for the seismic active earth pressure and its coefficient, the resultant of the seismic active earth pressure and its application height are put forward for the design of rigid retaining walls under RB mode considering the principal-stress rotation.

The effects of main parameters (i.e. the internal friction angle of backfills, wall-soil friction angle, horizontal and vertical seismic coefficients) on the seismic active rupture angle, the coefficient of the lateral seismic active earth pressure, the horizontal interface friction coefficient, the distribution of the seismic active earth pressure, the resultant earth pressure and the height of its application were analyzed. The horizontal seismic coefficient has a greater influence on the seismic active earth pressure of rigid retaining walls than the vertical seismic coefficient, and the internal friction angle of backfills has a greater influence on the seismic active earth pressure of rigid retaining walls than the wall-soil friction angle. The comparisons of predicted and measured values of the lateral seismic active earth pressure showed that the proposed method agreed better with the experiment than M-O method. This proposed method is feasible and reasonable in the design of seismic rigid retaining walls under RB mode.

Acknowledgments

This research was supported by the Natural Science Foundation of China (Grant 51774147 and 51978292), Natural Science Foundation of Fujian Province of China (Grants

2017J01669 and 2017J01094), Scientific Research Program of Hebei Education Department (Grant QN2018098) and Opening Fund of State Key Laboratory of Geohazard Prevention and Geoenvironment Protection (Chengdu University of Technology), China (SKLGP2018K008). All support is gratefully acknowledged.

Notation

The following symbols are used in this paper:

F_h = horizontal inertia force of the backfill
F_v = vertical inertia force of the backfill
F = total inertia force of the backfill
k_h = horizontal seismic coefficient
k_v = vertical seismic coefficient
ρ = density of the backfill
g = gravitational acceleration
k_hg = horizontal seismic acceleration
k_vg = vertical seismic acceleration
η = seismic angle
γ = unit weight of the backfill
γ' = unit weight of the backfill in rotating calculation model
δ = wall-soil friction angle
φ = internal friction angle of backfills
β = seismic active rupture angle
β' = pseudo seismic active rupture angle
H = height of the rigid retaining wall
H' = height of the rigid retaining wall after rotation
α = rotational angle of principal stresses
σ_1 = major principal stress
σ_3 = minor principal stress
σ_h = horizontal stress on the vertical of the differential sliding backfill element at any point
σ_v = vertical stress on the horizontal of the differential sliding backfill element at any point
τ = shear stress on horizontal of the differential sliding backfill element at any point
σ_w = lateral earth pressure on the wall
τ_w = shear stress on the wall
α_w = rotational angle of the principal stress at the wall
τ_s = shear stress on the sliding surface
σ_s = normal stress on the sliding surface
α_β = angle between the active sliding surface and the major principal stress plane
α_s = angle between the horizontal and major principal stress at the sliding surface
dx = differential length along the horizontal
L = horizontal width of the differential flat element
R = radius of the circular arc
x = horizontal distance of arbitrary point in differential flat element from the wall
y = depth of the differential element from the backfill surface
dG = self-weight of differential sliding backfill element
σ_{av} = average vertical stress on the horizontal in differential element
τ_a = average shear stress on the horizontal in differential element
k_a = coefficient of active earth pressure by Rankine
k_{aw} = coefficient of lateral seismic active earth pressure in this paper
φ' = horizontal interlayer friction angle
$\tan\varphi'$ = interfacial friction coefficient
E_h = resultant of lateral seismic active earth pressure on the retaining wall
E_a = resultant of seismic active earth pressure on the retaining wall
M = moment of the lateral seismic active earth pressure about the wall base
h = height of application of the seismic active earth pressure

REFERENCES

[1] Okabe, S. 1926. General theory of earth pressure. Journal of the Japanese society of Civil Engineers 12(1), 1277–1323.
[2] Mononobe, N., Matsuo, O. 1929. On the determination of earth pressure during earthquakes. Proceeding of the World Engineering Congress, 9, Tokyo, Japan, pp. 179–187.
[3] Khosravi, M.H., Pipatpongsa, T., Takemura, J. 2013. Experimental analysis of earth pressure against rigid retaining walls under translation mode. Géotechnique 63(12), 1020-1028. DOI: 10.1680/geot.12.P.021
[4] Ishibashi, I., Fang, Y.S. 1987. Dynamic earth pressures with different wall movement modes. Soils and Foundations 27(4), 11-22. DOI:10.3208/sandf1972.27.4-11
[5] Sherif, M.A., Fang, Y.S. 1984. Dynamic earth pressures on walls rotating about the top. Soils and Foundations 24(4), 109-117. DOI:10.3208/sandf1972.24.4-109
[6] Ghosh, S., Debnath, C. 2016. Pseudo-static analysis of reinforced earth retaining wall considering nonlinear failure surface. Geotechnical and Geological Engineering 34(4), 981-990. DOI: 10.1007/s10706-016-0018-6
[7] Iskander, M., Chen, Z., Omidvar, M., Guzman, I., Elsherif, O. 2013. Active static and seismic earth pressure for c–φ, soils. Soils and Foundations 53, 639–652. DOI: 10.1016/j.sandf.2013.08.003

[8] Caltabiano, S., Cascone, E., Maugeri, M. 2012. Static and seismic limit equilibrium analysis of sliding retaining walls under different surcharge conditions. Soil Dynamics and Earthquake Engineering 37(6), 38-55. DOI: 10.1016/j.soildyn.2012.01.015

[9] Nouri, H., Fakher, A., Jones, C.J.F.P. 2008. Evaluating the effects of the magnitude and amplification of pseudo-static acceleration on reinforced soil slopes and walls using the limit equilibrium horizontal slices method. Geotextiles and Geomembranes 26(3), 263-278. DOI: 10.1016/j.geotexmem.2007.09.002

[10 Choudhury, D., Singh, S. 2006. New approach for estimation of static and seismic active earth pressure. Geotechnical and Geological Engineering 24(1), 117-127. DOI: 10.1007/s10706-004-2366-x

[11] Rao, K.S.S., Choudhury, D. 2005. Seismic passive earth pressures in soils. Journal of Geotechnical and Geoenvironmental Engineering 131(1), 131-135. DOI: 10.1061/(ASCE)1090-0241(2005)131:1(131)

[12] Zhou, Y., Chen, F. 2015. Seismic active earth pressure for non-vertical rigid retaining wall considering soil arching effect. Chinese Journal of Rock Mechanics & Engineering 34(7), 1452-1461. DOI:1000-6915(2015)07-1452-10 (In Chinese)

[13] Pain, A., Chen, Q., Nimbalkar, S., Zhou, Y. 2017. Evaluation of seismic passive earth pressure of inclined rigid retaining wall considering soil arching effect. Soil Dynamics & Earthquake Engineering 100(9), 286-295. DOI: 10.1016/j.soildyn.2017.06.011

[14] Choudhury, D., Katdare, A.D., Pain, A. 2014. New method to compute seismic active earth pressure on retaining wall considering seismic waves. Geotechnical and Geological Engineering 32(2), 391-402. DOI: 10.1007/s10706-013-9721-8

[15] Ghosh, S., Sharma, R.P. 2012. Seismic active earth pressure on the back of battered retaining wall supporting inclined backfill. International Journal of Geomechanics 12(1), 54-63. DOI: 10.1061/(ASCE)GM.1943-5622.0000112

[16] Kolathayar, S., Ghosh, P. 2011. Seismic active earth pressure on walls with bilinear backface using pseudo-dynamic approach. Geotechnical and Geological Engineering 29(3), 307-317. DOI: 10.1016/j.compgeo.2009.05.015

[17] Zhou, Y., Chen, F., Wang, X. 2018. Seismic active earth pressure for inclined rigid retaining walls considering rotation of the principal stresses with pseudo-dynamic method. International Journal of Geomechanics 18(7). DOI: 10.1061/(ASCE)GM.1943-5622.0001198

[18] Azad, A., Yasrobi, S.S., Pak, A. 2008. Seismic active pressure distribution history behind rigid retaining walls. Soil Dynamics and Earthquake Engineering 28(5), 365-375. DOI: 10.1016/j.soildyn.2007.07.003

[19] Shamsabadi, A., Xu, S.Y., Taciroglu, E. 2013. A generalized log-spiral-rankine limit equilibrium model for seismic earth pressure analysis. Soil Dynamics and Earthquake Engineering 49(6), 197-209. DOI: 10.1016/j.soildyn.2013.02.020

[20] Chen, J., Yang, Z., Hu, R., Zhang, H. 2016. Study on the seismic active earth pressure by variational limit equilibrium method. Shock and Vibration 2016(3), 1-10. DOI: 10.1155/2016/4158785

[21] Zhou, Q.Y., Zhou, Y.T., Wang, X.M., Yang, P.Z. 2017. Estimation of active earth pressure on a translating rigid retaining wall considering soil arching effect. Indian Geotechnical Journal. DOI: 10.1007/s40098-017-0252-8

[22] Zhou, Y., Chen, Q., Chen, F., Xue, X., & Basack, S. 2018. Active earth pressure on translating rigid retaining structures considering soil arching effect. European Journal of Environmental and Civil Engineering, 22(8), 910-926. DOI: 10.1080/19648189.2016.1229225

[23] Handy, R.L. 1985. The arch in soil arching. Journal of Geotechnical Engineering 111, 302–318. DOI:10.1061/(asce)0733-9410(1985)111:3(302)

[24] Paik, K.H., Salgado, R. 2003. Estimation of active earth pressure against rigid retaining walls considering arching effects. Geotechnique 53(7), 643-653.

[25] Goel, S., Patra, N.R. 2008. Effect of arching on active earth pressures for rigid retaining walls considering translation mode. International Journal of Geomechanics 8(2), 123-133. DOI: 10.1061/(ASCE)1532-3641 (2008)8:2(123)

[26] Li, J.P., Wang, M. 2014. Simplified method for calculating active earth pressure on rigid retaining walls considering the arching effect under translational mode. International Journal of Geomechanics 14(2), 282-290. DOI: 10.1061/(ASCE)GM.1943-5622. 0000313

[27] Li, D., Wang, W., Zhang, Q. 2014. Lateral earth pressure behind walls rotating about base considering arching effects. Mathematical Problems in Engineering 2014, 1-7. Doi: 10.1155/2014/715891

[28] Harrop-Williams, K.O. 1989. Geostatic wall pressures. Journal of Geotechnical Engineering 115, 1321–1325. DOI:10.1061/(asce)0733-9410(1989)115:9(1321)

[29] Cai, Y., Chen, Q., Zhou, Y., Nimbalkar, S., Yu, J. 2016. Estimation of passive earth pressure against rigid retaining wall considering arching effect in cohesive-frictional backfill under translation mode. International Journal of Geomechanics

17(4), 1-11. DOI: 10.1061/(ASCE)GM.1943-5622.0000786

[30] Rao, P., Chen, Q., Zhou, Y., Nimbalkar, S., & Chiaro, G. 2016. Determination of active earth pressure on rigid retaining wall considering arching effect in cohesive backfill soil. International Journal of Geomechanics, 16(3), 1-9. doi: 10.1061/(ASCE)GM.1943-5622.0000589

[31] Dalvi, R.S., Pise, P. J. 2012. Analysis of arching in soil-passive state. Indian Geotechnical Journal 42(2), 106-112. DOI: 10.1007/s40098-012-0004-8

[32] Dalvi, R.S., Bhosale, S.S., Pise, P.J. 2005. Analysis for passive earth pressure-catenary arch in soil. Indian Geotechnical Journal 35 (4), 388–400.

A NUMERICAL STUDY OF REINFORCED EMBANKMENT-SUPPORTED BY ENCASED FLOATING COLUMNS

NUMERIČNA ŠTUDIJA OJAČENIH NASIPOV, PODPRTIH Z OBLOŽENIMI GRUŠČNATIMI STEBRI

Mehmet Rifat Kahyaoğlu *(corresponding author)*
Muğla Sitki Kocman University, Engineering Faculty,
Department of Civil Engineering
48000, Mentese-Muğla, Turkey
E-mail: rkahyaoglu@mu.edu.tr

Martin Vaníček
Geosyntetika Ltd.
N.Tesla str. 3, 160 00 Praha 6, The Czech Republic
E-mail: mvanicek@geosyntetika.cz

DOI https://doi.org/10.18690/actageotechslov.16.2.25-38.2019

Keywords

geogrid reinforcement, geotextile encasement, surcharge, soil settlement, column bulging, sand mat

Ključne besede

geomreže, geotekstilna obloga, preobremenitev, posedanje zemljine, izbočenje stebra, peščena podlaga

Abstract

This paper presents a three-dimensional, finite-element, parametric study of a base-reinforced embankment supported by encased floating columns on soft soil. A 3D numerical model is made to study the effects of geogrid basal reinforcement and geotextile encasement on the displacement behavior of the columns. The numerical model was initially verified using measured data from a real case study. Then, parametric studies were subsequently performed, considering the effect of the encasement stiffness, the basal reinforcement stiffness and the embankment fill height, together with an examination of the effective length of the encasement. The results from this parametric study are presented here in the form of comparative graphs. The objective of this paper is to present the behavior of the embankment on floating encased columns after the soft soil consolidation for different embankment heights, basal reinforcement and column-encasement stiffnesses.

Izvleček

V prispevku je predstavljena tridimenzionalna parametrična študija končnih elementov ojačenega nasipa, podprtega z geotekstilom obloženimi gruščnatimi stebri na mehkih tleh. Izdelan je 3D numerični model za proučevanje učinkov osnovne ojačitve z geomrežo in geotekstilnih oblog na deformacijsko obnašanje gruščnatih stebrov. Numerični model smo sprva preverili s pomočjo študije izmerjenih podatkov na realnem primeru. Nato so bile naknadno izvedene parametrične študije ob upoštevanju učinka togosti geotekstilnih oblog, togosti osnovne ojačitve z geomrežo in višine polnilnega nasipa vzdolž raziskovane efektivne dolžine geotekstilnih oblog. Rezultati iz te parametrične študije so predstavljeni v obliki primerjalnih grafov. Cilj tega prispevka je predstaviti obnašanje nasipa ležečega na z geotekstilom obloženih gruščnatih stebrih po konsolidaciji mehkih tal za različne višine nasipov, osnovne ojačitve in togosti z geotekstilom obloženih stebrov.

1 INTRODUCTION

The construction of embankments on soft soils, as part of the efforts to reclaim new areas for the construction of highways, railways, airport runways and urban infrastructure, faces several hurdles with regard to the low load-bearing capacity and high compressibility of the subsoil, as well as the tendency for excessive lateral deformations. Among the various available techniques, such as surcharging, excavation and replacement, vertical drainage, vacuum consolidation and column-

-supported embankments, the use of column-supported embankments (CSEs) allows for a rapid construction, total and differential settlement reduction, and adjacent facility protection [1-3]. However, it is impossible to construct CSEs in very soft clays (cu < 15 kN/m2) due to the insufficient columns material lateral confinement and excessive lateral bulging of the columns [4-6].

In such soils, the required lateral confinement can be induced through the encasement of individual columns with geosynthetics [7-11]. In 1995 the first project utilizing a seamless geotextile-encased column was successfully implemented in Germany, and later, Kempfert et al. [5], Raithel and Kempfert [6] and Raithel et al. [7] tested the performance of geosynthetic-encased stone columns (GECs) using numerical and analytical models. The technique detailed in the above-mentioned projects has been adopted in Europe [8, 9] and more recently in South America [11], but with growth in the construction sector and improvements in geosynthetic production technologies, new design procedures have been developed.

The performance of geosynthetic encasement on the capacity and settlement behavior of soft soils has been studied in both laboratory and field tests [12-17], while numerical studies of encased granular columns have been conducted successfully in the literature [18-27]. The cited studies investigated the influence of the geometry and material properties of encased and non-encased stone columns (SCs) on vertical stresses, excess pore-water pressures and tangential strains in the geotextile, with a focus on the effect of encasement length and stiffness, the strength of the soft ground and surcharge from the embankment fill. The benefit of encasing stone columns in terms of settlement, lateral deformation and load-carrying capacity has been underlined in the above studies, and design charts for an estimation of the maximum settlement in soil and column strain during the preliminary design are presented.

In recent years, in the event of high embankment loads, one layer of geogrid has been used at the base of the embankment in combination with GECs over soft clay soils to form a geosynthetic reinforced and column-supported embankment (GRCSE) [28-30]. The application of a geogrid layer over the columns and the soft soil enhances the efficiency of the load transfer from the embankment to the columns, provides controllable deformation, minimizes soil yield, enhances global stability and eliminates the need for inclined columns to resist the horizontal thrust at the sides of the embankment [31-34]. The complicated mechanism of load transfer in GRCSEs combines with the arching effects, tension in the geosynthetic reinforcement and stress transfer from the soft soil to the column due to the different stiffness values. Over the past few years, both experimental and numerical investigations into the behavior of GRCSE have been carried out by many researchers [35, 37]. Previous studies have analyzed the performance of GECs and the time-dependent behaviors of geosynthetic-reinforced embankments supported on end-bearing columns.

In some instances, when the column does not reach a hard stratum, the construction of floating columns is found to be more economical and technically feasible. The frictional force along the floating column, based on the relative deformation between the column and the surrounding soil, affects the behavior of GECs [36, 38, 39]. Although previous research has contributed valuable information to the knowledge of end-bearing columns, information about the group behavior of floating columns is still lacking, and so further research is required into the design of embankments on encased floating columns [40-42].

This paper explores the time-dependent behavior of geogrid-reinforced embankments supported by floating columns encased in geotextiles. Firstly, a real case study of GRCSE in thick soft soil was modeled numerically. Then, the numerical results and the measured data were compared, and some calibrations on the numerical model were made for the verification. Finally, parametric studies including variations of the embankment height, the stiffness of the column encasement and the base reinforcement were performed.

Many of the recent studies mentioned above have dealt with the load-carrying capacities and settlement of unreinforced embankments supported with GECs; however, the effects of reinforcement to the base of the embankment have not been considered to date, nor have the load-transfer mechanism and the lateral bulging deformation patterns associated with GECs. The published literature focusing on the long-term effects of these parameters on the vertical and lateral displacement behaviors of the GECs is limited, and so in order to enhance the performance of the GECs to contribute to the above-mentioned issues, the objectives of this paper are as follows: (1) to examine the long-term behavior (100% consolidation) of a floating, column-supported embankment under different surcharges; (2) to investigate the performance of basal geogrid reinforcement; (3) to consider the effects of geotextile encasement on the lateral and vertical displacement of columns; and (4) to determine the effective length of the geotextile encasement of floating columns.

2 NUMERICAL MODELLING

2.1 Model verification

A case study of a stone-column-supported embankment constructed in Kebun-Malaysia, the details of which can be found in Raju (1997) [43], was modelled numerically. The soil profile for the Kebun Interchange project contained marine clay where the CPT tip resistance values for the top 11 m are 0.1–0.3 MPa (Fig 1). Stone columns with a 1.1-m diameter were installed at a 2.2-m rectangular spacing to a depth of 12 m under the 2.6-m-high embankment. Settlement gauges were placed on the top of the stone columns and the total settlement was read as 0.4 m. A 1-m settlement was observed for untreated ground under the same circumstances. The results of the settlement in the soft soil and the encased column after the completion of the embankment construction from our numerical model were compared with measured settlements from the Kebun project. This comparison presented in Fig. 2 shows that the numerical model followed the trends of the measured data. The vertical stress transmitted to both the stone column and the soft soil was verified with measured values, and this consistency indicates that the numerical model is appropriate for a parametric study.

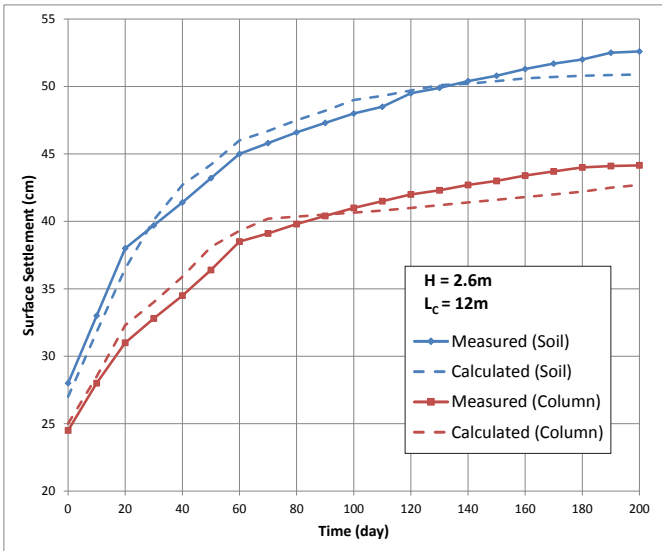

Figure 2. Comparison between the calculated and measured settlements of the column and the soil.

2.2 Parametric study

GRCSE in 40-m-thick soft soil lying on a rigid and firm layer were modeled and studied numerically. The water level was modelled at the original ground surface. Floating columns having a diameter of 1 m (D) were arran-

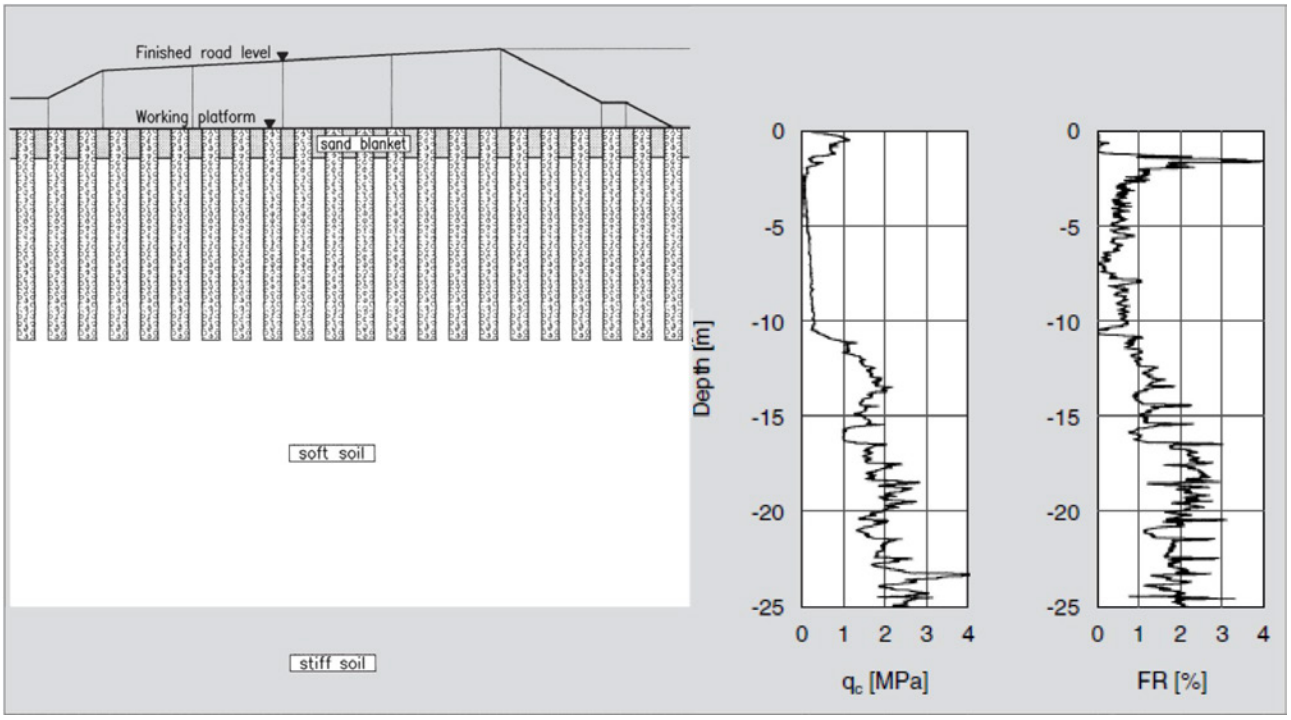

Figure 1. Schematic section view of Kebun Case (Raju, 1997) and tip resistance (q_c) - friction ratio (FR) with depth.

ged in a square-grid pattern with a 3-m center-to-center spacing, giving an area replacement ratio of 8.7 percent. All the stone columns were encased with geotextiles of the best geosynthetic type for the encasement of the floating columns [20]. A 1-m-thick sand mat, acting as a working platform below the embankment (2V:1H side slopes), was established on top of the natural clay soil prior to the embankment fill to allow equipment access and to provide drainage for the columns. Furthermore, one layer of geogrid was laid to provide a basal reinforcement for the embankment.

The numerical analyses were carried out using an available PLAXIS 3D Foundation package [44]. The displacements and the vertical stresses on the column and the surrounding soil, as well as the tensile strains and tangential tensile forces acting on the geosynthetics, were calculated. The details of the cross-section of the model and the finite-element mesh are shown in Fig. 3, representing the right half of the domain on account of the symmetry.

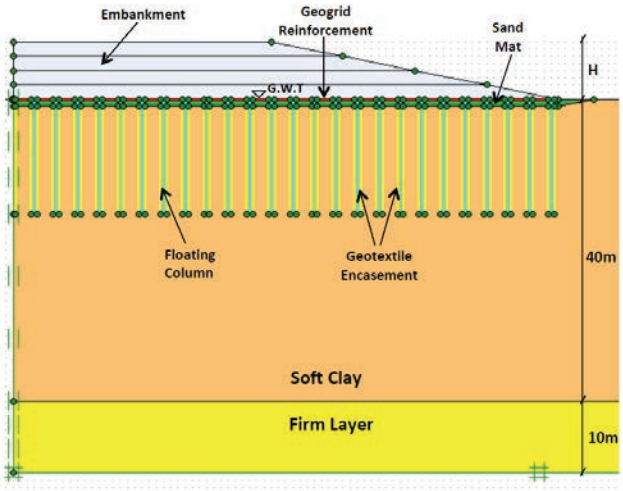

Figure 3a. Cross-section of the model.

In the analyses, the model limits were 50 m in the vertical direction and 220 m in the horizontal direction, being five times the width of half of the embankment base, so as to minimize the boundary effect. Fig. 4 shows the finite-element mesh used in the 3D numerical simulations. The soil clusters were modeled using 10-noded tetrahedral elements, whereas the geosynthetic elements are represented by 6-noded triangle surface elements. A horizontal displacement was not permitted on the vertical boundaries of the model; however, the bottom boundary was fixed securely in both the vertical and horizontal directions.

The embankment fill construction to the top surface was simulated in four stages. For each stage 20 days was envisaged for the construction of a 2-m layer and 90 days for the consolidation from its surcharge. The consolidation analyses were carried out during and after each construction stage. After the completion of the embankment construction, the calculations were continued until the excess pore-water pressure dissipation at mid-depth of the clay layer had reached 1 kPa. A closed consolidation boundary was applied to the sides of the model parallel to the embankment axis to prevent lateral drainage.

Both the embankment fill and the sand mat (assumed to be Sacramento River sand) were modeled using the Mohr–Coulomb failure criterion under a drained condition. Kaliakin et al. [45] discussed the determination of the values from experimental data for Sacramento River sand based on the tests carried out by Lee and Seed [46]. The column material was modeled as granular soil, in

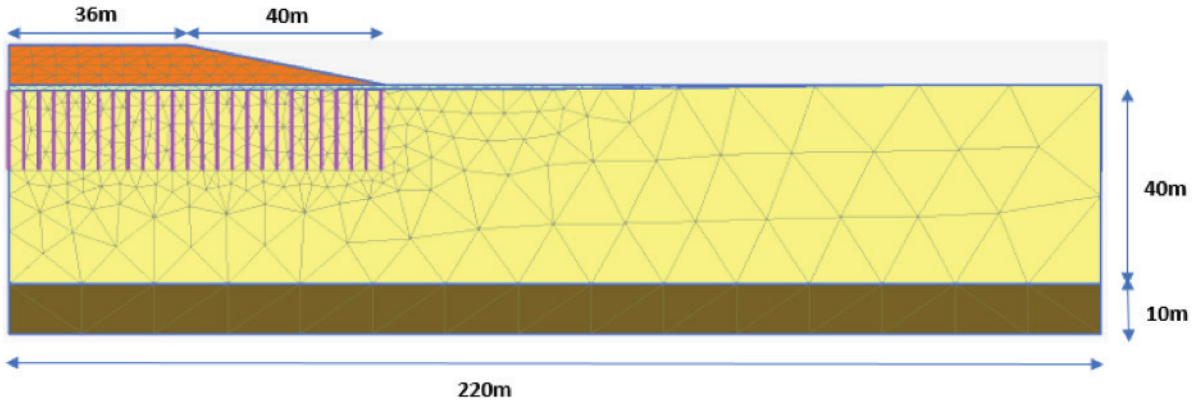

Figure 3b. Cross-section of the finite-element model.

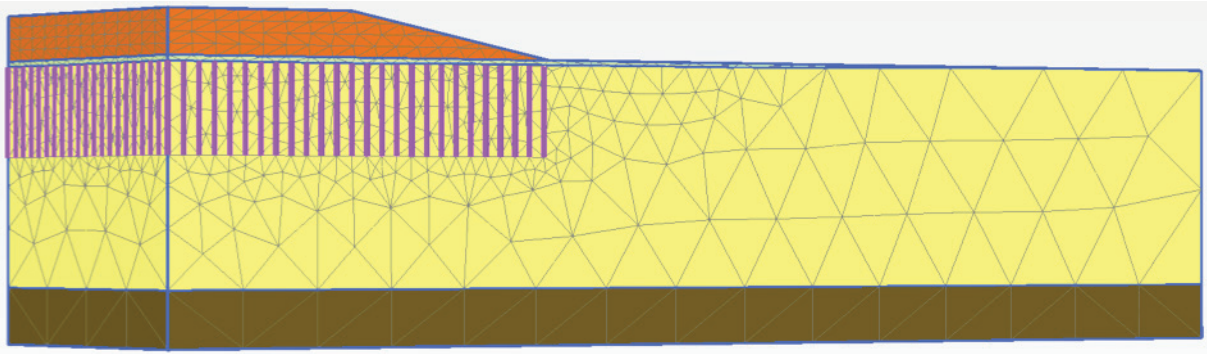

Figure 4. 3D finite-element model.

line with the suggestions of Ambily and Gandhi [47]. The soft soil was idealized using the modified Cam Clay (MCC) model. The MCC parameters considered in this study were adopted from the geotechnical parameters of soft Kebun clay soil encountered in a recent soft-ground improvement project [43]. Khabbazian et al. [37] stated that the use of the MCC model is preferable over the Mohr–Coulomb or linear elastic models, in that it allows a more accurate modeling of the behavior of the soft soil.

The geosynthetics used for both the reinforcement and the encasement were modeled as linear elastic material with no bending stiffness, as recommended by Murugesan and Rajagopal [19] and Liu et al. 2007 [13]. The stiffness of the geosynthetic reinforcement (J=EA) was determined as the tensile force at 3% elongation divided by that elongation (3%). Perfect adhesion between the stone and the surrounding soil were assumed, and thus interface elements with a rigid interface were used at the interfaces of either the stone column and the encasement, or the encasement and the soft clay [22, 23]. In fact, a large number of researchers have been investigating so much to characterize the interface working mechanism and propose fruitful achievements on the constitute models of the soil-geosynthetic interface. The parameters used in the numerical analyses are summarized in Table 1.

Stone columns are installed using vibro-displacement and vibro-replacement methods. The stone material is laterally expanded, which is accompanied by an increase in the horizontal earth pressure and the excess pore-water pressure in the soft soil during and after the column's installation. However, any influence related to the installation of the columns was disregarded in this study.

Table 1. Material parameters used in the numerical analyses.

Parameter	Column Material *Stone Soil* (Ambily and Gandhi 2007)	Embankment Fill *Sacramento River Sand* (Kaliakin 2012)	Working Platform *Sacramento River Sand* (Kaliakin 2012)	Soft Clay *Kebun Clay* (Raju 1997)
Model Type	Mohr-Coulomb	Mohr-Coulomb	Mohr-Coulomb	Modified Cam Clay
Unit Weight, γ(kN/m^3)	24	22.5	20	15
Effective Friction Angle, ϕ'(°)	42	36	32	-
Effective Cohesion, c'(kPa)	1	1	1	-
Dilation Angle, φ'(°)	10	4	3	-
Elastic Modulus, E(kPa)	55000	20000	15000	-
Poisson's Ratio, ν	0.3	0.3	0.3	0.3
Slope of Swelling Line, K	-	-	-	0.02
Slope of the Virgin Consolidation Line, λ	-	-	-	0.4
Void Ratio at Unit Pressure, e	-	-	-	1.0
Slope of the Critical State Line, M	-	-	-	1.0
Permeability, k(m/s)	1×10^{-2}	1×10^{-3}	1×10^{-3}	1×10^{-6}

In order to cover all the cases in the embankment--construction scenarios, parameters such as the embankment height (H), column-encasement stiffness (J_E), and basal reinforcement stiffness (J_R) were varied, as summarized in Table 2.

Table 2. Parameters evaluated in the parametric analyses.

Parameter					
Embankment Height, H (m)	2	4	6	8	
Geogrid Reinforcement Stiffness, J_R (kN/m)	1000	2000	3500	5000	6500
Column Length, L_C (m)	16				
Geotextile Encasement Stiffness, J_E (kN/m)	500	1000	1500	2000	2500

For the case of the 8-m-high embankment, the critical length of a floating column according to the analytical equation developed by Satibi [40] was determined as 15 m. Based on this critical length, the lengths of the columns are determined to be 16 m (L_C=16m) for the whole parametric study. A comparison is made of the surface settlement of the column and the soft soil, the column bulging, the vertical stresses on the floating column (L_C=16m) and the soft soil, and the tangential force in the geogrid reinforcement.

A similar parametric study with several variables for reinforced shallow foundations was performed by Jelušič and Žlender [48, 49].

3. RESULTS OF THE PARAMETRIC STUDY

The results of the parametric study evaluating the variation of the embankment height, column encasement and basal reinforcement stiffnesses were categorized according to the effects on the stress strain behavior of the GRCSE in the following subsections.

3.1 Surface settlement

Fig. 5 shows the surface-settlement behavior of the encased columns and the soft soil for different unreinforced embankment cases. The results reveal a significant decrease in the settlement with the encasement, which is thought to be a direct consequence of the column bulging reduction by additional confining pressure produced by the geotextile encasement along the column length. It is also clear that an increase in the stiffness of the encasement improves the performance of the GEC.

The settlement curves (Fig. 5) also indicate that geotextile encasement reduces the total settlement, but generates some differential settlement. The soft soil closer to the embankment centerline is subjected to greater vertical stresses when compared to the soil near the embankment edges, leading the settlement values to decrease with the distance from the centerline of the embankment. The value of the maximum settlement of the column close to the middle is about 30 percent greater than that of the column near the edge. The settlement response of the GECs also depends strongly on the surcharge from the embankment's self-weight. When the embankment height is less than 4.0 m (H < 4 m), the surface settlements are small.

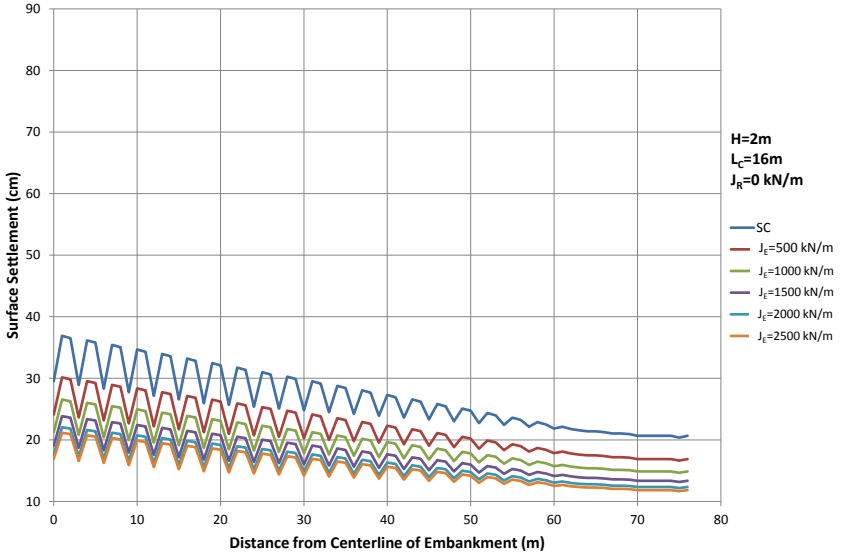

Figure 5a. Settlement profile at the base of the embankment; H=2m.

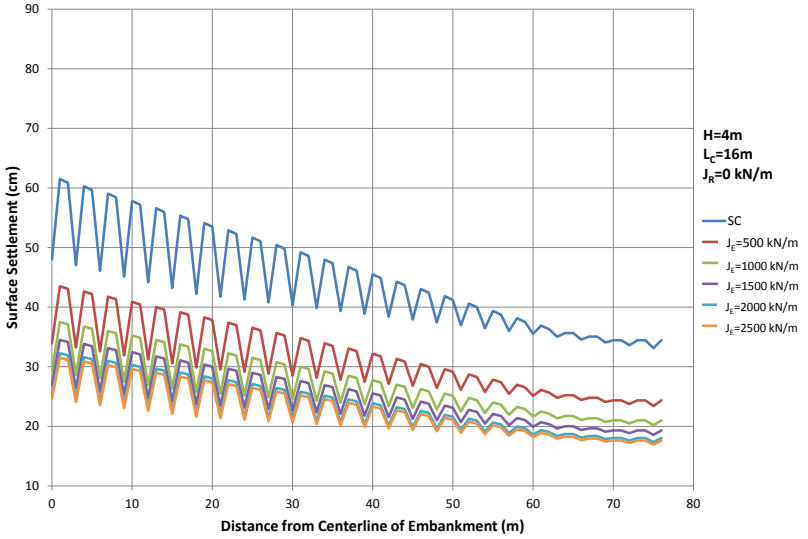

Figure 5b. Settlement profile at the base of the embankment; H=4m.

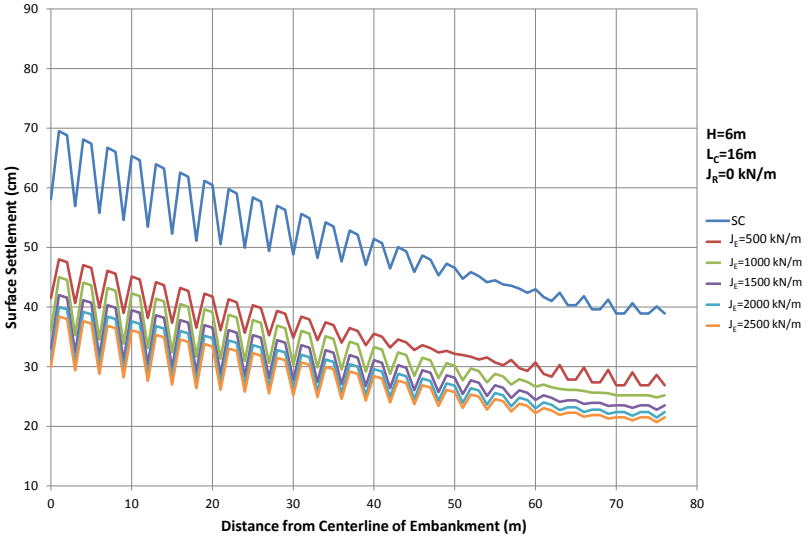

Figure 5c. Settlement profile at the base of the embankment; H=6m.

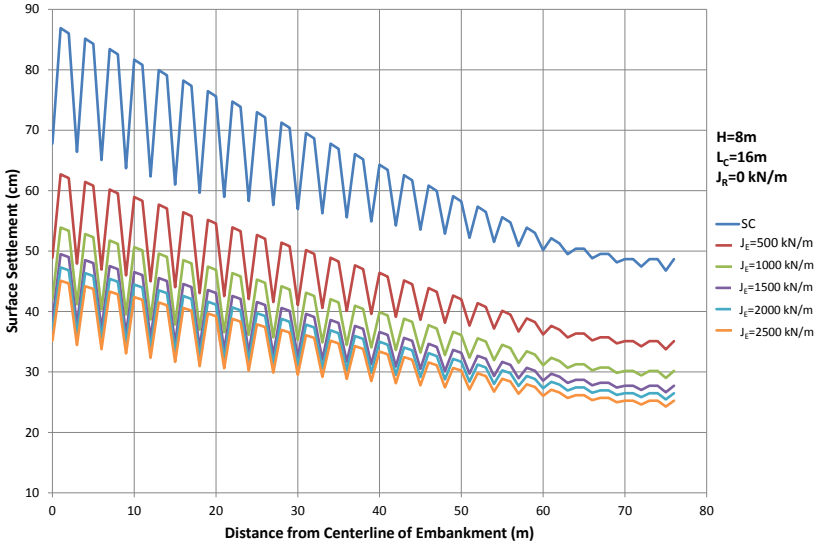

Figure 5d. Settlement profile at the base of the embankment; H=8m.

The settlement-reduction factor (β = ratio of the settlement for stabilized soft clay over the settlement of untreated soft clay) is almost equal to 0.82 (H=2 m) when the encased column (J_E=500 kN/m) is used. For H=2 m, the average settlement value on the soil decreases by 17 percent, and on the column by 18 percent. As the stiffness value of the encasement increases, β decreases to 0.49. For small stiffness values of the encasement ($J_E \leq$ 1500kN/m), β decreases gradually, while for higher stiffness values, it remains approximately constant (Fig. 6).

Fig. 7 illustrates the surface-settlement behavior of the encased columns (J_E=500kN/m) and the soft soil in the case of the reinforced embankment base. For H=2 m, the settlement value of the soil in the center of the embankment decreased from 15.8 cm to 10.4 cm, and of the column from 11.8 cm to 7.8 cm. The results show that the surface-settlement values of the soft soil and the column with the base reinforcement reduced by 35 and 34 percent, respectively. Keeping the stiffness value of the encasement constant, if the reinforcement stiffness increases, the settlement value decreases, as would be expected. For low stiffness values of the basal reinforcement, the settlement value decreases much more significantly, while for higher values, the settlement change becomes less noticeable and remains approximately

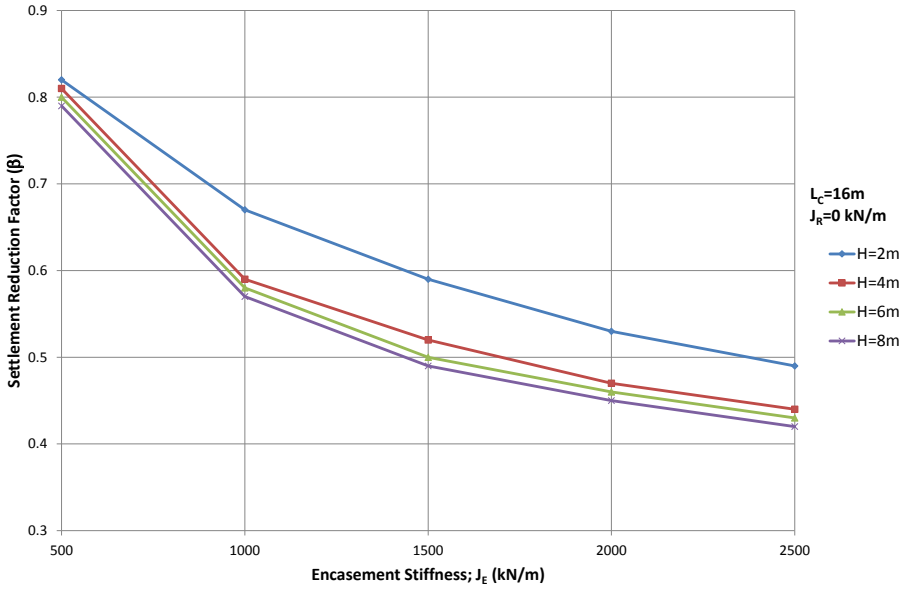

Figure 6. Variation of the settlement reduction ratio with the encasement stiffness.

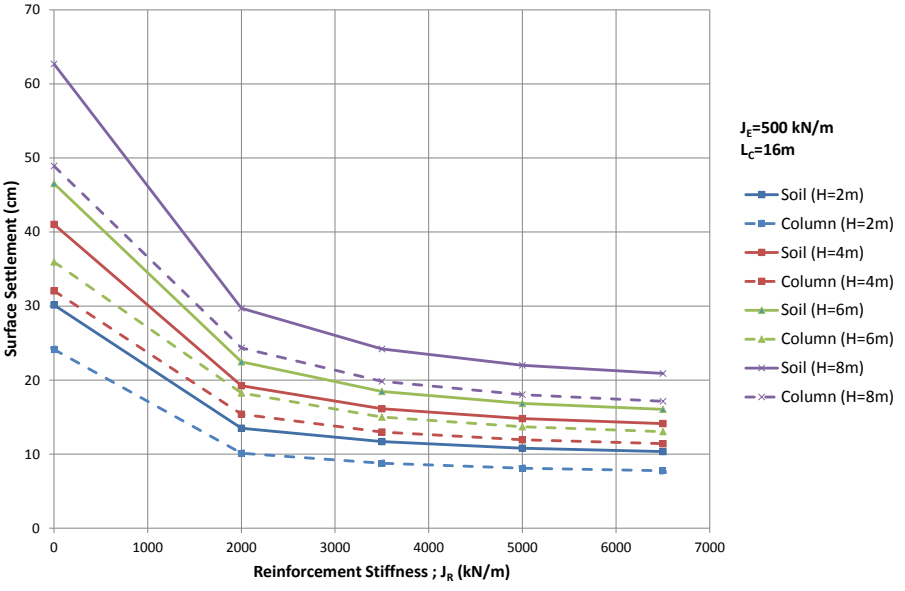

Figure 7. Variation of the settlement with the load intensity relative to the reinforcement stiffness.

constant. This means that although the geogrid has a positive effect on reducing the settlement of the soft soil beneath the embankment, this effect does not increase as the stiffness of the geogrid increases.

3.2 Lateral displacement of the columns

An encased column offers greater resistance to bulging as a result of the mobilized tangential stresses in the geotextile; consequently, higher stresses are transferred to greater depths, resulting in a decrease in the bulging [24-26]. The lateral displacements of the SC and GEC with different encasement-stiffness values under different surcharges are shown in Fig. 8. The column is displaced laterally within the soft soil as a result of loading, especially in the upper part. For H=2m, the SC exhibits considerable lateral bulging (12.4 mm), whereas the maximum lateral bulging of the GEC is limited (1.5 mm). However, after a depth of 1D, the GEC experienced more lateral displacement than the SC. This is attributed to the column confinement and the stress redistribution within the GEC [30].

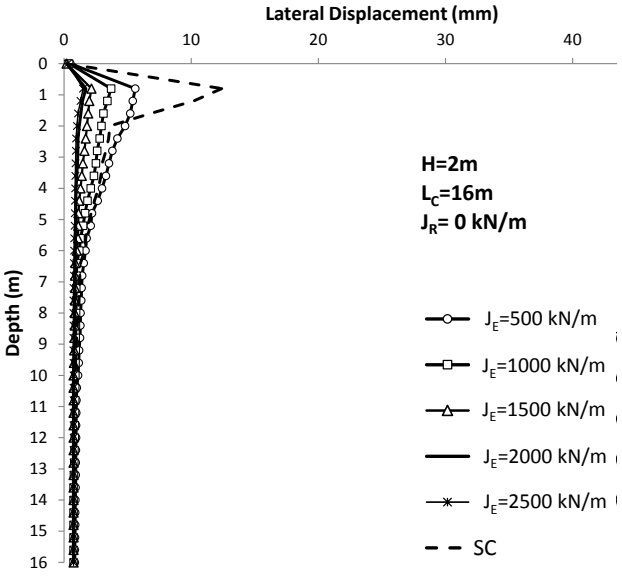

Figure 8a. Lateral displacement distribution of the columns at the end of the consolidation; H=2m.

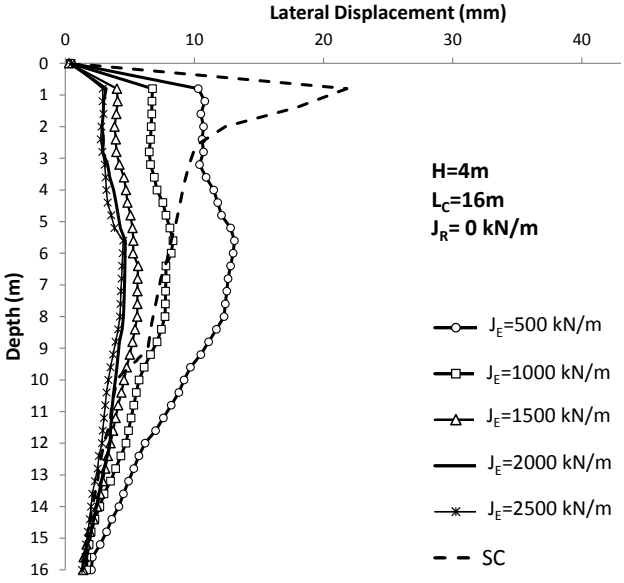

Figure 8b. Lateral displacement distribution of the columns at the end of the consolidation; H=4m.

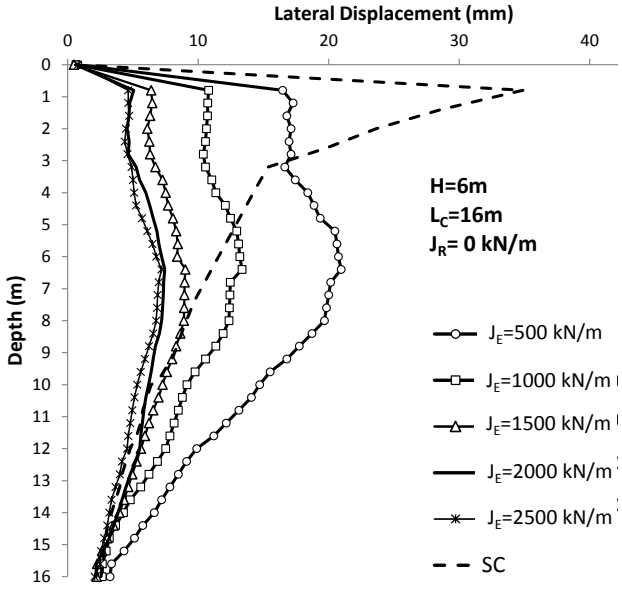

Figure 8c. Lateral displacement distribution of the columns at the end of the consolidation; H=6m.

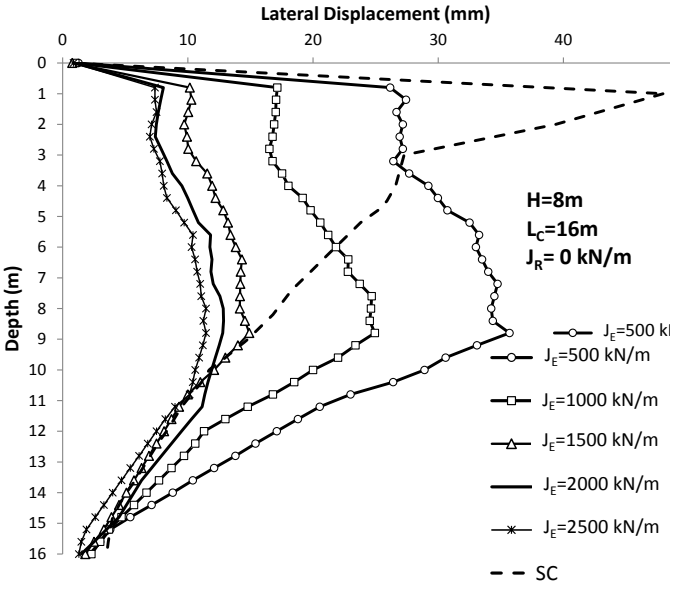

Figure 8d. Lateral displacement distribution of the columns at the end of the consolidation; H=8m.

Fig. 8 also shows that increasing the encasement stiffness up to 1500 kN/m results in a decrease in the lateral displacement; however, for higher stiffness values, the change in the lateral displacement is insignificant. It is clear that the bulging along the column increases with increasing load, causing more stress transfer to the lower depths during consolidation. For a relatively low embankment height, the bulging occurs mainly in the upper 1.5D zone. As the embankment height increases, the bulging zone extends downwards, with the maximum lateral displacement occurring at 8D below the top of the column. This finding is noteworthy, in that other researchers have previously attempted to find a specific value for the optimum length of the geosynthetic [24, 25]. This trend shows that an efficient design for an optimum encasement depth is related to the surcharge from the embankment, the column and the soft soil properties, and so full encasement could be necessary to ensure a bulging reduction.

3.3 Vertical stress below the embankment

After the completion of the construction, vertical stresses on the soft soil decrease with consolidation as a result of the redistribution of the forces. In contrast, vertical stresses on the encased columns continue to an increase during consolidation. This load transfer from the soil to the column can be quantified using a stress-concentration ratio (SCR), defined as the ratio of an average vertical stress on top of a column to the average vertical stress on the top of soft soil. The SCR plays a substantial role in reducing the stress in the soil, which leads to the settlement reduction. As the degree of load transfer between the column and the soil depends largely on the stiffness ratio between the column and the subsoil, the SCR can be expected to be larger for a GEC than for a SC. Experimental studies made on non-encased columns [21] demonstrate that the SCR on the whole varies between 2 and 3, but can reach 20 in some cases of geosynthetic-encased granular columns. Typical reported values of the SCR for piled embankments (without geogrid reinforcement) range from 1 to 8 [50, 51]; however, the calculated SCR in this study varies between 1.2 and 3.2, which contradicts previous studies [22, 23, 25]. This value can be explained by means of using the sand-working platform instead of applying the embankment load directly onto the soft soil. The presence of the sand working platform, the higher the embankment transfer from the embankment to the surrounding soil, a result of which is that the SCR remains lower than expected. The relationship between the SCR and the reinforcement stiffness is presented in Fig. 9.

As can be seen from Fig. 9, the vertical stresses on both the encased column and the surrounding soil increase as the embankment height increases, and the rate of the increase is higher for a reinforced case, pointing to the fact that basal reinforcement is highly effective in promoting the arching. The effect of reinforcement (referring to reinforcement stiffness) becomes more remarkable when the surcharge is greater. British Standard BS8006-1:2010 "Code of practice for strengthened/reinforced soil and other fills" implements the design for a geosynthetic reinforced-pile-supported embankment to evaluate the stress-reduction ratio, which represents

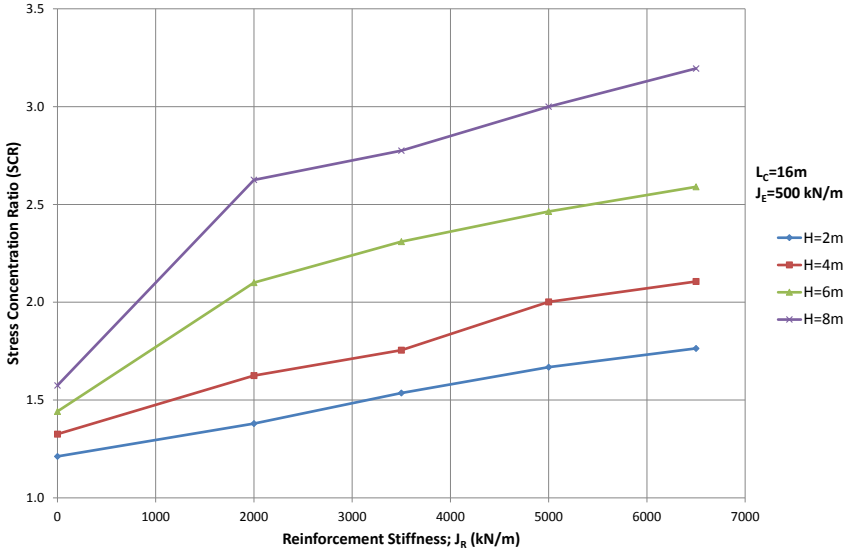

Figure 9. Variation of the stress-concentration ratio load intensity relative to the reinforcement stiffness.

the portion of the load from the embankment on to geosynthetics and between the piles. The computation considers factors such as the column (pile) diameter, the column spacing, the embankment fill height, the unit weight of fill used, the friction angle of the embankment and the stiffness of the geosynthetic.

3.4 Tension force in the basal reinforcement

When the soft soil settles in between the columns, the geogrid reinforcement layer elongates, resulting in a tension force that reduces the net pressure on the soft soil. The vertical stress above the geogrid layer is greater than that below the geogrid, and this effect helps the transfer the loads to the columns. The calculated tension forces along the geogrid layer decrease as the distance from the centerline of the embankment increases (Fig. 10).

The maximum computed acting force is only around 20% of the design strength of the geogrid, and this small force is consistent with the relatively small computed differential settlement between the column and the soil. The maximum tension force in the geogrid increases with its tensile stiffness (Fig. 11). The largest strain of the geogrid is 3%, which is in accordance with the suggested strain values [52, 53].

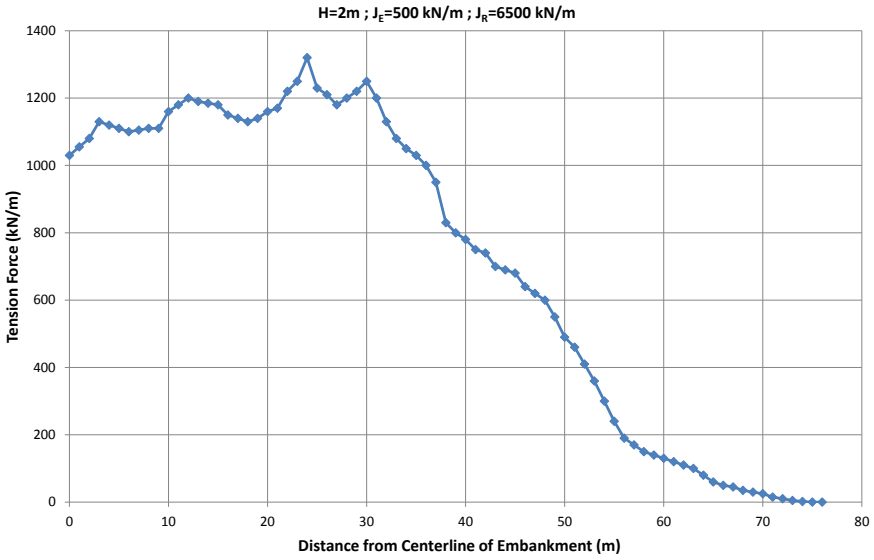

Figure 10. Distribution of the tension force along the geogrid layer (H=2m, J_E=500kN/m, J_R=6500kN/m).

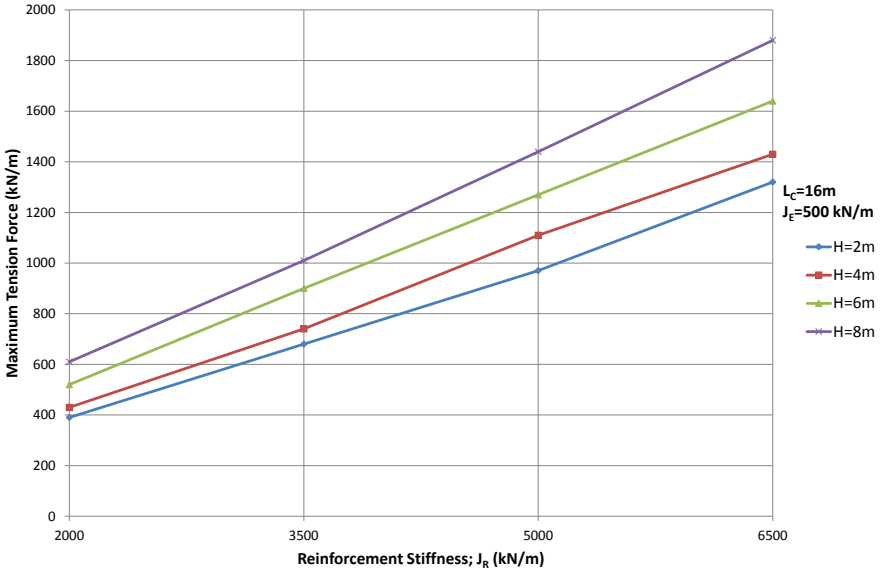

Figure 11. Influence of the reinforcement stiffness on the tension force.

4 CONCLUSIONS

This paper presents a numerical analysis of hypothetical reinforced embankments supported by floating geosynthetic-encased columns. The effects of the basal geogrid reinforcement and the geotextile encasement on the long-term behavior of the modelled geosynthetic reinforced and column-supported embankments are investigated. The following conclusions can be drawn:

1) Surface settlements on both the columns and the soft soil depend on the embankment height.

2) Encasement offers to the columns an increase in the radial stiffness, resulting in a decrease in the columns' bulging. An increase in the encasement stiffness results in a decrease in the lateral column displacement; however, when the stiffness exceeds a certain limiting value, which depends on several aspects, any further decrease in the lateral displacement becomes insignificant. The bulging along the column increases with increasing load, and the bulging zone extends downwards to greater depths during the consolidation. This trend shows that the efficiency of the encasement length is related to the surcharge and the strength properties of the column and the soil.

3) The higher is the stiffness of the basal geogrid reinforcement, the higher is the settlements reduction; however, this relationship is non-linear and similarly like for the encasement stiffness, there is a certain limiting stiffness above which the settlement reduction becomes insignificant.

4) The calculated stress-concentration ratio (SCR) is lower than that recorded in previous studies, which can be attributed to the level of the contribution of the area-replacement ratio, the sand working platform thickness to the column spacing ratio and the fact that the columns are floating and not supported firmly on the base.

5) The maximum computed tensile force in the basal geogrid is consistent with the relatively low computed differential settlement between the columns and the soil. The calculated tensile forces along the geogrid layer decrease as the distance from the center of the embankment increases, i.e., as the surcharge decreases. The maximum tensile force in the geogrid increases in parallel with its tensile stiffness.

Acknowledgments

The authors would like to thank Prof. Ivan Vaníček for his constructive reviews and valuable support throughout the study.

REFERENCES

[1] Hughes, J.M.O., Withers, N.J., Greenwood, D.A. 1975. Field trial of reinforcement effect of a stone column in soil. Geotechnique 25(1), 31–44. doi: 10.1680/geot.1975.25.1.31

[2] Barksdale, R.D., Bachus, R.C. 1983. Design and construction of stone columns. Report FHWA/RD-83/026, National Information Service, Springfield, Virginia.

[3] Borges, J.L., Marques, D.O. 2011. Geosynthetic-reinforced and jet grout column-supported embankments on soft soils: Numerical analysis and parametric study. Computers and Geotechnics 38(7), 883-896. doi: 10.1016/j.compgeo.2011.06.003

[4] Vanicek, I., Vanicek, M. 2008. Earth structures in transport, water and environmental engineering. Springer, Netherlands.

[5] Kempfert, H.G., Stadel, M., Zaeske, D. 1997. Design of geosynthetic-reinforced bearing clayers over piles. Bautechnik 74(12), 818–825.

[6] Raithel, M., Kempfert, H.G. 2000. Calculation models for dam foundations with geotextile-coated sand columns. In Proceedings of International Conference on Geotechnical and Geological Engineering, GeoEng 2000, Melbourne, Australia.

[7] Raithel, M., Kempert, H.G., Kirchiner, A. 2002. Geotextile-encased columns (GEC) for foundation of a dike on very soft soils. Geosynthetics – State of the Art Recent Developments, Delmas, P., Gourc, J. P. & Girard, H., Editors, Balkema, Rotterdam, the Netherlands, pp. 1025–1028.

[8] Raithel, M., Kirchner, A., Schade, C., Leusink, E. 2005. Foundation of construction on very soft soils with geotextile encased columns – state of the art. In Contemporary Issues in Foundation Engineering, Anderson, J. B., Phoon, K. K., Smith, E., Loehr, J. E. ASCE, Reston, VA, USA, Geotechnical Special Publication 131.

[9] Alexiew, D., Brokemper, D., Lothspeich, S. 2005. Geotextile Encased Columns (GEC): load capacity, geotextile selection and pre-design graphs. In Contemporary Issues in Foundation Engineering,

[10] Murugesan, S., Rajagopal, K. 2007. Model tests on geosynthetic encased stone columns. Geosynthetics International 14(6), 346–354. doi: 10.1680/

gein.2007.14.6.346
[11] De Mello, L.G., Mondolf, M., Montez, F., Tsukahara, C.N., Bilfinger, W. 2008. First use of geosynthetic encased sand columns in South America. Proceedings of 1st Pan-American Geosynthetics Conference, Cancu´n Mexico, Industrial Fabrics Association International, Roseville, MN, USA, pp. 1332–1341.
[12] Ayadat, T., Hanna, A.M. 2005. Encapsulated stone columns as a soil improvement technique for collapsible soil. Ground Improvement 9(4), 137–147. doi: 10.1680/grim.2005.9.4.137
[13] Liu, H. L., Ng, C.W.W., Fei, K. 2007. Performance of a geogrid reinforced and pile-supported highway embankment over soft clay: case study. Journal of Geotechnical and Geoenvironmental Engineering 133(12), 1483–1493. doi: 10.1061/(ASCE)1090-0241(2007)133:12(1483)
[14] Murugesan, S., Rajagopal, K. 2010. Studies on the behavior of single and group geosynthetic encased stone columns. Journal of Geotechnical and Geoenvironmental Engineering 136(1), 129-139.
[15] Ali, K., Shahu, J.T., Sharma, K.G. 2012. Model tests on geosynthetic-reinforced stone columns: A comparative study. Geosynthetics International 19(4), 292–305. doi: 10.1680/gein.12.00016
[16] Yoo, C., Lee, D. 2012. Performance of geogrid-encased stone columns in soft ground: full-scale load tests. Geosynthetics International 19(6), 480 –490. doi: 10.1680/gein.12.00033
[17] Hosseinpour, I., Almeida, M.S.S., Riccio, M. 2015. Full-scale load test and finite-element analysis of soft ground improved by geotextile-encased granular columns. Geosynthetics International 22(6), 428-438. doi: 10.1680/jgein.15.00023
[18] Lee, C. J., Bolton, M.D., Al-Tabbaa, A. 2002. Numerical modeling of group effects on the distribution of drag loads in pile foundations. Geotechnique 52(5), 325-335.
[19] Murugesan, S., Rajagopal, K. 2006. Geosynthetic-encased stone columns: Numerical evaluation. Geotextiles and Geomembranes 24(6), 349–358. doi: 10.1016/j.geotexmem.2006.05.001
[20] Yoo, C., Kim, S.B. 2009. Numerical modeling of geosynthetic encased stone column-reinforced ground. Geosynthetic International 16(3), 116–126. https://doi.org/10.1680/gein.2009.16.3.116
[21] Gniel, J., Bouazza, A. 2009. Improvement of soft soils using geogrid encased stone columns. Geotextiles and Geomembranes 27(3), 167–175. doi: 10.1016/j.geotexmem.2008.11.001
[22] Yoo, C. 2010. Performance of geosynthetic-encased stone columns in embankment construction: Numerical investigation. Journal of Geotechnical and Geoenvironmental Engineering 136(8), 129–139.
[23] Khabbazian, M., Kaliakin, V.N., Meehan, C.L. 2011. Performance of quasilinear elastic constitutive models in simulation of geosynthetic encased columns. Computers and Geotechnics 38(8), 998–1007.
[24] Elsawy, M.B.D. 2013. Behavior of soft ground improved by conventional and geogrid-encased stone columns, based on FEM study. Geosynthetics International 20(4), 276–285. doi: 10.1680/gein.13.00017
[25] Almeida, M.S.S., Hosseinpour, I., Riccio, M. 2013. Performance of a geosynthetic-encased column (GEC) in soft ground: Numerical and analytical studies. Geosynthetics International 20(4), 252–262. doi: 10.1680/gein.13.00015
[26] Hosseinpour, I., Riccio, M., Almeida, M.S.S. 2014. Numerical evaluation of a granular column reinforced by geosynthetics using encasement and laminated disks. Geotextiles and Geomembranes 42(4), 363–373. doi: 10.1016/j.geotexmem.2014.06.002
[27] Yoo, C. 2015. Settlement behavior of embankment on geosynthetic-encased stone column installed soft ground - A numerical investigation. Geotextiles and Geomembranes 43, 484-492. doi: 10.1016/j.geotexmem.2015.07.014
[28] Van Eekelen, S.J.M., Bezuijen, A. 2008. Considering the basic starting points of the design of piled embankments in the British Standard BS8006. In: Proceedings of EuroGeo4 p.p. 315, September 2008, Edinburgh, Scotland.
[29] EBGEO 2010. Recommendations for Design and Analysis of Earth Structures using Geosynthetic Reinforcements, German Geotechnical Society (DGGT), Berlin, Germany.
[30] Alexiew, D., Raithel, M., Kuster, V., Detert, O. 2012. 15 years of experience with geotextile encased granular columns as foundation system. ISSMGE-TC 211 Int. Symp. on Ground Improvement IS-GI, ISSMGE TC211 and BBRI, Brussels, Belgium.
[31] Han, J., Gabr, M.A. 2002. Numerical analysis of geosynthetic reinforced and pile-supported earth platforms over soft soil. Journal of Geotechnical and Geoenvironmental Engineering 128(1), 44–53. doi: 10.1061/(ASCE)1090-0241(2002)128:1(44)
[32] Abdullah, C.H., Edil, T.B. 2007. Behavior of geogrid-reinforced load transfer platforms for embankment on rammed aggregate piers. Geosynthetics International 14(3), 141–153. doi: 10.1680/gein.2007.14.3.141
[33] Smith, M., Filz, G. 2007. Axisymmetric numerical

modeling of a unit cell in geosynthetic-reinforced, column-supported embankments. Geosynthetics International 14(1), 13–22. doi: 10.1680/gein.2007.14.1.13

[34] Chen, R.P., Chen, Y.M., Han, J., Xu, Z.Z. 2008. A theoretical solution for pile-supported embankments on soft soils under one-dimensional compression. Canadian Geotechnical Journal 45(5), 611–623. doi: 10.1139/T08-003

[35] Jelušič, P., Žlender, B. 2018. Optimal design of piled embankments with basal reinforcement. Geosynthetics International 25(2), 150–163. doi: 10.1680/jgein.17.00039

[36] Bhasi, A., Rajagopal, K. 2015. Numerical study of basal reinforced embankments supported on floating/end bearing piles considering pile-soil interaction. Geotextiles and Geomembranes 43, 524-536. doi: 10.1016/j.geotexmem.2015.05.003

[37] Khabbazian, M., Meehan, C.L., Kaliakin, V.N. 2015. Column supported embankments with geosynthetic encased columns: Validity of the unit cell concept. Geotechnical Geological Engineering 33, 425–442. doi: 10.1007/s10706-014-9826-8

[38] Jenck, O., Dias, D., Kastner, R. 2009. Three-dimensional numerical modeling of a piled embankment. International Journal of Geomechanics 9(3), 102–112. doi: 10.1061/(ASCE)1532-3641(2009)9:3(102)

[39] Zhang, N., Shen, S.L., Wu, H., Chai, J., Xu, Y., Yin, Z. 2015. Evaluation of effect of basal geotextile reinforcement under embankment loading on soft marine deposits. Geotextiles and Geomembranes 43, 506-514. doi: 10.1016/j.geotexmem.2015.05.005

[40] Satibi, S. 2009. Numerical analysis and design criteria of embankments on floating piles (A PhD thesis submitted to the Universitat of Stuttgart, Stuttgart, Germany).

[41] EBGEO 2010. Recommendations for Design and Analysis of Earth Structures using Geosynthetic Reinforcements, German Geotechnical Society (DGGT), Berlin, Germany. doi: 10.1002/9783433600931

[42] Van Eekelen, S.J.M., Bezuijen, A., Van Tol, A.F. 2011. Analysis and modification of the British Standard BS8006 for the design of piled embankments. Geotextiles and Geomembranes 29, 345-359. doi: 10.1016/j.geotexmem.2011.02.001

[43] Raju, V.R. 1997. The behaviour of very soft soils improved by vibro replacement. Ground Improvement Conference, London.

[44] Brinkgreve, R.B., Vermeer, P.A. 2012. PLAXIS 3D-Finite element code for soil and rocks analysis, Balkema, Rotterdam, The Netherlands.

[45] Kaliakin, V.N., Khabbazian, M., Meehan, C.L. 2012. Modeling the behavior of geosynthetic encased columns: influence of granular soil constitutive model. International Journal of Geomechanics 12(4), 357–369. doi: 10.1061/(ASCE)GM.1943-5622.0000084

[46] Lee, K.L., Seed, H.B. 1967. Drained strength characteristics of sands. J Soil Mech. Found. Div. ASCE, 93, No.6, 117–141.

[47] Ambily, A.P., Gandhi, S.R. 2007. Behavior of stone columns based on experimental and FEM analysis. Journal of Geotechnical and Geoenvironmental Engineering ASCE 133(4), 405–415. doi: 10.1061/(ASCE)1090-0241(2007)133:4(405)

[48] Jelušič, P., Žlender, B. 2018. Optimal design of reinforced pad foundation and strip foundation. International Journal of Geomechanics, 18(9). doi: 10.1061/(asce)gm.1943-5622.0001258

[49] Jelušič, P. & Žlender, B. (2018). Optimal design of pad footing based on MINLP optimization. Soils and Foundations 58(2), 277–289. doi: 10.1016/j.sandf.2018.02.002

[50] Barksdale, R.D., Goughnour, R.R. 1984. Performance of a stone column supported embankment. Proc., Int. Conf. on Case Histories in Geotechnical Engineering, St. Louis, 6–11.

[51] Greenwood, D.A. 1991. Load tests on stone columns. Proc., Deep Foundation Improvements: Design, Construction, and Testing, ASTM, Philadelphia, 148–171.

[52] Rowe, R.K., Soderman, K.L. 1985. An approximate method for estimating the stability of geotextile-reinforced embankments. Canadian Geotechnical Journal 22, 392-398.

[53] Bonapare, R., Christopher, B.R. 1987. Design and construction of reinforced embankments over weak foundations. Transportation. Research Record 1153, 26-39.

QUARTZ-SAND COMPRESSIBILITY AT HIGH STRESSES AND TEMPERATURES

STISLJIVOST KREMENOVEGA PESKA PRI VISOKIH OBREMENITVAH IN TEMPERATURI

Miriam Martín-Ruiz
Universidad Politécnica de Madrid, UPM,
Department of Continuum Mechanics and Structuress
Madrid, Spain
E-mail: miriam.martinr@alumnos.upm.es

José Alvarellos
Repsol
Madrid, Spain
E-mail: jose.alvarellos@repsol.com

Jordi Delgado
University of A Coruña,
Department of Civil Engineering
A Coruña, Spain
E-mail: jorge.delgado@udc.es

José María Goicolea
Universidad Politécnica de Madrid,
Department of Continuum Mechanics and Structures
Madrid, Spain
E-mail: jose.goicolea@upm.es

DOI https://doi.org/10.18690/actageotechslov.16.2.39-49.2019

Keywords
compressibility, particle crushing, temperature effect, high-stresses effect, subcritical cracking growth

Ključne besede
stisljivost, drobljenje delcev, temperaturni učinek, učinek visokih obremenitev, rast mejne kritične razpoke

Abstract

The effects of temperature on the degree of grain crushing and the stress-strain response of a granular soil subjected to high stresses are a matter of interest for unconventional geomechanical projects. As a part of a research program on the thermo-hydro-mechanical-chemical compressibility of quartz sand from a heavy oil reservoir, we have conducted a series of oedometric tests under dry conditions, high stresses (up to 50 MPa) and constant temperatures, ranging from 25 to 250°C. Acoustic emissions were recorded throughout the tests, and SEM photomicrographs of sieved grain-size fractions before and after the experiments were analysed.

The results show that the temperature has a negligible effect on the macroscopic compressibility, with similar oedometric curves for all the tests. Conversely, the acoustic-emission counts drop off, and changes in the particle size distribution are minor, though grains subjected at high temperature show incipient fractures attributed to subcritical cracking through stress-corrosion.

Izvleček

Za nekonvencionalne geomehanske projekte je zanimiv vpliv temperature na stopnjo drobljenja zrn in napetostno-deformacijski odziv zrnatih zemljin, izpostavljenih visokim obremenitvam. Kot del raziskovalnega programa o termo-hidromehansko-kemijski stisljivosti kremenovega peska iz težkega naftnega rezervoarja so avtorji izvedli serijo edometrskih preizkusov pri suhih pogojih, visokih obremenitvah (do 50 MPa) in konstantnih temperaturah v razponu od 25 do 250 °C. Med preizkusi so bile zabeležene akustične emisije in analizirane SEM fotomikrografije presejanih frakcij velikosti zrn pred in po preizkusih

Rezultati kažejo, da ima temperatura zanemarljiv vpliv na makroskopsko stisljivost, pri podobnih krivuljah stisljivosti za vse preizkuse. Nasprotno pa število akustičnih emisij upada in so spremembe v porazdelitvi velikosti delcev manjše, čeprav zrna, izpostavljena visoki temperaturi, kažejo začetne lome, ki se pripisujejo mejnemu kritičnemu razpokanju zaradi napetostne korozije.

Thus, the compressibility of the samples tested at high and low temperatures can be explained within the same grain-scale mechanisms of cracking: critical rapid Herzian crack growth, at low temperatures, and subcritical silent crack growth by stress-corrosion, at the higher temperatures.

Tako lahko stisljivost vzorcev, preizkušenih pri visokih in nizkih temperaturah, razložimo z enakimi mehanizmi razpokanja v velikosti zrna: kritična hitra Hertzianova razpoka raste pri nizkih temperaturah, medtem, ko mejna kritična tiha razpoka zaradi napetostne korozije raste pri višjih temperaturah.

1 INTRODUCTION

While geotechnical practice does not typically require a knowledge of temperature effects, emerging geoenvironmental and geomechanical applications require a knowledge of the grain crushing in soils and granular materials under high stresses and temperatures. Examples of this kind are thermal oil recovery in petroleum engineering, CO_2 capture and storage (CCS), storage of radioactive waste and unconventional foundations or structures.

The compressibility and crushing of quartz sand at high pressures, considered either as an assembly of single particles or as a bulk skeleton, have been examined using compression (or oedometric) data for quartz sands, plotted as e – logσ_v curves and the identification of a stress threshold that leads to a steepening of its slope at high stresses.

While large stresses have been achieved, the effects of temperature on compressibility and grain cracking require further study. The point of maximum curvature, commonly known as the yield point, is a stress level that marks the onset of particle crushing. Particle rearrangement and packing are the main sources of strains at low loads (conventional geotechnics); as the stress increases, the early asperity damage leads to particle splitting. Beyond that stress threshold, the compression curve fits into a linear relationship in the semi-log plot, called the normal (or virgin) compression line [1-5], which can be thought of as a "degenerated-by-crushing" normal compression line (provided the tests can be carried out at room temperature), in contrast to the classic concepts.

The initial void ratio, grain shape, size, and grading govern the compressibility of quartz sands and, particularly, the yield point [5-11]. The high rates of loading intensify the grain crushing as well [12-17].

Related processes have been dealt with, on the one hand, in the scope of Earth Sciences, such as the diagenetic compaction of natural sediments [18-24] and the behaviour of cataclastic zones [25].

2 PURPOSE AND EXPERIMENTAL PROGRAM

Here, we examine the coupled thermo-hydro-mechano-chemical response of quartz sand, saturated with brine and oil, and apply the results to reservoirs in the Orinoco Heavy Oil Belt of Venezuela. A series of 20 compression tests at high stresses (up to 50 MPa) were performed over a range of constant temperature (from 25 to 250°C) in a special oedometric apparatus. Dry conditions were required to assess the effect of the temperature on the sand compressibility at high stresses. In addition, acoustic emissions (AEs) were recorded throughout the oedometric tests, since crushing is the basic acoustic source expected. The samples were examined using a scanning electron microscope (SEM) and an optical microscope.

3 MECHANICAL RESPONSE OF SAND AGGREGATES

When a sand aggregate is subjected to high stresses at room temperature in an oedometric cell, three compressional curvatures or stages can be distinguished along the oedometric curve, as shown in Fig. 1, from [26, 27 and 28].

Particle rearrangement, Stage I

The curvature of the oedometric curve in this stage accounts for the primary compressibility, caused by particle rearrangement, up to the maximum particle packing. Despite the highly constrained conditions of the oedometric cell (radial strains remain zero), the maximum density (maximum packing) is reached as long as the vertical stress is raised up to an intermediate level (5–10 MPa). Hence, the curvature and the slope during this stage depend on the original grain size distribution, the grain morphology and the initial void ratio.

Yield point, Stage II

Once the maximum particle packing is reached, the potential grain movement is completely frustrated and blocked; this state is commonly known as the yield point. The applied stresses are transmitted as discrete

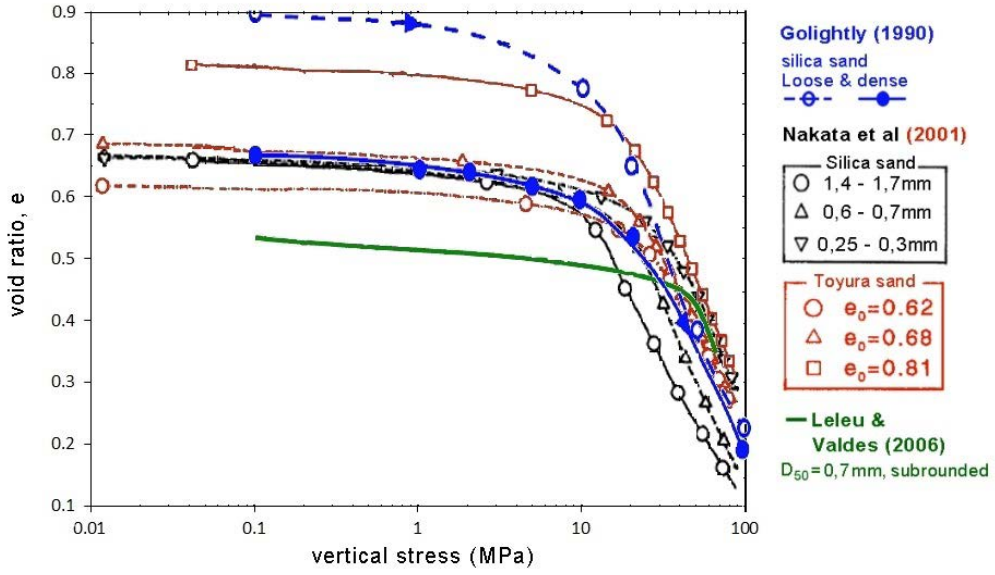

Figure 1. Oedometric curves of quartz sand at high stresses and room temperature (from [26, 27 and 28]).

forces along the grain contacts within the soil skeleton [29]. Therefore, further strains can only occur as a result of particle crushing, which can be addressed appropriately with the concurrence of the following theories.

Hertzian contact theory and critical pressure

Macroscopic yielding depends on the crack initiation at loaded grains and can be examined on the scale of individual contacts between pairs of grains according to the Hertzian theory for loaded spherical bodies. The contact area of the loaded spherical bodies is circular and its radius $\left(\frac{d_c}{2}\right)$ depends on the normal force applied (F_n), the grain radii (R) and the Young's moduli (E), given by Equation 1 for two identical grains (adapted from [30]).

$$\frac{d_c}{2} = \left(\frac{3\,F_n\,R}{4\,E}\right)^{1/3} \qquad (1)$$

Even though relevant research efforts in the field of granular media have been made during the past decade to establish the relationship between the macroscale ("Terzaghian" effective) stresses and the microscale (particulate level) stresses, the simplified equation for monosized spheres (Eq. 2) suffices for the purpose of the current research [31 and 32]. The total normal force applied at the contact (F_n) can be expressed as a function of the grain size (d), the normal applied stress (σ) and the void ratio (e).

$$Fn = \sigma(d)^2\,\frac{\pi(1+e)^2}{12} \qquad (2)$$

The mean intergranular stress at the grain contacts (σ_{int}) can be expressed according to Equation 3.

$$\sigma_{\mathrm{int}} = \left(\frac{\mathrm{F_n}}{\pi\left(\frac{\mathrm{d_c}}{2}\right)^2}\right) \qquad (3)$$

Taking into account that the intergranular stress is several orders of magnitude higher than its corresponding effective stress, grains are likely to crush beyond the yield point (with intergranular stresses in the range of 1GPa), leading to a reduction of the mean grain size and the production of fines.

The Hertzian maximum tensile radial stress at the contact (σ_t) reaches its maximum value at the edge of the circular contact area.

$$\sigma_t = \frac{(1-2\nu)\sigma_{int}}{2} \qquad (4)$$

The Mode-I stress-intensity factor governs the development of this kind of cracking at the tip of the crack [33], K_I, and follows equation 5 [33 and 34], where c is the length of a pre-existing flaw.

$$K_I = 1.12\,\sigma_t\sqrt{\pi c} \qquad (5)$$

The crack growth that can ultimately cause the grain failure will only occur if the stress-intensity factor on the tip of the crack reaches the value of the fracture toughness.

$$K_I = K_{IC} \qquad (6)$$

Thus, if the Hertzian and the fracture-mechanics models are combined, the pressure of breakage (P_{cr}) [13] can be obtained, which depends on the grain radius, the elastic parameters (E and ν), the porosity (n), or the void ratio, and the properties of the fracture mechanics (K_{IC}, the

fracture toughness and c, the length of the initial pre-existing flaw).

$$\frac{P_{cr}}{E} = 2.2\frac{(1-\nu^2)^2}{(1-2\nu)^3}\left(\frac{K_{IC}}{E}\right)^3(\alpha nR)^{\frac{-3}{2}} \qquad (7)$$

$$\alpha = \frac{c}{R} \qquad (8)$$

Since α is approximately 3.6×10^{-5} for most porous soils [13] and the range of variation of porosity (or void ratio) is relatively narrow, the onset of grain crushing, i.e., when σ_t reaches P_{cr}, is just a function of the grain radius. Thus, the coarser the grains are, the lower the critical pressure of breakage.

Note that, leaving the formulation itself aside, the smaller the particles, the lower the likelihood of the presence of a pre-existing flaw and, therefore, any further development of the crushing.

The microscopic and the macroscopic realms can be connected, and the tensile stress on a particle embedded in a soil matrix due to the normal stress depends on the void ratio [32].

$$\sigma_t = \sigma\left(\frac{(1+e)\pi}{6}\right)^{\frac{2}{3}} \qquad (9)$$

Moreover, Field [34], who studied granular assemblies of rounded stones with different sizes and gradings, concluded that the coordination number (the average number of contact points per particle, C_n) varies inversely with the void ratio, as shown in Equation 10.

$$C_n = \frac{12}{1+e} \qquad (10)$$

Hence, the tensile stress on a particle in a soil matrix decreases, as shown Equation 11, as the coordination number increases.

$$\sigma_t = \sigma\left(\frac{2\pi}{C_n}\right)^{\frac{2}{3}} \qquad (11)$$

Particle breakage and interparticle slip (no thermally induced effect), Stage III

From the moment the overloaded particles start to break, a crushing knock-on effect is triggered, and the compressibility curve shifts to a steeper "degenerated-by-crushing" virgin compression line due to particle crushing and interparticle slip.

Uniform soils made up of coarse particles are more prone to crushing than soils made of finer particles of the same

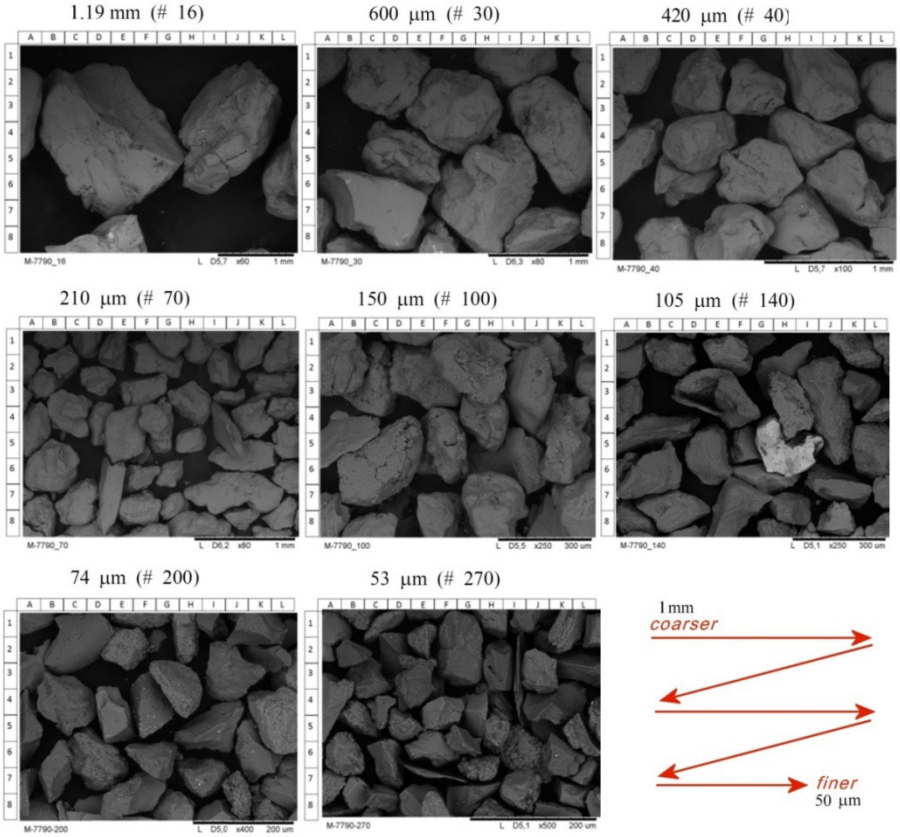

Figure 2. SEM photomicrographs of 8 sieved fractions after cleaning.

material [3, 6, 7, 9 and 10]. Likewise, angular particles are more crushable than rounded particles [3, 7 and 9] as their intergranular stresses tend to be more localised and the asperities favour the locking effect, preventing further packing. Besides, uniform soils exhibit more crushing than well-graded soils having the same maximum size [3 and 9].

Much of our understanding of the compressibility of sand aggregates is restricted to room-temperature loading. This paper takes the theoretical framework of room-temperature compaction, and we examined the compaction at higher temperatures.

4 MATERIAL AND METHODS

4.1 Quartz-sand preparation and characterisation

The sand samples were retrieved from an oil well at a depth of approximately 1000 m. They are fine-grained (D_{50}≈210 μm), uniform (c_u≈1.8), uncemented sands, composed of quartz. Prior to testing, oil and any other impurities were removed according to the following cleaning guidelines: thorough acid-washing (36 wt. % HCl); rinsing with deionised water, and re-washing (96 wt. % ethylic alcohol). Finally, the sand samples were oven-dried. The SEM photomicrographs of 8 different sieved fractions after cleaning are shown in Fig. 2. The photomicrographs suggest that the coarser fractions contain sub-rounded grains and that grains with finer fractions consist of sharp angular particles.

4.2 Sample preparation and description of the oedometric apparatus

The sand samples were poured into a thin-walled (1.3 mm) sample holder of 40 mm outer diameter (OD). The sand was meant to be placed in its loosest state and a target height of 12 mm, although a settling pressure of 0.2 MPa was applied before testing for the sake of sample homogenization. Even though a strict procedure of placement of the sand was followed, some scattering of the initial void ratio (from 0.72 to 0.85) was unavoidable. Nevertheless, as will be shown, this variation had little effect on the compressibility at high stresses (beyond the yield point). Fig. 3 illustrates the sample preparation.

Figure 3. Sample preparation of the one-dimensional compression tests.

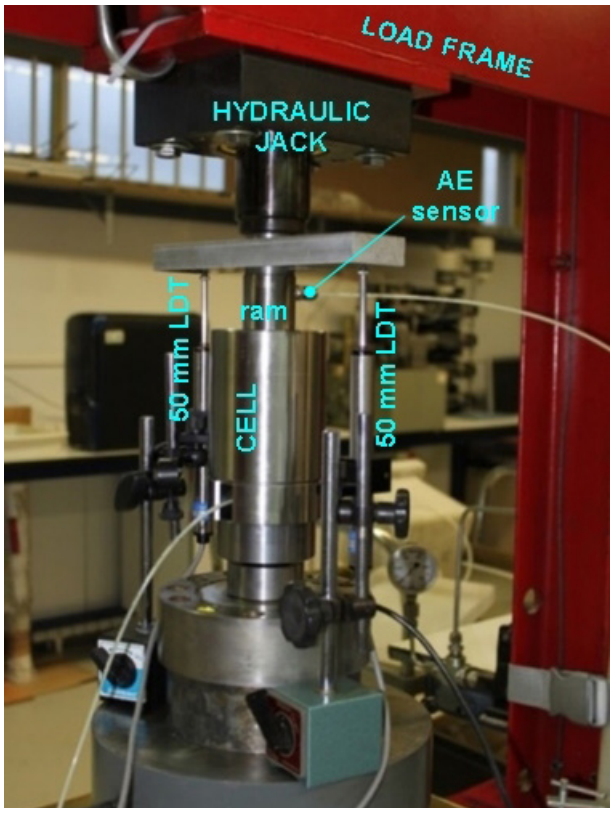

Figure 4. One-dimensional compression (oedometric) apparatus during testing.

The sample holder is fitted into an oedometric cell that consists of a stainless-steel cylinder with a 24.5-mm-thick wall. The oedometric cell is placed in a rigid load frame (Fig. 4). The axial load is applied by a servo-controlled hydraulic jack, acting at the selected loading rate. The axial displacement is measured by two external, averaged, LDT-type transducers, whereas the axial load is recorded by the built-in data-acquisition system of the hydraulic jack. Two band heaters are used to raise the temperature and keep it constant during the tests. They are connected to a PID temperature controller, and a PT100 sensor located in the middle of the inner cell wall was used. When necessary, thermal isolation blocks are placed around the cell (Fig. 5). A PAC-Micro200HF wideband acoustic emission sensor attached to the ram of the hydraulic jack records the acoustic events occurring within the sample (basically, crushing counts). The data are recorded with a Physical Acoustics Co. PCI-2 and the software AEwin for PCI r.2.1. As the sensor withstands just up to 177°C, acoustic emissions (AEs) data were recorded only for the tests at temperatures not exceeding 150°C.

4.3 Calibration for high temperatures and stresses

Several calibrations were carried out. An additional PT100 was required for the calibration of the tempera-

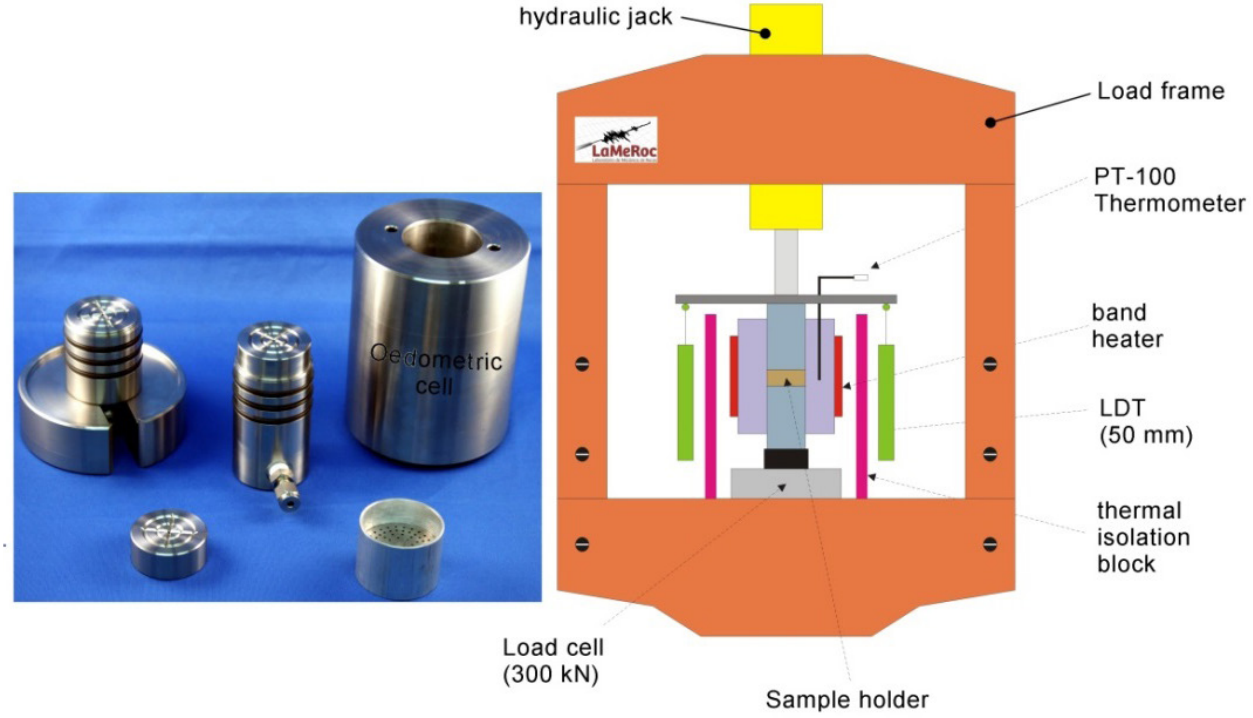

Figure 5. Layout of the oedometric apparatus.

ture. In the first stage of the temperature rise (from 25 to 109°C), an axial thermal expansion of 0.176 mm was recorded over the initial length (140.2 mm), while in a second stage (from 109 to 223°C), this expansion reached 0.284 mm.

Displacements were determined for the whole mechanical assembly (250 mm in height, including the load column) caused by the application of axial stress (from 0.1 to 50 MPa). A shortening of 0.613 mm was measured at 109°C, while a shortening of 0.534 was measured at 223°C. This difference in shortening (0.09 m) is attributed to the differential fitting of the O-rings into the oedometric cell. These calibration measurements yielded the linear thermal expansion coefficients, and the Young's moduli of the parts (perforated steel discs, positioning reference blocks, steel compression platens and refractory ceramic blocks to protect the load cell).

4.4 Stress paths of the oedometric tests

Prior to any loading, the sand samples were heated up to the target temperature. Once the samples reached it, the axial load was applied in three stages:

- a 10-step monotonic loading (0.2 / 1 / 2 / 3 / 4 / 6 / 10 / 15 / 20 / 25 / 30 MPa);
- a 4-step unloading/reloading loop (30 / 10 / 1 / 30 / 50 MPa);
- a 4-step monotonic unloading (50 / 30 / 15 / 5 / 1 MPa).

Each step of the loading increase or decrease was reached in seconds or a few minutes and maintained for 90 minutes. Hence, a whole oedometric test took approximately 28 h.

5 RESULTS

Fig. 6 shows 3 characteristic oedometric curves at different temperatures (25, 100 and 150°C) in which the AE data were recorded during the tests. Additionally, an oedometric curve at 250°C is included, even though the AE are not available due to the limitations of the sensor.

Compression curves show variations in the void ratio for the yield point followed by similar slopes, irrespective of the temperature of testing or the initial void ratio. Thus, Table 1 summarises the compression index (c_c) and the swelling index (c_s) obtained for all the oedometric tests carried out. The average compression index reached c_c=0.294 with a coefficient of variation as low as 0.1. These results compare reasonably well with those avail-

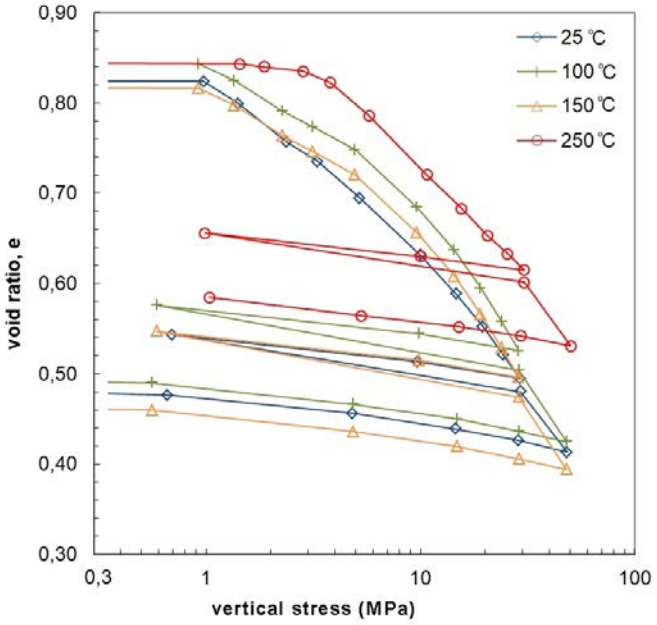

Figure 6. Representative oedometric curves for temperatures from 25 to 250°C.

Table 1. Compression indexes and swelling indexes for all the tests carried out.

	TEST	T (°C)	LOAD	UNLOAD
			c_c	c_s
LOW-MEDIUM TEMPERATURE	EDO-1	25	0.310	0.038
	EDO-2		0.279	0.035
	EDO-5		0.273	0.033
	EDO-6		0.288	0.033
	EDO-7		0.286	0.030
	EDO-8		0.291	0.038
	EDO-9		0.299	0.039
	EDO-10		0.309	0.038
	EDO-11	50	0.332	0.038
	EDO-12	60	0.257	0.030

	TEST	T (°C)	LOAD	UNLOAD
			c_c	c_s
HIGH TEMPERATURE	EDO-13	100	0.306	0.032
	EDO-14		0.332	0.038
	EDO-15		0.329	0.038
	EDO-16		0.332	0.038
	EDO-17	150	0.229	0.036
	EDO-18		0.287	0.037
	EDO-19		0.332	0.038
	EDO-20	200	0.276	0.037
	EDO-21		0.281	0.037
	EDO-22	250	0.249	0.032

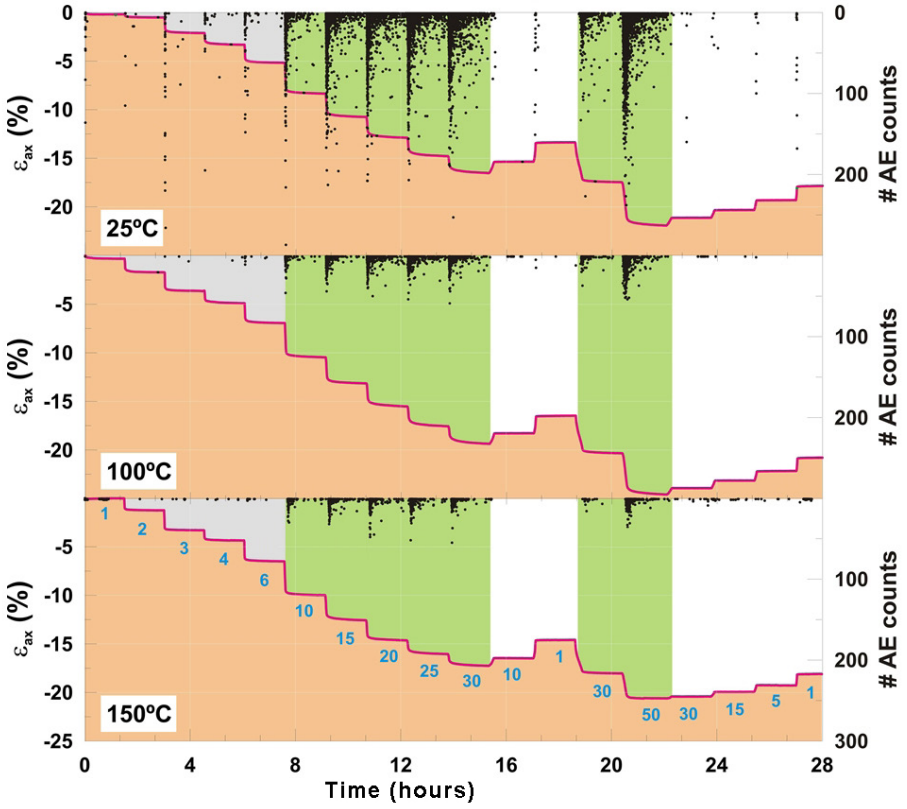

Figure 7. Acoustic emission data.

able in the literature [15, 27, 36 and 37]. In addition, the average swelling index c_s=0.036 is characteristic of the whole range of unloading to within 0.08.

Despite the similar results in the compaction and unloading results, the AE counts measured during the tests show a significant variation (Fig. 7). AEs at higher temperatures 1) are most frequent at the start of each loading ramp, 2) decay in frequency exponentially with time at each loading step, 3) are rare during unloading, and 4) exhibit lower counts at higher temperatures.

Such observations, together with the results of the grain size distributions before and after the tests (see Fig. 8), leave little doubt that the AEs correspond to the crushing events during the tests.

The tests carried out at room temperature underwent substantial grain failure: as shown in Fig. 8, the fines content increased from 18 even up to 55% and D_{50} (the grain size of the sand particles at 50% in the cumulative distribution) reduced in some cases by more than 50%. In contrast, the samples tested at higher temperatures revealed minor grain failure.

Finally, AEs prove to be useful for narrowing down the yield point. In this case, as the AE activity intensifies at

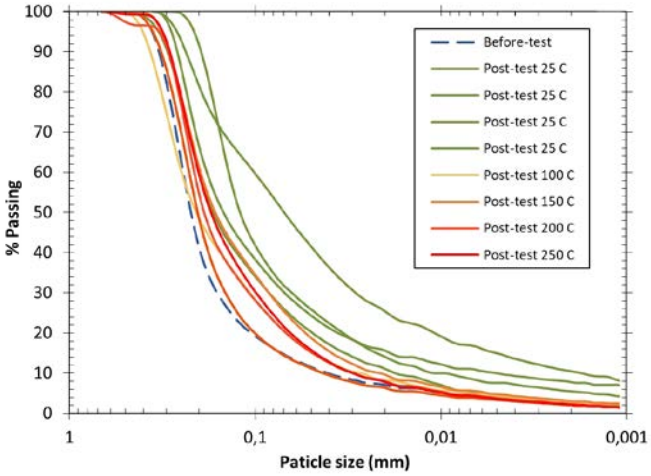

Figure 8. Grain size distribution curves before and after testing.

the range of 10 MPa, it appears reasonable to establish the yield point in that load step. Hence, according to Equation 7, a coordination number of 7.6 ± 0.5 at the yield point can be accepted. That range matches the expected value for dense sands 7.7 (C_n≅≈7.7 for the maximum dry density considered ≅ 1700 kg/cm^3 and equivalent to a porosity ≅ 36%).

6 DISCUSSION

If the test temperature is raised, the macroscopic sand compressibility beyond the yield point remains unaffected, the AE activity decays, and changes in the particle size distribution are negligible. Therefore, it seems that phenomena other than grain-scale mechanical crushing alone must account for the compressibility at high temperatures.

On the one hand, with an increase of the temperature, the elastic parameters decrease [38] and so does the stress level at the tip of a crack or flaw (K_I). On the other hand, the fracture toughness, K_{IC}, increases [39 and 40]. Both circumstances make Equation 6 unlikely to hold and appears to be sufficient to explain the sharp decay of the AEs and the null change of the grain size distribution.

However, an SEM analysis (photomicrographs) of the sand grains, after being subjected to a stress of 14 MPa (according to the yield point) and at 150°C, proves the presence of incipient fractures, see Fig.9.

Furthermore, a detailed observation with an optical microscope reveals that the quartz grains contain fluid inclusions, not only in the syntaxial cement growth but in the detrital grains as well, Fig.10. These fluid inclusions are, in some cases, strongly aligned.

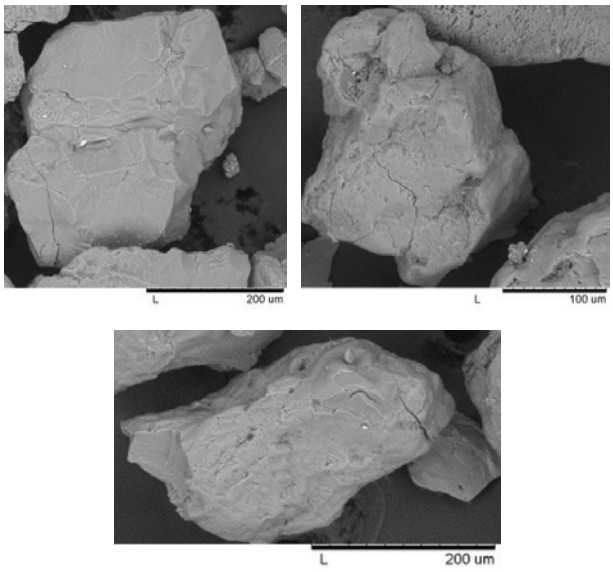

Figure 9. Incipient cracks on quartz grains tested at 150°C.

Thus, fluid inclusions, that are themselves flaws in the grain, seem to contribute to weakening its most overstressed region by the chemical rupture of the Si-O bonds. This process may counterbalance the decrease in the stress level due to the temperature rise in Equation 6. Such a phenomenon, known as stress-corrosion, is considered as the main mechanism of subcritical crack growth.

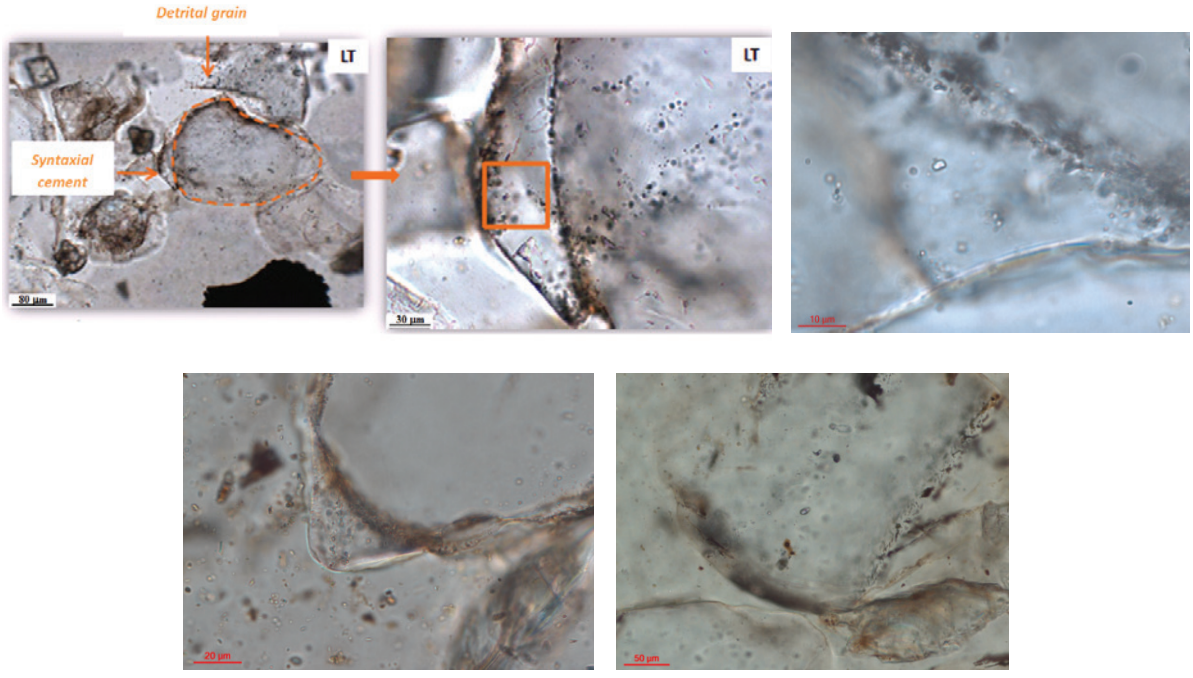

Figure 10. Fluid inclusions in quartz grains.

As a consequence, the subcritical crack growth rate, at high temperatures, does not release enough energy to generate sound waves (acoustic emissions), and some counts drop off as a result. Conversely, at room temperature, as the grain failure occurs once the effective critical stress for crushing is reached, the growth rate is faster, and the fast release of energy generates sound waves recorded as acoustic emissions.

7 CONCLUSIONS

Grain crushing is the fundamental source of the compressibility of sands subjected to high stresses at room temperature, although hardly any studies have been devoted to the effect of temperature. The presented oedometric tests revealed that the compressibility of quartz sand beyond the yield point is not affected either by the temperature or the initial void ratio; thus, all the oedometric curves follow a reasonably similar compression pattern (c_c=0.294 on average, with a coefficient of variation of 0.1).

Although the AE counts drop off and changes in the particle size distribution are negligible when the temperature is raised, the quartz grains subjected to high temperatures and stresses (150°C and 14 MPa) show incipient fractures.

A detailed study by optical microscope reveals fluid inclusions in the detrital grains, which suggests that subcritical crack growth may well be considered the cracking process of the grains at high temperature through stress-corrosion.

Finally, the fact that the compressibility remains unaffected by the temperature can be attributed to a change in the grain-scale mechanics: from critical rapid crack growth, at low temperatures, to fluid-sensitive subcritical cracking, at the higher temperatures, which is in good agreement with related works [41].

Acknowledgments

The authors would like to thank Repsol Technological Centre for granting permission to publish some of the results obtained in the tests shown in this paper.

REFERENCES

[1] Lo, K.Y., Roy, M. 1973. Response of particulate materials at high pressures. Soils and Foundations 13(1), 61-76.

[2] Vesic, A.S., Clough, G.W. 1968. Behaviour of Granular Materials under High Stresses. Journal of Soil Mechanics and Foundations Division ASCE 94(3), 661-688.

[3] Lee, K.L., Farhoomand, I. 1967. Compressibility and crushing of granular soil in anisotropic triaxial compression. Canadian Geotechnical Journal 4(1), 68-86. doi:10.1139/t67-012

[4] Bishop, A.W., Webb, D.L., Skinner, A.E. 1965. Triaxial test on soils at elevated cell pressure. In Proceedings of the 6th International Conference on Soil Mechanics and Foundation Engineering, Montreal, Canada, 1, pp 170-174.

[5] Coop, M.R., Lee, I.K. 1993. The behaviour of granular soils at elevated stresses. In Predictive Soil Mechanics. Proceedings of the Wroth Memorial Symposium, Thomas Telford, London, UK, pp. 186-196.

[6] Hardin, B.O. 1985. Crushing of soil particles. Journal of Geotechnical Engineering 11, 1177-1192.

[7] Hagerty, M.M., Hite, D.R., Ullrich, C.R., Hagerty, D.J. 1993. One-dimensional high-pressure compression of granular media. Journal of Geotechnical Engineering ASCE 119(1), 1-18.

[8] Yamamuro, J.A., Bopp, P.A., Lade, P.V. 1996. One-dimensional compression of sand at high pressures. Journal of Geotechnical Engineering ASCE 122(2), 147-154.

[9] Lade, P.V., Yamamuro, J.A., Bopp, P.A. 1996. Significance of particle crushing in granular materials. Journal of Geotechnical Engineering ASCE 122(4), 309-316.

[10] McDowell, G.R., Bolton, M.D. 1998. On the micromechanics of crushable aggregates. Géotechnique 48(5), 667-679. doi:10.1680/geot.1998.48.5.667

[11] Nakata, Y., Hyodo, M., Hyde, A.F.L., Kato, Y., Murata, H. 2001b. Microscopic particle crushing of sand subjected to high pressure one-dimensional compression. Soils and Foundations 41(1), 69-82.

[12] Borg, I., Friedman, M., Handin, J., Higgs, D.V. 1960. Experimental deformation of St. Peter Sand: a study of cataclastic flow. In Rock Deformation (D. Griggs, J. Handin Eds.), Geological Society of America Memoirs. 79, 133-192.

[13] Zhang, J., Wong, T-F., Davis, D.M. 1990. Micromechanics of pressure-induced grain crushing in porous media. Journal of Geophysical Research 95(B1), 341-352.

[14] Menendez, B., Zhu, W., Wong, T-F. 1996. Micromechanics of brittle faulting and cataclastic flow in Berea Sandstone. Journal of Structural Geology 18(1), 1-16.

[15] Chuan, F.A., Kjeldstad, A., Bjorlykke, K., Hoeg, K.

2003. Experimental compression of loose sand: Relevance to porosity reduction during burial sedimentary basins. Canadian Geotechnical Journal 40(5), 995-1011. doi:10.1139/t03-050

[16] Karner, S.L., Chester, F.M., Kronenberg, A.K., Chester, J.S. 2003. Subcritical compaction and yielding of granular sand. Tectonophysics 377(3-4), 357-381.

[17] Karner, S.L., Chester, J.S., Chester, F.M., Kronenberg, A.K., Hajash, A. 2005. Laboratory deformation of granular quartz sand: Implications for the burial of clastic rocks. American Association of Petroleum Geologists Bulletin 89, 603-625.

[18] Brzesowsky, R.H., Spiers, C.J., Peach, C.J., Hangx, S.J.T. 2014. Time-independent compaction behaviour of quartz sands. Journal of Geophysical Research: Solid Earth 119. doi:10.1002/2013JB010444.

[19] Karner, S.L., Kronenberg, A.K., Chester, F.M., Chester, J.S., Hajash, A. 2008. Hydrothermal deformation of granular quartz sand. Journal of Geophysical Research: Solid Earth 113 (B05404). doi:10.1029/2006JB004710

[20] Chester, J.S., Lenz, S.C., Chester, F.M., Lang, R.A. 2004. Mechanisms of compaction of quartz sand at diagenetic conditions. Earth and Planetary Science Letters 220, 435-451.

[21] Chester, F.M., Chester, J.S., Kronenberg, A.K., Hajash, A. 2007. Subcritical creep compaction of quartz sand at diagenetic conditions: Effect of water and grain size. Journal of Geophysical Research: Solid Earth 112(B06203), 1-15. doi:10.1029/2006JB004317

[22] Schutjens, P.M.T.M. 1991. Experimental compaction of quartz sand at low effective stress and temperature conditions. Journal of the Geological Society 148, 527-539. doi: 10.1144/gsjgs.148.3.0527

[23] Wong, T-F. 1990. Mechanical compaction and the brittle-ductile transition in porous sandstones. Geological Society Special Publication 54, 111-122.

[24] Wong, T-F., Baud, P. 1999. Mechanical compaction of porous sandstone. Oil & Gas Science and Technology 54(6), 715-727. doi:10.2516/ogst:1999061

[25] Heard, J.C., Carter, N.L. 1968. Experimentally induced natural intergranular flow in quartz and quartzite. American Journal of Science 266, 1-42.

[26] Golightly, C.G. 1990. Engineering properties of carbonate sands. PhD dissertation, Bradford University.

[27] Nakata, Y., Kato, Y., Hyodo, M., Hyde, A.F.L., Murata, H. 2001a. One-dimensional compression behaviour of uniformly graded sand related to single particle crushing strength. Soils and Foundations 41(2), 39-51.

[28] Leleu, S., Valdes, J.R. 2006. Crushing of sand mixtures. Geomechanics and Geotechnics of Particulate Media. Hyodo, Murata and Nakata (eds).

[29] Drescher, A., De Josselin de Jong, G. 1972. Photoelastic verification for a model of the flow of granular material. Journal of the Mechanics and Physics of Solids 20, 337-351.

[30] Gallagher, Jr. J.J. 1976. Fracturing of Quartz Sand Grains. American Rock Mechanics Association, The 17th U.S. Symposium on Rock Mechanics (USRMS), 25-27.

[31] Santamarina, J.C., Klein, K.A., Fam, M.A. 2001. Soils and Waves: Particulate Materials Behavior, Characterization and Process Monitoring. Wiley.

[32] Mavko, G., Mukerji, T., Dvorkin, J. 2009. The Rock Physics Handbook. Tools for Seismic Analysis of Porous Media. Cambridge University Press, New York, United States of America.

[33] Huber, M.T. 1904. Zur Theorie der Berührung fester elastischer Körper. Annalen der Physic. 319 (6), 153-163. https://doi.org/10.1002/andp.19043190611

[34] Frank, F.C., Lawn, B.R. 1967. On the theory of Hertzian fracture. Proceedings of the Royal Society of London. Series A, Mathematical and Physical Sciences, 299(1458), pp. 291-306. doi: 10.1098/rspa.1967.0137

[35] Field, W.G. 1963. Toward the statistical definition of a granular mass. In: Proceeding of 4th Australia-New Zealand Conference on soil mechanics and foundation engineering: 143-148.

[36] McDowell, G.R., Humphreys, A. 2002. Yielding of granular materials. Granular Matter, 4(1), 1-8.

[37] Mesri, G., Vardhanahuti, B. 2009. Compression granular materials. Canadian Geotechnical Journal 46(4), 369-392. doi:10.1139/T08-123

[38] Pabst, W.E.G. 2013. Elastic properties of silica polymorphs-A review. Ceramics-Silikáty 57(3), 167-184.

[39] Atkinson, B.K., Avdis, V. 1980. Technical Note. Fracture mechanics parameters of some rock-forming minerals determined using an indentation technique. International Journal of Rock Mechanics and Mining Sciences & Geomechanics Abstracts 17, 283-386.

[40] Atkinson, B.K. 1984. Subcritical crack growth in geological materials. Journal of Geophysical Research 89(B6), 4077-4114.

[41] Lenz, S.C. 2002. Acoustic emission and compaction creep of quartz sand at subcritical stress. MS Thesis. Texas A&M University (Unpublished).

DETERMINATION AND PREDICTION OF THE ULTIMATE BEARING CAPACITY OF A STRIP FOOTING ON UNDRAINED CLAYEY SLOPES

DOLOČANJE IN NAPOVED MEJNE NOSILNOSTI PASOVNIH TEMELJEV NA NEDRENIRANIH GLINENIH POBOČJIH

Rajesh Prasad Shukla
Adani Institute of Infrastructure Engineering,
Department of Civil and Infrastructure Engineering
Ahmedabad, India
E-mail: rpshukla.2013@iitkalumni.org

Ravi S. Jakka
Indian Institute of Technology Roorkee,
Department of Earthquake Engineering
Roorkee, India
E-mail: rsjakka@iitr.ac.in

DOI https://doi.org/10.18690/actageotechslov.16.2.50-65.2019

Keywords

bearing capacity ratio, cohesive soil, cohesionless soil, edge distance, footing, slope

Ključne besede

razmerje nosilnosti, vezljiva zemljina, nevezljiva zemljina, razdalja med robovi, temelj, naklon

Abstract

In the present study, a footing resting on clayey slopes is analysed using finite element analysis, and the results are further used for predicting the bearing capacity of the footing using statistical analyses. The absolute bearing capacity increases with an increase in the embedment depth of the footing, the edge distance and the soil undrained strength. However, the rate of increase of the bearing capacity with the footing depth on the slope is, relatively, less than the level ground. The critical edge distance is found to increase with an increase in the embedment depth of the footing and the slope inclination. In contrast to cohesionless soil slopes, the critical edge distance decreases and the bearing-capacity ratio increases with an increase in the soil strength for a given slope geometry and footing depth. The magnitude of the critical edge distance is found to vary from 0.5 to 5 times the footing width in cohesive soil, which is relatively very small when compared to cohesionless soil. A number of differences have been observed between the failure mechanism of a footing resting on a cohesive soil slope and a cohesionless soil slope, which contributes to the differences in their behaviour. The soil strength and the slope inclination are found to be the two most important factors affecting the bearing capacity of a footing on slopes. The predicted values of the bearing capacity are compared with the existing experimental and theoretical values.

Izvleček

V tej študiji je s pomočjo metode končnih elementov analiziran temelj na glinastih pobočjih. Rezultati analiz so nato s pomočjo statističnih analiz uporabljeni za napovedovanje nosilnosti temeljev na pobočju. Absolutna nosilnost narašča s povečanjem globine vpetja, razdalje do roba pobočja in nedrenirane trdnosti zemljine. Stopnja povečanja nosilnosti z globino vpetja na pobočju je relativno manjša kot pri temeljih na ravnih tleh. Ugotovljeno je, da se kritična razdalja do roba temelja poveča s povečanjem globine vpetja temelja in naklona pobočja. Za določeno geometrijo pobočja in globino osnove temelja, se, v nasprotju s pobočji nekoherentnih zemljin, kritična razdalja do roba zmanjšuje in razmerje nosilnosti narašča s povečanjem trdnosti tal. Ugotovljeno je tudi, da se obseg kritične razdalje do roba giblje od 0,5 do 5-kratne širine temelja v vezljivi zemlji, kar je v primerjavi z nevezljivo zemljino relativno majhno. Ugotovljene so bile številne razlike med porušnim mehanizmom temelja na piobočju iz vezljivih in nevezljivih zemljin, ki prispevajo k razlikam v obnašanju tal. Nadalje je ugotovljeno, da sta trdnost tal in naklon pobočja najpomembnejša dejavnika, ki vplivata na nosilnost temelja na pobočju. Napovedane vrednosti nosilnosti so bile primerjane z obstoječimi eksperimentalnimi in teoretičnimi vrednostmi.

1 INTRODUCTION

A foundation located on a slope or adjacent to a slope crest possesses a lower bearing capacity than level ground as it lacks the confinement from the slope side. Footings resting precisely on the slope crest possess the minimum bearing capacity [1]. However, the bearing capacity improves with an increase in the edge distance (b) between the footing and the slope crest, an increase in the soil strength and also with an increase of the embedment depth of the footing [1].

The majority of earlier studies were carried out on cohesionless soil. The range of critical edge distances is found to vary from 2 to 12 times the footing width (B) in cohesionless soils [2-3]. A number of studies investigated the footing resting adjacent to cohesive slopes. Meyerhof [1] assumed a uniform mobilization of the soil on the slope side and the level side, and found that the critical edge distance ranged from B to 4.5B. Kusakabe et al. [4] found that $c_u/(\gamma B)$ is an important factor affecting the bearing capacity and the failure mechanism. In a few cases the critical edge distance was found to be more than 5B. DeSimone [5] used a boundary integral equation to study the bearing capacity of the footing on a clay slope without considering the effect of the edge distance in the analysis. Jao et al. [6] found that the effect of the slope inclination and the edge distance is relatively less in purely cohesive soils than in silty clay and cohesionless soil. Georgiadis [7] analyzed the cohesive soil slope using an upper-bound analysis and found the critical edge distance to be 2B without a consideration of the slope height. Al-Jubair & Abbas [8] and Abbas and Sabbar [9] used 2D Plaxis and observed that the influence of the slope became insignificant at an edge distance of 1.5B. Georgiadis and Chrysouli [10] varied the edge distance from 0 to B and found that the bearing capacity decreases linearly with the horizontal seismic acceleration. Gill et al. [11-12] found that the efficiency of the reinforcement reduces with an increase in the edge distance. Farzaneh et al. [13] determined the seismic bearing capacity of a footing on a slope for a maximum edge distance of 1B. Mirzababaei et al. [14] also constrained the edge distance to 3B. Luo and Bathurst [15] performed a reliability analysis for the bearing capacity of a footing resting on a cohesive slope crest. Baazouzi et al. [16-17] determined the effect of slope inclination on the undrained bearing capacity. Aminpour et al. [18] determined the effect of surcharge loading slope behaviour. Acharya and Dey [19] found the critical edge distance to be 4B in c-ϕ soils for an isolated footing. Leshchinsky and Xie [20] analysed a number of cases of a footing resting on a c-φ slope, but the edge distance was not determined in the analysis. Acharya and Dey [21] developed an interaction mechanism for a multiple footing resting on a slope based on a displacement pattern. A number of studies have also been carried out to analyse cohesive soil slopes using soft computing [19, 22-24]. However, most of these studies are limited to a determination of the slope's stability. It is observed from the literature that a consensus over the critical edge distance is also missing in the case of a footing resting over a cohesive slope. In the majority of studies the edge distance was found to vary from B to 3B. However, some studies found the values to be on the very high side. Kusakabe et al. [4] and Meyerhof [1] found this distance to be approximately 4B–5B. Zhao and Wei [25] found that the bearing capacity is increasing continuously, even up to an edge distance of 10B. However, these values cannot be considered as a true value of the critical edge distance as most of the studies were limited to a particular soil and a limited range of other parameters. The surcharge loading is triangular on the slope side; however, most of the earlier studies considered it as a uniform loading.

In this study, a series of finite element analyses were performed to determine the effect of various factors, such as the slope geometry, soil strength, edge distance, and embedment depth on the bearing capacity of a footing resting on cohesive soil slopes. The differences in the failure mechanism of a footing resting on clayey soil and cohesionless soil are identified and presented in detail. The use of conventional limit equilibrium methods to determine the bearing capacity is time consuming. Therefore, a limit analysis has been used in the present study. Additionally, a nonlinear multiple regression analysis (NMRA) and an artificial neural network (ANN) have been used to predict the bearing capacity factor as well as the BCR. The predicted values are compared with the earlier theoretical and experimental studies.

2 NUMERICAL MODELLING OF THE PROBLEM

The finite-element program OptumG2 [26] was used to perform the analysis. A typical model used in the analysis is presented in Fig. 1. A horizontal displacement is not allowed along the vertical boundary and no displacement is allowed along the bottom boundary. However, along the slope edge, the displacement is allowed in both the directions. The gradient of the soil slope is kept uniform throughout the slope. Based on the edge distance and the slope geometry, the area of the domain was selected as large enough to avoid the boundary effect. The minimum height and width of the domain are restricted to 8B and 16B, respectively. The width domain is increased to 25B on gentle slopes. A

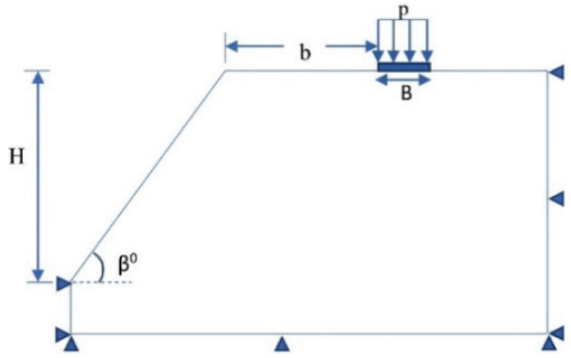

Figure 1. Representation of the foundation and the slope with boundary conditions.

number of iterations were performed to achieve stable results, and in every iteration the mesh was re-refined in the critical area to avoid the unnecessary refining of the mesh all over the domain area.

The strip footing has been modeled as a "plate" element. Under the plain-strain condition, the elastic plate element behaves like a standard Euler-Bernoulli beam element. To model the rigid footing, the stiffness of the plate has to be kept very high, compared to the soil. The clay was modelled using the elastic/perfectly-plastic Mohr-Coulomb model. The unconfined strength of the soil is assumed to be constant throughout the depth of the soil strata.

Three type of elements, namely, three-noded triangular elements for the lower bound analysis, six-node triangular elements for the upper bound, and a 15-node mixed Gauss element were used to model the soil. The lower-bound (UB) analysis follows the formulation of Makrodimopoulos and Martin [27-28], and the upper bound (UB) follows the formulation of Krabbenhøft et al. [29-30] in association with second-order cone programming. The lower-bound element of the three nodes uses a linear change in the stresses between the junction nodes. The lower-bound elements are linked by two zero-thickness elements to produce the statically admissible stress discontinuity between the junction nodes. For the maximum lower bound limit, the collapse load is evaluated by finding a collapse load that satisfies a statically admissible stress field defined by the stress equilibrium equations for triangular elements. Similar to the lower-bound element, the six-nodded upper-bound element uses the linear interpolation of the stresses, while unknown displacements were determined using quadratic interpolation. The displacements are continuous between the elements. The minimum upper-bound limit load satisfies a kinematic velocity field defined by the compatibility and the associated flow-rule equations for triangular elements and velocity discontinuities for soil-skirt interfaces. It is observed that the 15-node mixed Gauss element gives results very close to the average of the UB and LB analyses. Therefore, the analysis was carried out on a 15-node mixed Gauss element.

A total 5000 elements were initially used in the domain and this was increased to 70,000 in the final iteration. The element uses a cubic interpolation and quartic interpolation functions for the stresses and displacements, respectively. The footing is modeled as a perfectly rigid plate, which possesses an infinite stiffness. The six-node zero-thickness element was used to model the interface of the soil and the footing. The interface factor value was varied from 0.5 to 1, to consider the effect of the roughness of the footing. The interface factor is assumed to be 0 for a footing with a perfectly rough base. It was observed that the bearing capacity of a footing resting on a clay slope is changing noticeably with the interface-factor value. However, the change in BCR with the interface friction is very small.

The loading was applied in terms of a load multiplier directly over the footing, and it is increased continuously until the bearing capacity failure Before performing the bearing capacity analysis, a slope-stability analysis was performed to check the stability of the slope. The present study determined the bearing capacity considering the ultimate failure of the footing. Therefore, the settlement criterion has not been considered in the present study due to the inability of a limit analysis. The details of the modeling and the analysis are presented in a manual [26, 31].

3 PARAMETERS CONSIDERED IN THE ANALYSIS

All the parameters that influence the bearing capacity of a footing resting near the slope crest are considered in the analysis. These parameters include, the slope inclination, the edge distance, the average undrained shear strength of the soil and the footing properties. Earlier studies used ranges of undrained shear strength to represent the various consistencies of the cohesive soils [32]. Based on previous studies, a large range of undrained strength values are selected to reflect all the possible ranges of consistency. The ranges of the considered parameters are presented in Table 1. The unit weights of the soil are assumed to be 14–17 kN/m^3. The stiffness of the soil increases with an increase in the consistency of the soil. Therefore, the stiffness of the soil is also assumed to be varying from 2500 kN/m^2 to 14000kN/m^2 with the soil unconfined strength [33]. The edge distance (b) and the embedment depth (D) are normalized with respect to the footing width and stated as the edge-distance ratio (b/B) and the depth ratio (D/B), respectively.

Table 1. Range of various parameters considered in the study.

c_u (kPa)	Consis-tency	$c_u/(\gamma B)$	(b/B)	$\beta°$	(D/B)	No. of analysis
20	Soft	0.7	0, 1, 2, 3, 5	0–15	0, 0.5,1.0	60
40	Medium	1.4	0, 1, 2, 3, 5	0–35	0, 0.5,1.0	120
80	Stiff	2.8	0, 1, 2, 3, 4	0–45	0, 0.5,1.0	150
160	Very stiff	5.7	0, 1, 2, 3, 4	0–55	0, 0.5,1.0	180
320	Hard	10.6	0, 1, 2, 3	0–80	0, 0.5,1.0	204

4 RESULTS AND DISCUSSION

The variation in the bearing capacity with each of the factors is presented in detail and discussed separately. The change in the bearing capacity is determined in terms of the bearing capacity ratio (BCR). The BCR is defined as the ratio of the bearing capacity (or the bearing capacity factor) of a footing resting over the slope to the bearing capacity (or the bearing capacity factor) of the same footing resting over level ground under identical soil conditions. This means that the BCR also represents the relative bearing capacity of a footing resting on a slope to level ground.

4.1 The effect of the slope gradient

The typical variation in the bearing capacity ratio (BCR) with the change in the slope inclination for a footing with various embedment ratios (0, 0.5 and 1) resting on soil ($c_u/(\gamma B)$=2.85) is presented in Fig. 2. The bearing capacity as well as the BCR decreases nonlinearly with the increase in the slope inclination. The adverse effect of the slope on the BCR decreases with an increase in the edge distance. For a larger edge distance, the decrease in the BCR with the slope inclination is either very nominal or negligible. It is also observed that the decrease in the BCR with the slope inclination is relatively large in the footings resting below ground level compared to the footing resting on the ground surface.

The effect of slope inclination on the failure mechanism (shear dissipation contours) for a footing resting at an edge distance of 3B is presented in Fig. 3. It shows that the failure mechanism is independent of the slope inclination for gentle slopes and it is similar to the footing resting on level ground. These cases are similar to the failure mechanism assumed by Terzaghi. However, the interaction between the slope and the footing increases with an increase in the slope inclination,

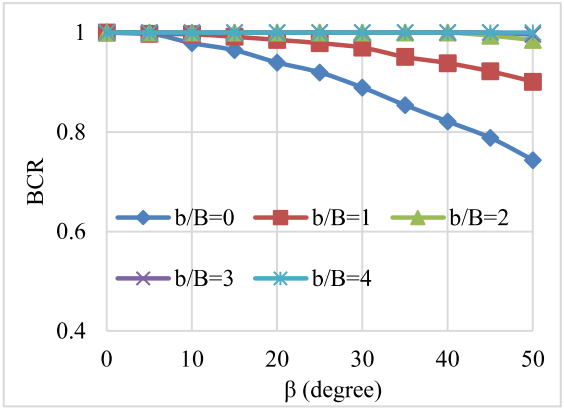

(a)

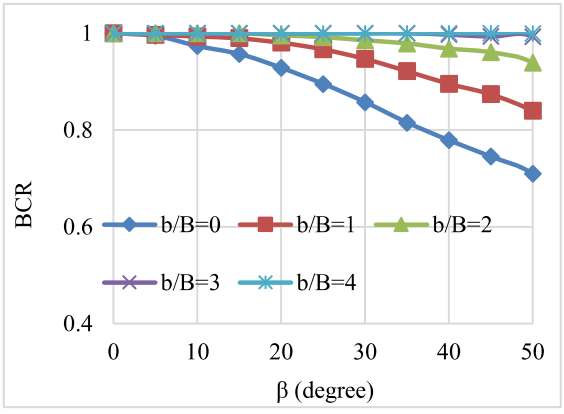

(b)

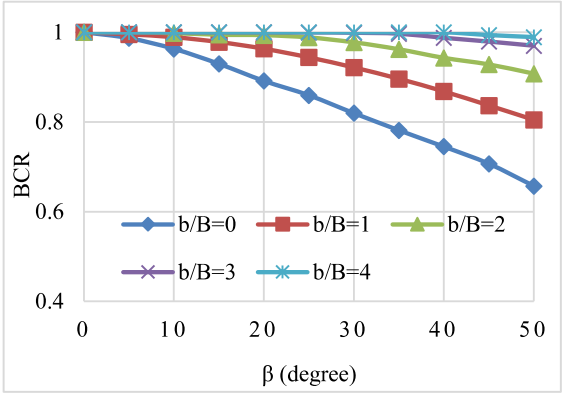

(c)

Figure 2. Effect of slope inclination on the BCR: (a) D/B=0, (b) D/B=0.5, (c) D/B=1.

which decreases the mobilization of the soil strength on the level side of the footing and decreases the bearing capacity of the footing (Fig. 3 c-f). Consequently, there is a decrease in the BCR, as observed in Fig. 2. Cure et al. [34] have also observed similar trends for cohesionless soils. For gentle slopes, the failure is bearing-capacity failure (Fig. 3 a-c). For a very steep slope (50–70°), the slope failure is not representative (Fig. 3 e-f). In moderate-to-steep slopes (35–45°), a combined failure

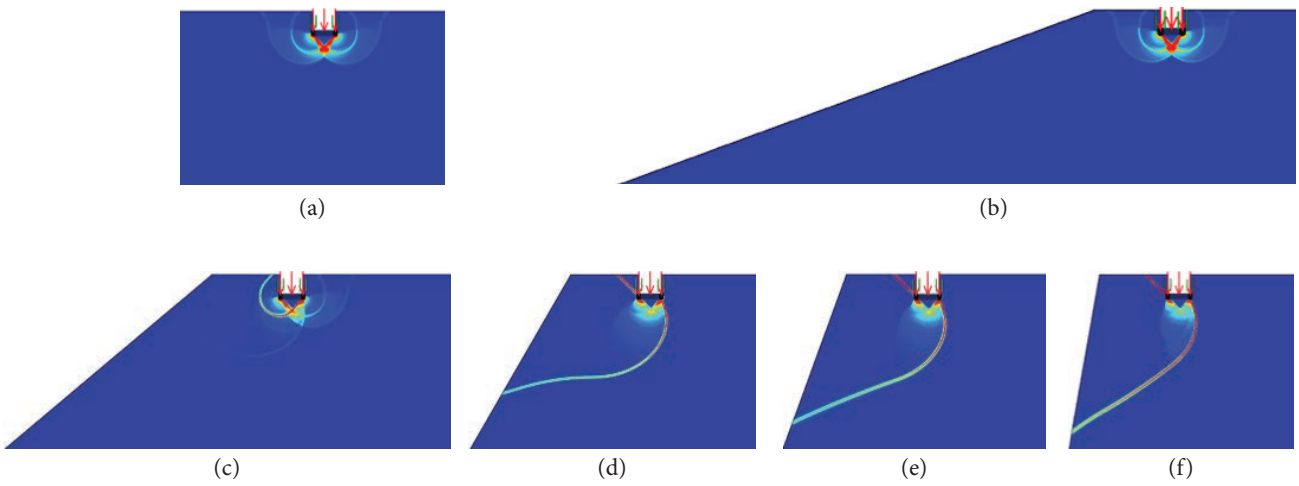

Figure 3. Effect of slope inclination on the failure mechanism: (a) β=0°, (b) β=20°, (c) β=30°, (d) β=40°, (e) β=50°, (f) β=70°.

mechanism coexists, where the slope failure as well as the bearing capacity failure occur together (Fig. 3 d). Even a footing on a steep slope can be stable if it is resting at a large edge distance, as it remains intact and unaffected by the slope. However, soil near to the slope edge and along the slope surface may fail and causes to the local slope failure.

4.2 The effect of the embedment depth of a footing

Fig. 4 shows the effect of the embedment depth of a footing on the BCR for a cohesive soil of $c_u/(\gamma B)$=2.85. Though the bearing capacity increases with an increase in the embedment depth of the footing, the BCR decreases with an increase in the depth of the footing.

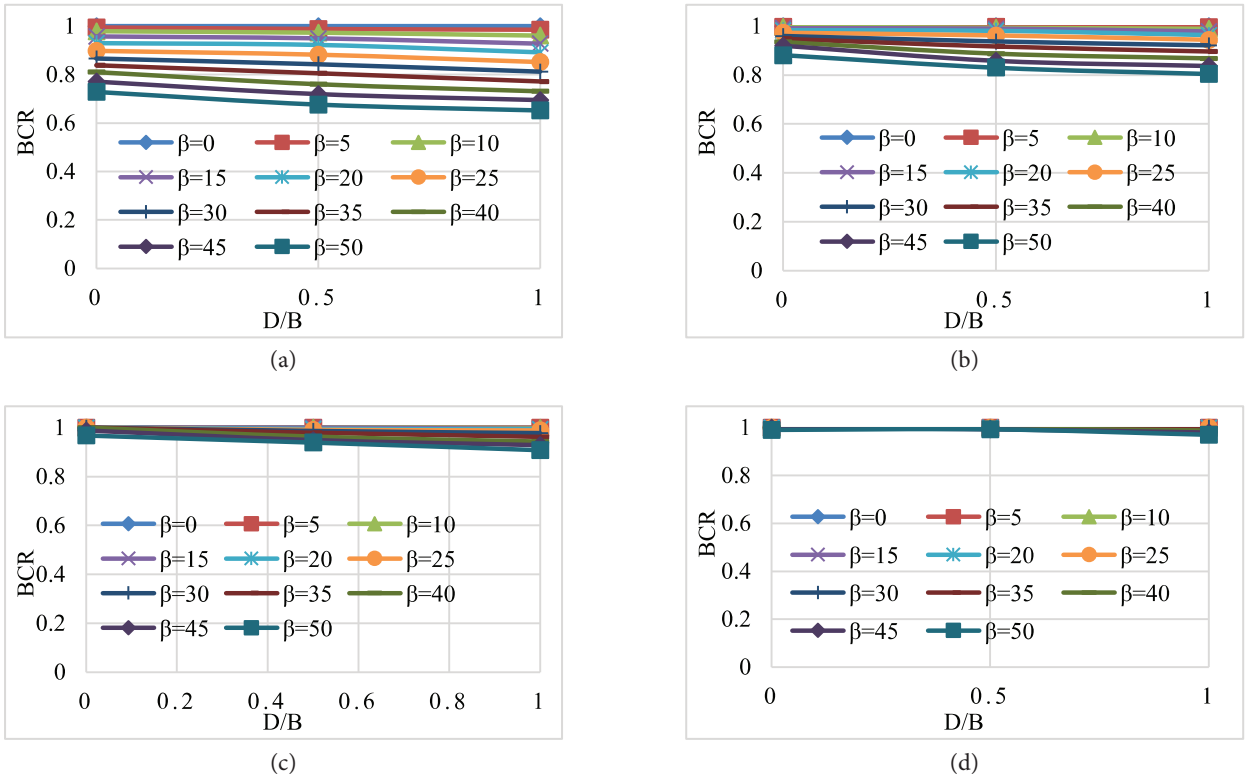

Figure 4. Effect of embedment depth of the footing on the BCR: (a) b/B=0, (b) b/B=1, (c) b/B=2, (d) b/B=3.

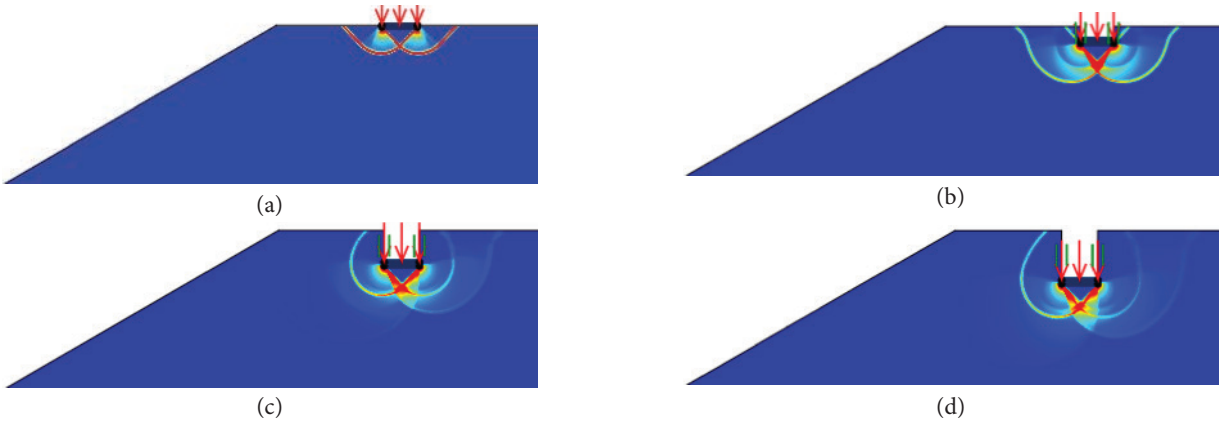

Figure 5. Effect of the embedment depth of a footing on the shear dissipation (a) D/B=0.0, (b) D/B=0.5, (c) D/B=1.0, D/B=1.5.

The influence of the footing depth becomes more noticeable with an increase in the steepness of the slopes, but reduces with an increase in the edge distance. The rate of decrease in the BCR with the depth of the embedment is relatively high when the depth ratio increases from 0 to 0.5, but it reduces when the depth ratio increases from 0.5 to 1. It is expected that the rate of decrease in the BCR with the depth of the footing will decrease further with an increase in the depth of the footing from 1 to 1.5. The contribution of the surcharge loading to the bearing capacity is a maximum for level ground and it reduces with an increase in the slope inclination. Narita and Yamaguchi [35] also found that the effect of the embedment depth of the footing is significant for steep slopes and a low setback distance.

The effect of the embedment depth on the failure mechanism is presented in Fig. 5. At a shallow depth (D/B=0 and 0.5), the failure mechanism of the footing resting on a slope is similar to Terzaghi's failure mechanism (Fig. 4 a, b). However, with an increase in the footing depth, the difference in the failure mechanism becomes significant. The footing resting on the ground surface possesses a small load-carrying capacity and a very small area of foundation soil involves and contributes to the bearing capacity (Fig. 5 a). Therefore, the bearing capacity is independent of the slope (Fig. 5 a). While in the case of a greater embedment depth, the large soil area contributes to the bearing capacity. The failure surface also extends in the lateral direction and a large edge distance is required to cover that much area to mobilize the soil strength optimally (Fig. 5 b, c). Therefore, the BCR reduces with an increase in the embedment depth of the footing, as depicted in Fig. 4.

The influence of the embedment depth on the BCR becomes less evident with an increase in the edge distance. This is due to the fact that for an edge distance, more than or equal to the critical edge distance, the BCR remains almost constant, irrespective of the slope inclination and the depth ratio of the footing. Narita and Yamaguchi [34] have made similar observations for cohesionless soils.

4.3 Effect of the soil strength

The typical variation in the normalized bearing capacity (BCR) with soil strength for a footing with an embedment ratio (D/B) of 1 is presented in Fig. 6. It shows that the BCR increases with an increase in the $c_u/(\gamma B)$. The change in BCR is significant when $c_u/(\gamma B)$ increases from 1.4 to 2.8, but a further increase in $c_u/(\gamma B)$ only makes a negligible improvement in the BCR. Similar observations have been made for the other embedment ratios (D/B=0, 0.5 and 1.5). However, it was observed that the effect of the soil strength on the BCR is increasing marginally with the footing depth. It can also be observed that the effect of the soil strength is more prominent in a steep slope, but it reduces with a decrease in the steepness of the slope. The effect of the soil strength on the BCR reduces with a further increase in the edge distance. With an increase in the edge distance, the footing becomes independent of the slope and the condition becomes similar to level ground. Therefore, the influence of the strength becomes negligible with a decrease in the slope inclination, and it increases the BCR close to 1, irrespective of the slope inclination.

The typical effect of soil strength on the failure mechanism for a footing with an embedment ratio of 1 resting over a soil slope of 300 at an edge distance of 2B is presented in Fig. 7. At low strength ($c_u/(\gamma B)$=0.7), the failure is a global slope failure. However, with an increase in the strength of the soil, the failure mode changes to bearing-capacity failure. The contribution of the soil located on the level side of the footing to the bearing capacity increases with an increase in the soil strength, and the failure becomes a bearing capacity

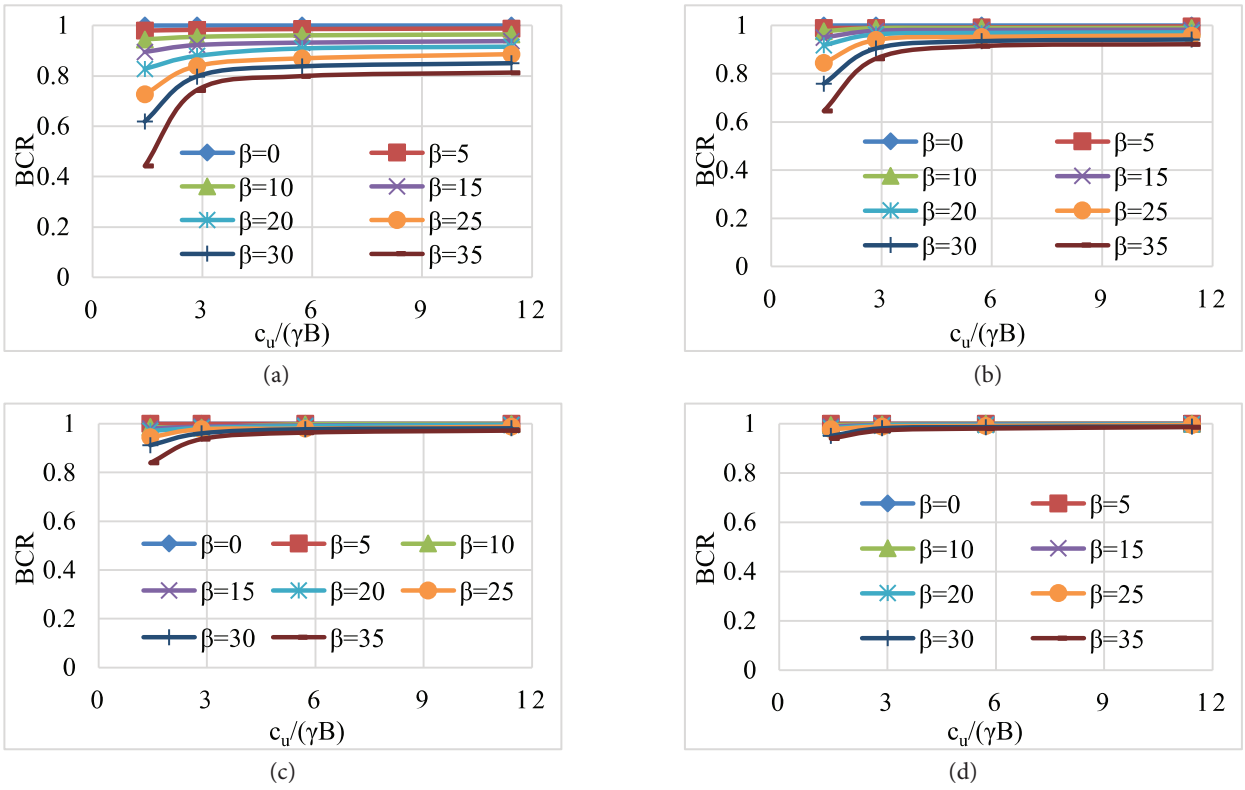

Figure 6. Effect of soil strength on the relative bearing capacity: (a) b/B=0, (b) b/B=1, (c) b/B=2, (c) b/B=3, (c) b/B=4.

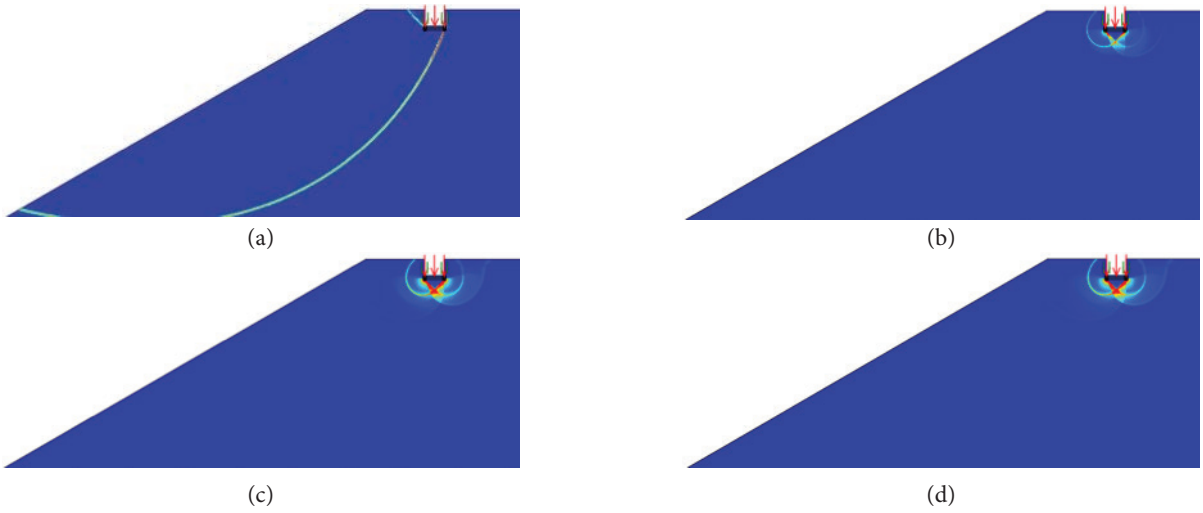

Figure 7. Effect of soil strength on the failure mechanism: (a) $c_u/(\gamma B)$ =0.7, (b) $c_u/(\gamma B)$ =1.4, (c) $c_u/(\gamma B)$ =2.8, (d) $c_u/(\gamma B)$ =5.7.

failure. It can also be stated that the severe effect of the slope decreases with an increase in the strength of the soil. Therefore, the edge distance at which the strength of the soil mobilizes optimally decreases with the increase in the soil strength. Although the magnitude of the safe slope inclination increases with the soil strength, the critical edge distance is found to decrease.

4.4 Effect of the edge distance

The typical variation in the BCR with edge distance is presented in Fig. 8 for a footing of different embedment ratios resting over a soil having $c_u/(\gamma B)$=2.85. The degree of strength mobilization of the soil located on the level side increases with an increase in the edge distance.

Consequently, it increases the bearing capacity and the stability of the footing. The footing located near to the slope fails due to the local shear failure and the mode of failure changed to general shear or punching shear failures with an increase in the edge distance.

At a particular edge distance, both sides of the soil contribute with an equal amount and the footing behaviour becomes independent of the slope. At this critical edge distance, the failure pattern becomes symmetrical about the footing axis. At a small edge distance and a steep slope, the failure is one sided (slope side only), and the soil on the side of the level ground does not fully contribute to the bearing capacity. Therefore, the measured BCR is small for a footing resting precisely on a slope crest or near to the slope crest. The degree of strength mobilization of the soil located on the level side increases with an increase in the edge distance (Fig. 9). The passive resistane increases with an increase in the edge distance, resulting in the increases in the bearing capacity [36]. Varzaghani and Ghanbari [37] also stated that the stiffness of the foundation increases with the setback distance increases, which leads to an increase in the bearing capacity of the soil.

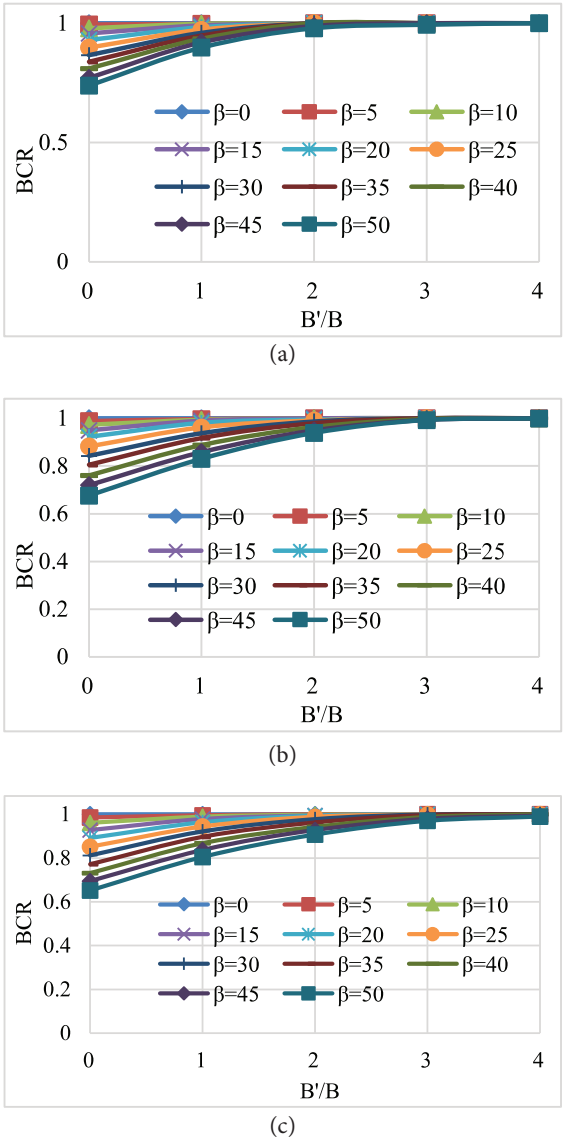

Figure 8. Effect of edge distance on the bearing capacity enhancement for a footing: (a) $D_f/B=0$, (b) $D_f/B=0.5$, (c) $D_f/B=1.0$.

The typical effect of edge distance on the failure mechanism is shown in Figure 9. It shows that the failure mechanism changes significantly with an increase in the edge distance. The elastic wedge below the footing is unsymmetrical for a small setback and becomes a symmetrical and higher edge distance. Also, the shear dissipation on the level side of the footing also increases with an increase in the edge distance. The footing becomes independent of the slope with an increase in the edge distance, and at a particular edge distance, the footing becomes independent of the slope inclination.

On the basis of the numerical analyses, the limiting edge distance is identified for the various combinations

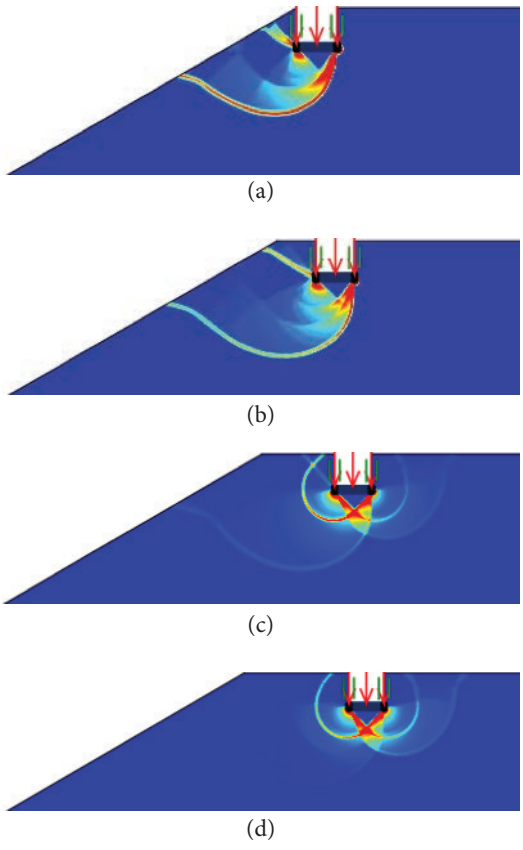

Figure 9. Effect of edge distance on the failure mechanism: (a) b/B=0, (b) b/B=1, (c) b/B=2, (d) b/B=3.

of parameters. The limiting edge distance evaluated in the present study is presented in Table 2. The increase in the critical edge distance is primarily observed (Table 2) due to the increased slope inclination in the soils, rather than an increase in the soil strength as even a steep slope is stable in cohesive soils due to the higher strength.

Table 2. Limiting edge distance for strip footing on a cohesive soil slope.

Undrained shear c_u (kPa)	$c_u/(\gamma B)$	β°	Depth ratio (D/B)	Critical b/B	Optimum b/B
20	*0.7*	0–20	0–1.0	1–5.0	1.0–2.5
40	1.4	0–35	0–1.0	1.0–4.5	1.0–2.0
80	2.8	0–50	0–1.0	1.0–4.5	1.0–1.5
160	5.7	0–55	0–1.0	0.5.0–4.0	0.5–1.0
320	11.4	0–80	0–1.0	0.5.0–3.0	0.5

The International Residential Code [38] and the Uniform Building Code [39] suggest the maximum edge distance can be a minimum of H/3 and 12 m. The Indian standard IS: 1904-1986 recommends maintaining a minimum distance of 0.9 m from the slope surface. However, the code does not provide any guidelines to locate a footing resting near to the slope crest (edge distance). In the present study, the critical edge distance is found to vary from 1 m to 9 m (or 0.05H to 0.45H). However, from the present numerical study, it is observed that the critical setback distance depends not only on the slope height, but also on the slope inclination, the depth of footing, the width of footing, and the strength of the soil ($c_u/(\gamma B)$).

However, in practice, it is not always possible to locate a footing at a critical setback distance. Therefore, an optimum value of the edge distance needs to be identified, at which the reduced bearing capacity (due to the slope effect) is reasonably negligible. In the present study, the optimum value of the edge is determined by considering a BCR value equal to 0.75–0.8 and varies from 0.5B to 2.5B (0.05H to 0.05H), depending on the footing depth, the soil strength and the slope inclination. The obtained values of the optimum setback (0.05H to 0.05H) are significantly less than the values suggested in the codes. The significant difference highlights the fact that a constant value of the edge distance, as suggested in the standards/codes, irrespective of the soil properties, foundation characteristics and slope geometry is not appropriate, and needs to be improved.

5 COMPARISON WITH THE BEHAVIOUR OF A FOOTING RESTING ON COHESIONLESS SOIL SLOPES

The results of the present study have been compared with the results of Shukla and Jakka [2], where footings resting on cohesionless soil slopes were studied in detail. From the comparison of the results, it is observed that the BCR decreases with an increase in the slope inclination and the embedment depth in both cohesive and cohesionless soil slopes. However, the influence of the soil strength on the critical edge and the BCR is the opposite in cohesive and cohesionless soils. Unlike cohesionless soils, the critical edge distance decreases with an increase in the strength of the cohesive soils. Furthermore, the range of the critical edge distance is found to be narrow (1B to 5B) in cohesive soils, compared to cohesionless soil, where it is varying from 2B to more than 12B. Despite the increase in the bearing capacity with the soil strength in cohesive soil, as well as cohesionless soils, the BCR increases with the soil strength in cohesive soil and decreases in cohesionless soil.

The effect of the strength parameters (φ, $c_u/(\gamma B)$) on the BCR and the bearing capacity factor for a footing resting at an edge distance of 1B is presented in Fig. 10. Further discussions are made here to understand the reasons for the observed opposite trends in the case of the critical edge distance and the BCR. The bearing capacity factor ($N_{\gamma q}$) in cohesionless soil increases exponentially with the soil strength in cohesionless soils, especially for level ground (Fig. 10 a), while its increase rate is moderate or low for steep slopes. As the BCR represents the normalized bearing capacity with respect to level ground, the BCR decreases with an increase in the soil strength due to a large and sharp increase in the bearing capacity in level ground compared to the slopes (Fig. 10 a). However, in clayey slopes, the bearing capacity factor (N_{cq}) increases sharply for steep slopes in comparison to gentle slopes (Fig. 10 b). This opposite observation in cohesionless soil and cohesive soil leads to a difference in the observations made in the BCR (Fig. 10 c-d).

To further understand the contradictory observations, the failure mechanisms of footings in both types of soil have been studied. The variation in the failure mechanism for cohesive soil and cohesionless soil is presented in Figs. 7 and 11, respectively. The area contributing to the bearing capacity increases with the increase in the internal friction of cohesionless soil and the undrained strength of cohesive soil. The increase in the area within the rupture surface leads to an increase in the bearing-capacity factor. The contribution from the level side of

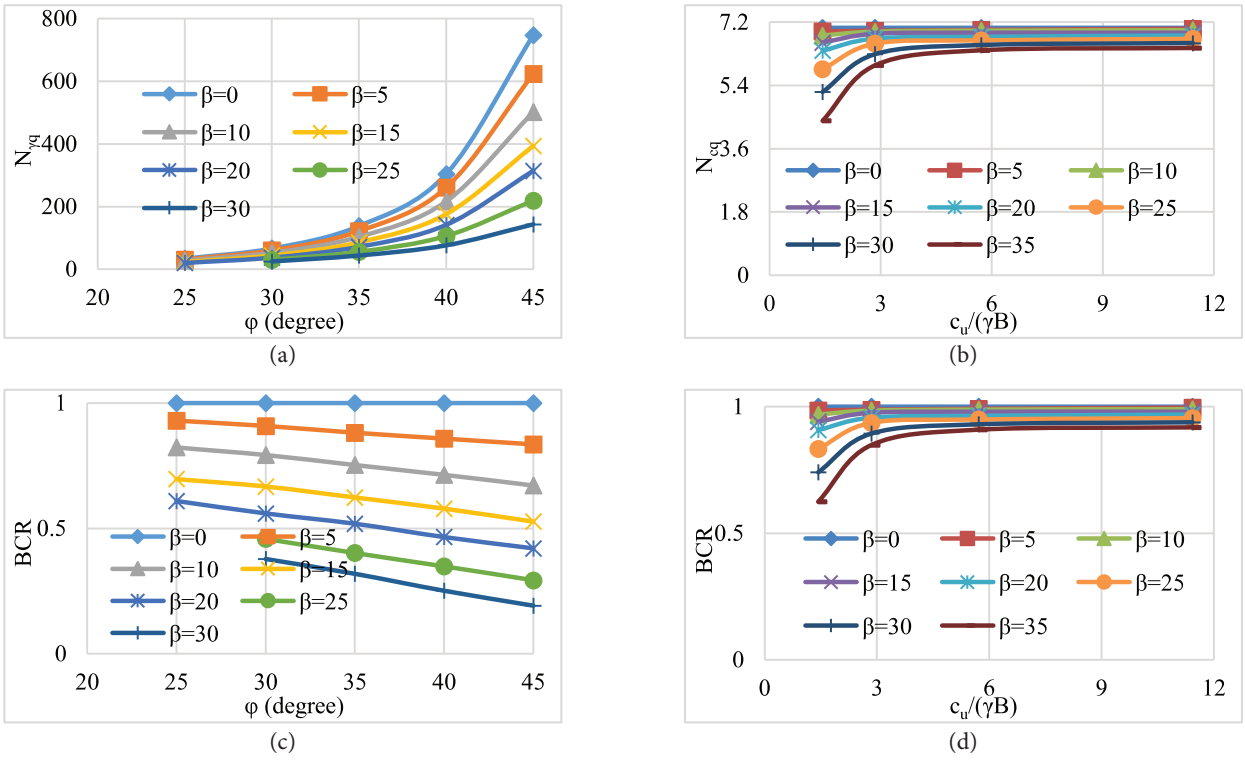

Figure 10. Effect of strength parameters: (a) on the bearing capacity factor in cohesionless soil, (b) on the bearing capacity factor in cohesive soil, (c) on the bearing capacity ratio in cohesionless soil, (d) on the bearing capacity ratio in cohesive soil.

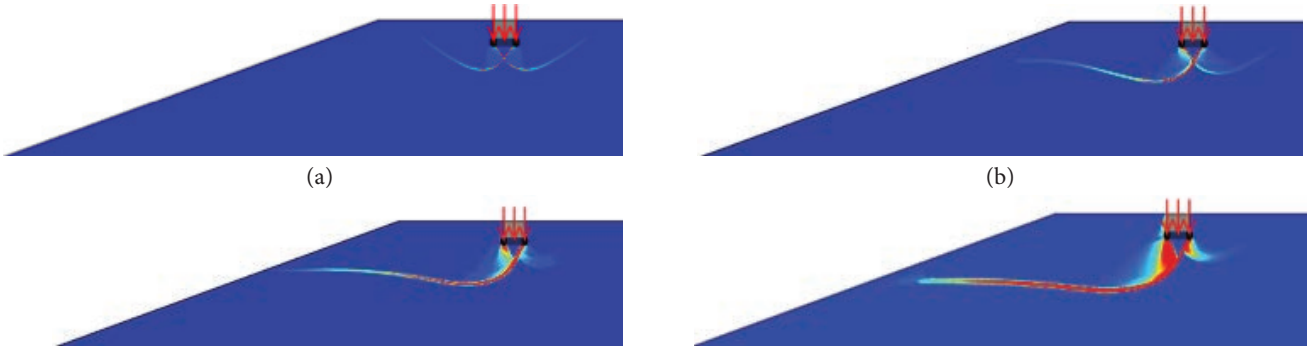

Figure 11. Effect of the angle of internal friction on the failure mechanism: (a) φ=25°, (b) φ=30°, (c) φ=35°, (d) φ=40°.

the footing reduces sharply in cohesionless soils (Fig. 11 a-d). The reduction in the area of the shear zone on the level side of the footing contributes to a reduction in the BCR with an increase in the angle of the internal friction of the soil. This means that the adverse effect of the slope reduces with an increase in the soil-strength parameter in cohesive soil, unlike in the cohesive soil.

In cohesionless soils, the slip surface is a log spiral and extends to longer lateral dimensions and greater depths than the cohesive soil. This contributing area increases significantly with the angle of the shearing resistance of the soil. Therefore, a larger edge distance is required in cohesionless soils. In cohesive soils, the failure surface is circular and only a small area contributes to the bearing capacity. The slip surface extends to a very small area beyond the footing width in cohesive soils. Also, the failure mechanism changes from slope failure to bearing-capacity failure with an increase in the strength for a given edge distance. Therefore, the critical edge distance decreases with an increase in the soil strength in cohesive soils.

6 PREDICTION OF THE BEARING CAPACITY

The numerical analysis results were used to carry out a regression analysis and an artificial neural network (ANN). The purpose of using both of the methods is to predict the BCR and the bearing-capacity factor accurately. It is observed from the numerical analyses that a total of four independent variables (i.e., b, β, $c_u/(\gamma B)$ and D/B) influences the bearing capacity factor of a footing resting near to the slope crest. The linear multiple regression (LMR) analysis was carried out initially to predict the BCR and N_{cq} . The regression coefficient (R^2) is found to be 0.81 and 0.68 for N_{cq} and BCR, respectively. This means that LMR is not efficient to model and predict the bearing capacity of a footing on a slope as the relationship between the independent variables and the dependent variable is nonlinear. Therefore, it is necessary to consider the nonlinearity in developing regression equations. To consider the nonlinearity, it is assumed that Ncq and BCR are dependent not only on these four variables, but also upon a number of other variables. These other variables are a function of the initially assumed four independent variations. Considering these derivatives, a nonlinear multiple regression analysis (NMRA) and correlation analysis, along with other statistical tests, were performed to derive an equation to predict the bearing-capacity factor (N_{cq}) considering the combined effect of the soil cohesion and the surcharge loading above the footing base. Another equation is also developed to determine the change in the bearing capacity (BCR).

Various types of functions, such as linear, exponential and polynomial functions, were initially assumed, and finally the best relationship was used to develop the equation. Initially, a total of 24 variables, which are functions of four independent variables, were considered in the regression analysis to develop equations to compute BCR and N_{cq}. Co-linearity can produce serious problems and ordinary least-squares approximations can be very different from the true values. Therefore, the degree of multi-collinearity was used to remove the insignificant variables. It was found that only eight variables out of 24 affect the N_{cq}) significantly. Later, these eight variables were used to develop an equation to predict N_{cq}. It was found that R^2 reduces from 0.994 to 0.975, when a number of insignificant variables were removed from the analysis. This reduces the number of variables in the regression equation significantly, without reducing the R^2 value by much. It ensures that all the assumed dependent variables are not affecting the bearing capacity significantly with respect to those assumed in the initial phase of the regression analysis. Similarly, 13 derivatives were used in the development of an equation to predict the normalized bearing relative to the level ground (BCR) out of 32 derivatives. It reduces the regression coefficient from 0.992 to 0.953. The ultimate bearing capacity of a footing located adjacent to a slope can be determined precisely by using either Eqn. 4 or Eqn. 5. Therefore, it is suggested to use the BCR values (using Eqn. 2) and Eqn. 4 to determine the effect of the slope geometry on the footing bearing capacity of a footing on a slope.

In equations (1) to (5) c_u is the undrained cohesion of the soil, N_{cq} is the bearing-capacity factor, β is the slope inclination in radians, D is the depth of the footing, B is the width of the footing, γ is the unit weight of the soil and b is the edge distance.

$$N_{cq} = 5.18 - 2.2\beta + \frac{b}{B}\beta\left(1 - 0.016\frac{b}{B} + 0.27\frac{D}{B}\right) + 3.6\frac{D}{B}\left(1 - 0.48\frac{D}{B} - 0.28\beta\right) + \frac{c_u}{\gamma B}\beta\left(0.4 - 0.03\frac{c_u}{\gamma B}\right)$$
$$-1.85\beta^2\left(1 - 0.18\beta - 0.04\frac{c_u}{\gamma B} - 0.14\frac{D}{B}\right) \quad (1)$$

$$BCR = 1 - 0.4\beta + 0.065\frac{c_u}{\gamma B}\beta\left(1 - 0.068\frac{c_u}{\gamma B}\right) + 0.17\frac{b}{B}\beta\left(1 - 0.15\frac{b}{B}\right) - 0.28\beta^2\left(1 - 0.038\frac{c_u}{\gamma B} - 0.2\beta - 0.12\frac{D}{B}\right)$$
$$-0.072\frac{D}{B}\beta\left(1 - 0.22\frac{b}{B}\right) \quad (2)$$

$$N_{cq} \text{ on slope} = N_{cq} \text{ on level ground (BCR)} \quad (3)$$

$$\text{Ultimate bearing capacity}_{(slope)} = N_{cq(slope)}c_u \quad (4)$$

$$\text{Ultimate bearing capacity}_{(slope)} = (5.16c_u + \gamma D)\text{BCR} \quad (5)$$

Hansen [40] and Vesic [41] have also developed equations considering the slope inclination and $c_u/(\gamma B)$ only. Later, Bowles [42] also developed an equation and the soil strength was considered in the developed equation. Recently, Georgiadis [7] proposed an equation to calculate Nc (slope) based on a rigorous finite element analysis. However, the developed equation is complex and does not consider the effect of the footing depth that is an important factor affecting the bearing capacity. The presented Eqns. 1 and 2, consider the effects of all these factors together in single equation to determine the effect of the slope inclination on the bearing capacity. The slope height was not considered in the presented equation as only the foundation failure was considered in the analysis, not the slope failure (toe and base failure). Initially, the slope height (H/B) was also considered in the analysis, but it was observed that its effect is very nominal with respect to the bearing capacity. However, in marginally stable slopes, the slope height has a significant influence. In a marginally stable slope, the slope failure induced by the footing loading governs the capacity, not the shear failure, which can be clearly seen from Figs. 3(f) and Fig. 7(a).

A linear multiple regression analysis was also performed to determine the critical factors affecting the bearing capacity. Based on the P values, the order of significant factors affecting the bearing capacity is also evaluated. The order of the factors is $c_u/(\gamma B)$ > Slope inclination > Embedment depth of footing > Edge distance. The relative importance of all these factors was again assessed based on Garson's algorithm [43], and a similar order was obtained in this case also. The relative importance of these variables is presented in Table 3. Acharyya and dey [19] have also provided a similar rating for the *c*-φ soil slope based on an ANN. This indicates that the bearing

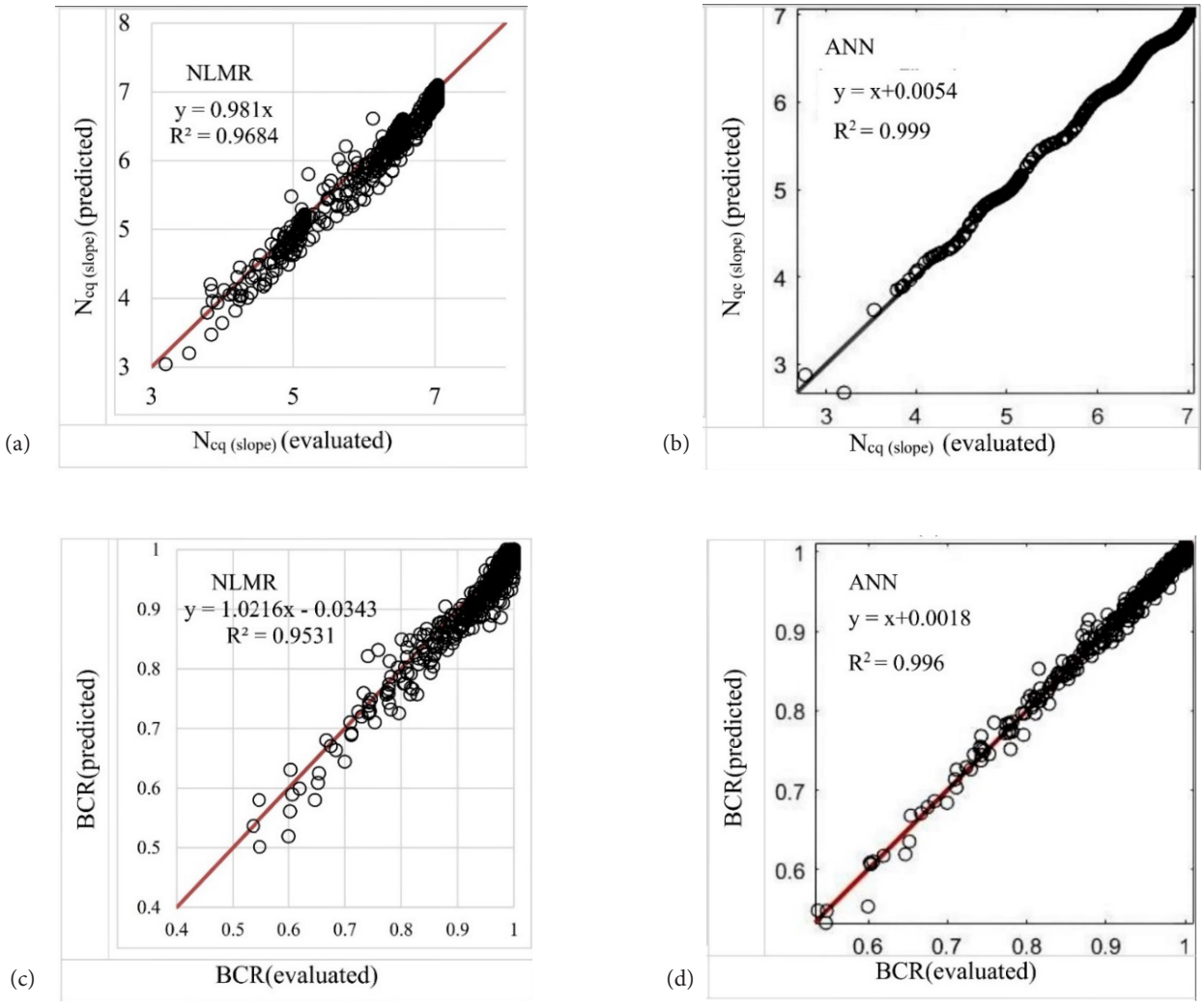

Figure 12. Comparison of the predicted values with the determined values:
(a) N_{cq}(slope) using NLMR analysis, (b) N_{cq}(slope) using ANN, (c) BCR using NLMR analysis, (d) BCR using ANN.

capacity is greatly affected by the soil strength, followed by the steepness of the slope, which is a destabilizing factor, and the embedment depth of the footing and the edge distance have the least influence on the BCR. In contrast to cohesive soils, the influence of the depth ratio is found to be less than the edge distance in cohesionless soils. This is due to the fact that the slip line/fracture surface spread over a larger lateral extent in the cohesionless soil than in the cohesive soil, which makes the lateral dimension (edge distance) more important than the vertical dimension (depth of footing).

Table 3. Relative importance of all four variables.

Factors	*Rating*	Relative importance
$c_u/(\gamma B)$	1	45.6 %
Slope inclination (β)	2	40.5 %
Depth ratio (D/B)	3	8.5 %
Edge distance (b/B)	4	5.4 %

An artificial neural network (ANN) model was also developed to determine the bearing capacity of the footing on the slope using the Levenberg-Marquardt algorithm and MATLAB. The ANN was added to compare the efficiency of the regression analysis with a regression analysis. In the model, 70% of the data (420) was used for training purposes and the remaining 30% of the data (180) was used for testing and validation purposes. Similar to the regression analysis, a total of four independent variables (i.e., b, β, $c_u/(\gamma B)$ and D/B) were used as the input, and BCR and Ncq were the output variables. Eight hidden layers were used in the study. Each hidden layer had 10 hidden neurons, which is based on the formula $2(n + 1)$. Here, 'n' is the number of input variables, which is equal to four in the present cases. A comparison of the predicted values with the determined values of N_{cq} with a nonlinear multiple regression analysis (NLMR) and the ANN is presented in Figs. 12 (a) and 12 (b), respectively. Similarly, a comparison of the predicted values with the determined values of the BCR with the NMRA and ANN is presented in Figs. 12 (c) and 12 (d), respectively.

Both methods predict the N_{cq} and BCR accurately (as R^2 is relatively high for both methods); however, the efficiency of the ANN of is found to be relatively higher than the NMRA. This means the ANN modeled the nonlinearity more accurately than the MMRA. However, the ANN method has many limitations due the black-box approach [44]. NLMR also has an advantage over ANN, as it gives simple equations to predict the bearing capacity factor and BCR, which can be easily used by researchers and engineers.

7 VALIDATION OF THE PROPOSED EQUATION

To validate the presented equation, the predicted values are compared with the results of previous studies and are presented in Fig. 13. Fig. 13 (a-b) presents the normalised bearing capacity ($q/\gamma B$) for various values of $c_u/(\gamma B)$ for cohesive soil. These plots show that the bearing-capacity values are close to those determined by Kusakabe et al. [4]. Kusakabe et al. [4] also presented the ($q/\gamma B$) values determined by other researchers, i.e., Bishop [45], Kotter and Bishop. These values have also been used for comparison purposes. As seen from Fig. 13 (a), the solution obtained with the presently used finite element model is less than the upper-bound solution of Kusakabe et al. [4], Bishop [45] and Kotter's solution. However, the values of the present study are found to be always greater than the lower-bound solution of Kusakabe et al. [4] and Fellenius's solution.

Fig. 13 (b) shows that the bearing capacity factor values predicted from the NLMR analysis are close to those determined in the numerical analysis and the previ-

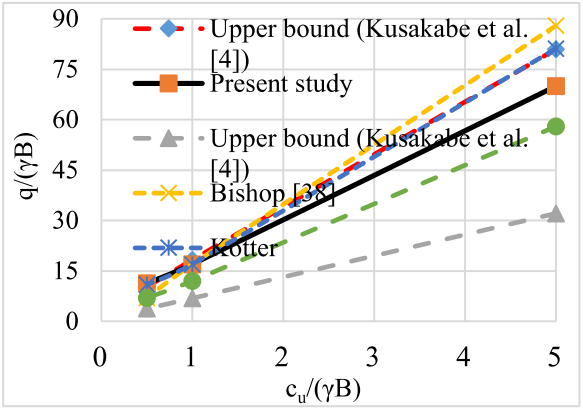

(a)

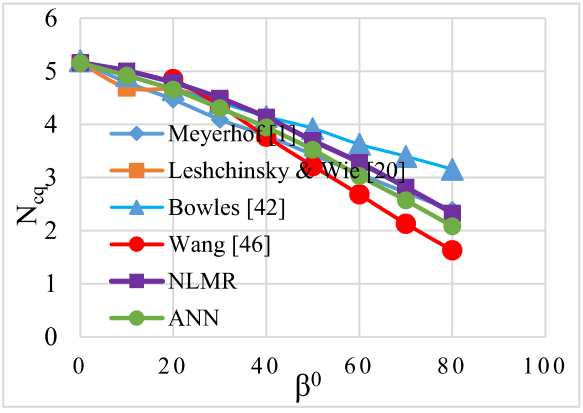

(b)

Figure 13. Comparison of the predicted values with previous studies: (a) Effect of $c_u/(\gamma B)$, (b) Effect of slope inclination.

ously determined values of Meyerhof [1], Bowles [42] and the experimental study of Wang [46]. The values of the predicted bearing capacity factor are close to the experimental study result of Wang [46] for a small slope inclination. However, the predicted values are slightly higher than the experimentally determined values of Wang [46] and lower than the values of Bowles [42]. The predicted bearing capacity factors are found to be close to the values proposed by Meyerhof [1]. However, for steep slopes ($\beta > 40°$), the values are lower than the Meyerhof [1] values. This similar observation was made in previous studies of a cohesionless soil slope [47-48]. The values predicted from the ANN are less than the earlier studies, except for the experimentally determined values of Wang et al. [40]. Similar to the present study, a number of other studies also found that small-scale model testing generally underestimates the bearing capacity of a footing on a slope [49].

8 CONCLUSION

The presence of a slope, close to a footing, influences the bearing capacity of the footing. The severity of the slope effect depends on the footing location, the soil strength and the slope geometry. However, the slope effects are found to be independent of the soil strength in the case of a stable slope (in the case of bearing-capacity failure). The bearing capacity is a minimum when the footing is resting exactly on the slope crest and it increases with the increase in the edge distance. The critical edge distance varies from 1B to 5B, depending on various factors. In contrast to the present finding, currently codes suggest the critical setback distance mainly based only on the slope inclination and the slope height. The range of critical setbacks in cohesive soils is significantly less than in cohesionless soils. The increase in the bearing capacity with the edge distance is relatively large and non-linear in the case of the steep slopes and footings of the higher depth of the embedment. The critical value of the edge distance is identified in the present study and it is found to increase with an increase in the slope inclination and the embedment depth of the footing.

In gentle slopes, shear failure governs the footing capacity. Two failure mechanisms, i.e., slope failure and bearing-capacity failure, can co-exist in steep slopes. In a few cases, the slope fails due to the stress generated from the footing loading itself. The influence of the strength parameter on the BCR and the critical edge distance is different in cohesive soils, compared to cohesionless soils. The BCR decreases with an increase in the strength of a cohesionless soil, whereas it increases with an increase in the undrained strength in cohesive soils. In contrast to cohesionless soils, the critical edge distance is found to decrease with an increase in the undrained strength of the cohesive soil. This contradictory behavior is ascribed to the differences in the failure mechanisms of the cohesive and noncohesive soils. The range of the critical edge distance is found to vary from 1B to 5B in cohesive soil.

Both the ANN and NLMR analyses were used to predict the BCR and Ncq (slope). The developed nonlinear regression equations are found to be efficient in predicting the bearing capacity factor on the slope and the BCR accurately. However, the ANN is found to be relatively more efficient at predicting the BCR and the N_{cq} (slope) values, compared to the NLMR analysis.

Acknowledgment

Authors are thankful to the anonymous reviewers for their valuable suggestions. Authors are also grateful to the Optum Computational Engineering for providing the OptumG2 program free of cost and their constant support throughout the study.

REFERENCES

[1] Meyerhof, G.G. 1957. The ultimate bearing capacity of foundation on slopes, 4th Int. Conf. on Soil Mech. and Foundation Eng. 3, 384-386.

[2] Shukla, R.P., Jakka, R.S. 2017. Critical Setback Distance for a Footing Resting on Slopes. Acta Geotechnica Slovenica 14(2), 19-31.

[3] Huang, C.C., Kang, W.W. 2008. The effects of a setback on the bearing capacity of a surface footing near a slope. J. Geo Eng. 3(1), 25-32.

[4] Kusakabe, O., Kimura, T., Yamaguchi, H. 1981. Bearing capacity of slopes under strip loads on the top surfaces. Soils and foundations 21(4), 29-40. doi.org/10.3208/sandf1972.21.4_29

[5] De Simone, P. 1987. Bearing capacity of footings on clay slopes by means of BEM. Engineering analysis 4(4), 209-213. doi.org/10.1016/0264-682X(87)90044-X

[6] Jao, M., Ahmed, F., Muninarayana, G., Wang, M.C. 2008. Stability of eccentrically loaded footings on slopes. Geomechanics and Geoengineering, An International Journal 3(2), 107-111. doi.org/10.1080/17486020802010772

[7] Georgiadis K. 2010. Undrained bearing capacity of strip footings on slopes. Journal of Geotechnical and Geoenvironmental Engineering 136(5), 677-685. doi.org/10.1061/(ASCE)GT.1943-5606.0000269

[8] Al-Jubair, H.S., Abbas, J.K. 2007. Bearing capacity

of eccentrically loaded strip footing near the edge of cohesive slope. Tikrit Journal of Engg. Science 14(2), 32-48.

[9] Abbas, J.K., Sabbar, A.S. 2011. Finite element analysis for bearing capacity of rectangular footing resting near sloped cohesive soil. Tikrit Journal of Engineering Science 18(3), 33-41.

[10] Georgiadis, K., Chrysouli, E. 2011. Seismic bearing capacity of strip footings on clay slopes. 15th European Conf. on Soil Mechanics and Geot. Engg., 723-728. doi.org/10.1061/(ASCE)GT.1943-5606.0000269

[11] Gill, K.S., Choudhary, A.K., Jha, J.N., Shukla, S.K. 2012a. Load-bearing capacity of the footing resting on a reinforced fly ash slope. Journal of Civil Engineering and Architecture 6(5), 627-632. doi.org/10.17265/1934-7359/2012.05.011

[12] Gill, K.S., Choudhary, A.K., Jha, J.N., Shukla, S.K. 2012b. Load bearing capacity of footing resting on the fly ash slope with multilayer reinforcements. Geo-Congress 2012, 4262-4271. doi.org/10.1061/9780784412121.438

[13] Farzaneh, O., Mofidi, J., Askari, F. 2013. Seismic bearing capacity of strip footings near cohesive slopes using lower bound limit analysis. In 18th Int. Conf. on Soil Mechanics and Geotechnical Eng., Paris.

[14] Mirzababaei, M., Mohamed, M., Miraftab, M. 2016. Analysis of strip footings on fiber-reinforced slopes with the aid of particle image velocimetry. Journal of Materials in Civil Engineering 29(4), 04016243. doi.org/10.1061/(ASCE)MT.1943-5533.0001758

[15] Luo, N., Bathurst, R.J. 2017. Reliability bearing capacity analysis of footings on cohesive soil slopes using RFEM. Computers and Geotechnics 89, 203-212. doi.org/10.1016/j.compgeo.2017.04.013

[16] Baazouzi, M., Mellas, M., Benmeddour, D., Mabrouki, A. 2017b. The Behaviour of Shallow Foundation Near Slope Under Inclined Loading. Innovative Infrastructure Geotechnology 275-286, Springer, Cham. doi.org/10.1007/978-3-319-61905-7_24

[17] Baazouzi, M., Mellas, M., Mabrouki, A., Benmeddour, D. 2017a. Effect of the Slope on the Undrained Bearing Capacity of Shallow Foundation. Int. Journal of Eng. Research in Africa 28, 32-44. doi.org/10.4028/www.scientific.net/JERA.28.32

[18] Aminpour, M.M., Maleki, M., Ghanbari, A. 2017. Investigation of the effect of surcharge on behavior of soil slopes. Geomechanics and Engineering, An Int'l Journal13(4), 653-669. doi.org/ 10.12989/gae.2017.13.4.653

[19] Acharyya, R., Dey, A., Kumar, B. 2018. Finite element and ANN-based prediction of bearing capacity of square footing resting on the crest of c-φ soil slope. Int. Journal of Geotechnical Engineering 1-12. doi.org/10.1080/19386362.2018.1435022

[20] Leshchinsky, B., Xie, Y. 2016. Bearing Capacity for Spread Footings Placed Near c-ϕ Slopes. Journal of Geotechnical and Geoenvironmental Engineering 143(1), 06016020. doi.org/10.1061/(ASCE)GT.1943-5606.0001578.

[21] Acharyya, R., Dey, A. 2018. Assessment of bearing capacity and failure mechanism of isolated and interfering strip footings on sloping ground. International Journal of Geotechnical Engineering 15(12), 2766-2780. Doi.org/: 10.1080/19386362.2018.1540099).

[22] Khajehzadeh, M., Taha, M.R., El-Shafie, A., Eslami, M. 2012. A modified gravitational search algorithm for slope stability analysis. Engineering Applications of Artificial Intelligence 25(8), 1589-1597. doi.org/10.1016/j.engappai.2012.01.011

[23] Raihan, T.M., Mohammad, K., Mahdiyeh, E. 2013. A new hybrid algorithm for global optimization and slope stability evaluation. Journal of Central South University 20(11), 3265-3273. doi.org/10.1007/s11771-013-1850-y

[24] Zhang, G., Tan, J., Zhang, L., Xiang, Y. 2015. Linear regression analysis for factors influencing displacement of high-filled embankment slopes. Geomechanics and Engineering 8(4), 511-521. doi.org/10.12989/gae.2015.8.4.511

[25] Zhao, Z., Wei, Z. 2017. Study on the safety distance of strip footing on cohesive soil slope. Journal for forestry engineering 2(1), 130-134. doi.org/10.13360/j.issn.2096-1359.2017.01.023.

[26] Optum G2 [Computer software]. OptumCE, Copenhagen, Denmark.

[27] Makrodimopoulos, A., Martin, C.M. 2006. Lower bound limit analysis of cohesive-frictional materials using second-order cone programming. International Journal for Numerical Methods in Engineering 66(4), 604-634.

[28] Makrodimopoulos, A., Martin, C.M. 2007. Upper bound limit analysis using simplex strain elements and second-order cone programming. International journal for numerical and analytical methods in geomechanics 31(6), 835-865.

[29] Krabbenhøft, K., Lyamin, A.V., Sloan, S.W. 2007. Formulation and solution of some plasticity problems as conic programs. Int. Journal of Solids and Structures 44(5), 1533-1549.

[30] Krabbenhøft, K., Lyamin, A.V., Sloan, S.W. 2008. Three-dimensional Mohr–Coulomb limit analysis using semidefinite programming. International

Journal for Numerical Methods in Biomedical Engineering 24(11), 1107-1119. https://doi.org/10.1002/cnm.1018
[31] Krabbenhoft, K., Lyamin, A., Krabbenhoft, J. 2015. Optum computational engineering, (www.optumce.com).
[32] Terzaghi, K., Peck, R.B., Mesri, G. 1996. Soil mechanics in engineering practice. John Wiley and Sons.
[33] Kezdi, A. 1974. Handbook of soil mechanics. Elsevier, Amsterdam.
[34] Cure, E., Sadoglu, E., Turker, E., Uzuner, B.A. 2014. Decrease trends of ultimate loads of eccentrically loaded model strip footings close to a slope. Geomech. Geoeng. 6(5), 469-485.
[35] Narita, K., Yamaguchi, H. 1990. Bearing capacity analysis of foundations on slopes by use of log-spiral sliding surfaces. Soil and Foundations 30(3), 144-152. doi.org/10.3208/sandf1972.30.3_144.
[36] Shukla, R. P., Jakka, R. S. 2018. Critical setback distance for a footing resting on slopes under seismic loading. Geomechanics and Engineering, 15(6), 1193-1205. doi.org/10.12989/gae.2018.15.6.1193
[37] Varzaghani, I.M., Ghanbari, A. 2014. A new analytical model to determine dynamic displacement of foundations adjacent to slope. Geomech. Geoeng. 6(6), 561-575.
[38] IRC. 2015. International residential code for one- and two-family dwellings. International Code Council, Country Club Hills, IL.
[39] Uniform Building Code (UBC) 1997. Uniform Building Code. International Conference of Building Officials, Whittier, California, USA.
[40] Hansen, J.B. 1970. A revised and extended formula for bearing capacity, Bulletin 28, 5-11. Copenhagen: Danish Geotechnical Institute.
[41] Vesic, A.S. 1973. Analysis of ultimate loads of shallow foundations, Journal of the Soil Mechanics and Foundations Division 99(1), 45-73. doi.org/10.1016/0148-9062(74)90598-1
[42] Bowles, J.E. 1988. Foundation engineering and design, 5th Edition, McGraw-Hill, Inc.
[43] Garson, G.D. 1991. Interpreting neuralnetwork connection weights, AI Expert, 6(4), 46–51.
[44] Tu, J.V. 1996. Advantages and disadvantages of using artificial neural networks versus logistic regression for predicting medical outcomes. Journal of clinical epidemiology 49(11), 1225-1231.
[45] Bishop, A.W. 1955. The use of the slip circle in the stability analysis of slopes. Géotechnique 5(1), 7-17. doi.org/10.1680/geot.1955.5.1.7
[46] Wang, M.J. 1986. Ultimate bearing capacity of a continuous foundation on top of a clay slope. Master of Science degree dissertation, The University of Texas, El Paso, USA.
[47] Saran, S., Sud, V., Handa, S. 1989. Bearing capacity of footings adjacent to slopes. ASCE, J. Geotech. Eng. 115(4), 553–573. /doi.org/10.1061/(ASCE)0733-9410(1989)115:4(553)
[48] Shields, D., Chandler, N., Garnier, J. 1990. Bearing capacity of foundations in slopes. ASCE, J Geotech. Eng. 116(3), 528-537. doi.org/10.1061/(ASCE)0733-9410(1990)116:3(528)
[49] Omar Maher, T. 1995. Bearing capacity of surface strip foundation on geogrid-reinforced clay slope. Dept. of Civil Eng. and Mechanics, Southern Illinois University at Carbondale, 0548-0548.

RESEARCH ON A NUMERICAL MODEL OF REAL MESO-STRUCTURES IN THE NON-SHEAR ZONE OF CLAY

RAZISKAVA NUMERIČNEGA MODELA REALNIH MEZO-STRUKTUR V NE-STRIŽNEM DELU GLINE

Wei Wang *(corresponding author)*
Nanjing Institute of Technology,
Institute of Civil Engineering and Architecture
211167, Nanjing, China
E-mail: ww1177114@163.com

Binghua Zhao
Nanjing Institute of Technology,
Institute of Civil Engineering and Architecture
211167, Nanjing, China

Liwu Yu
Nanjing Institute of Technology,
Institute of Civil Engineering and Architecture
211167, Nanjing, China

Deheng Zhang
Nanjing Institute of Technology,
Institute of Civil Engineering and Architecture
211167, Nanjing, China

DOI https://doi.org/10.18690/actageotechslov.16.2.66-76.2019

Keywords

clay; mesoscopic model; numerical analysis; real meso-structures

Ključne besede

glina; mezoskopski model; numerična analiza; realne mezostrukture

Abstract

The conventional numerical simulations of rock and soil are mainly concerned with the macroscopic continuous model or the pseudo-microscopic model established using the discrete-element method (DEM). However, these adopted models are not completely consistent with actual soil samples. To explore the evolution law of the internal stresses of soil samples from the mesoscopic perspective, we proposed an image-finite-element method for studying the deflection angles and the shear stresses at four points in the non-shear zone of clay with real mesostructures. The approach allowed for a realistic distribution of the pore structures and avoided any virtualization, thereby significantly improving the veracity of the mesoscopic model. It worked by using a microscopic lens and a charge-coupled device (CCD) to capture the two-dimensional (2D) meso image in the non-shear zone, and then convert this digital image into a vector image recognized by the finite-element software (ABAQUS) through image-processing techniques, and import it into a numerical model, and then carry out a numerical calculation. For the purposes of performing a

Izvleček

Konvencionalna numerična simulacija kamnin in zemljin se v glavnem ukvarja z makroskopskim kontinuiranim modelom ali psevdo-mikroskopskim modelom, določenim z metodo diskretnih elementov (DEM). Ti modeli niso popolnoma skladni z dejanskimi vzorci zemljin. Za raziskavo pravila napredovanja notranjih napetosti vzorcev zemljin iz mezoskopske perspektive, predlagamo slikovno metodo končnih elementov za proučevanje odklonskih kotov in strižnih napetosti na štirih mestih v ne-strižnem delu gline z realnimi mezostrukturami. Takšen pristop omogoča realistično porazdelitev struktur por in preprečuje virtualizacijo, kar bistveno izboljša verodostojnost mezoskopskega modela. Deluje z uporabo mikroskopskih leč in senzorjem CCD za zajemanje dvodimenzionalne (2D) mezo-slike v ne-strižnem območju in nato pretvorbo te digitalne slike v vektorsko sliko. S tehnikami obdelave slik jo prepozna programska oprema s končnimi elementi (ABAQUS), uvozimo jo v numerični model, nato pa izvedemo numerični izračun. Za izvedbo korelacijske analize je bil na istem vzorcu

correlation analysis, the unconfined-compression (UC) test was also carried out on the same specimen. The numerical results show that there is no shear failure in the meso numerical model, which is consistent with the UC test results for the same region. And, the quantitative analysis results show that: (1) under load, the yield zones in the meso numerical model are obviously located around the pores; (2) the evolution laws of the deflection angles and the meso shear stresses at four points are different in the compression process; and (3) the pore structures play a significant role in the evolution of the deflection angles and meso shear stresses, especially around the larger and denser pores.

opravljen tudi enoosni preizkus (UC). Numerični rezultati kažejo, da v mezo-numeričnem modelu ni strižne porušitve, kar je skladno z rezultati enoosnega preizkusa v istem območju. Rezultati kvantitativne analize kažejo: (1) da so pod obremenitvijo plastična območja v mezo--numeričnem modelu očitno locirana okoli por; (2) da se pravila napredovanja odklonskih kotov in mezo-strižnih napetosti v štirih točkah v procesu stiskanja razlikujejo; in (3) da imajo strukture por pomembno vlogo pri povečanju odklonskih kotov in mezo-strižnih napetosti, zlasti okoli večjih por in gosteje razporejenih por.

1 INTRODUCTION

Understanding the connection between internal stresses from the mesoscopic perspective and the shear failure mechanism of soil is a fundamental challenge in geomechanics research. Works on the theory, testing and numerical simulations of soil from microscopic and macroscopic perspectives have led to many great achievements. For example, in theory, Borja et al. investigated the effect of the spatially varying degree of saturation on triggering a shear band in granular materials and presented variational formulations for the porous solids whose voids were filled with liquid and gas [1]. Lu and Yang pointed out that the development of shear bands was affected by the coupling strain rate and pore pressure of a material using the momentum equations of water and grains by the mixture theory [2]. Gutierrez introduced a simple elastoplastic constitutive model that adequately captured the monotonic response of granular soils under biaxial loading conditions and developed a strain-localization criterion expressed in terms of constitutive parameters [3]. As a matter of fact, these theoretical studies take into account the effects of the physical properties of the particles and macroscopic parameters on the shear failure of soil samples [4], but do not involve the influence of internal stresses from the mesoscopic perspective. In tests, developments in meso experimental techniques, like scanning electron microscopy (SEM), computer tomography (CT), ultrasonic or digital camera, etc., made the real microscopic features of soil samples more deeply understood. Most importantly, these techniques enable the precise detection of the particles' (or aggregate particles') morphology, providing a detailed position of the local pores. The observations, made by Shan et al, indicate that the soil particles were rearranged in an orientation parallel to the direction of the maximum principal stress and the maximum shear stress [5]. Bo et al. demonstrated how to determine the mineralogical properties of ultra-soft soils using X-ray diffraction and scanning electron microscope techniques [6]. Zhang et al. calculated the volume porosity of the whole specimen by analyzing the tomography images with an error of only 3.93% compared with the experimental porosity [7]. However, compared with the digital camera method, the complexity of the soil samples' preparation and the high cost of the test equipment mentioned above limit their application. For this reason, a digital camera or a microscope lens were another choice for revealing the mesostructures of geomaterials [8-10]. Yue Z Q et al. carried out quantitative investigations of the orientations, distributions and shapes of aggregates about asphalt concrete using a conventional digital camera [11]. Ghalehjough et al. showed that the shear failure mechanism of the soil changed from general towards punching shear failure with increasing particle roundness by analysing the photographs taken from a high-resolution digital camera [12]. Shao et al. developed a series of geotechnical test instruments based on a digital image measurement system [13]. Amy et al. found that the shear band thickness ranged between 6 and 9.5 times D50 and pointed out that the grain shape, angularity, and size distribution can also affect the shear band thickness using the digital image correlation (DIC) method [14]. Although the aforementioned image methods have successfully obtained the mesostructures of soil and investigated its influence on the macroscopic properties, these results only focus on the particle characteristics of the soil and do not take into account the influence of the internal pore characteristics, nor do they involve the internal stresses from the mesoscopic perspective. In numerical simulations, some researchers have simulated the effect of mesoscopic characteristics on the macro performance by setting a "weak" element in the finite-element software. For instance, Jiang et al. performed a series of biaxial-compression-test simulations by increasing the void ratio of element No.105 on methane hydrate-bearing sediment samples to simulate

the influence of the nonuniform density (mesostructures) and showed that the bifurcation of the stress and volumetric response of the elements within the shear band is more obvious during the tests [15]. Certainly, the most typical method for simulating the microscopic model of soil is DEM, which helps to study the deformation behaviour of the particle system. Bayesteh et al. developed a 2D DEM computer program to simulate the mechanism that controlled the behaviour of a granular assembly after local and random particle loss [16]. Nicot et al. discussed the dependency of the mechanical response to the imposed volumetric strain by presenting the numerical simulation with a discrete element model and micromechanical approaches [17]. Li et al. showed that it was possible to capture, using DEM, the essential features of the mechanical behaviour of granular materials under a complex stress state [18]. However, the DEM method mainly simulates granular materials, such as sand, soil-rock mixtures, and concrete, and assumes that the soil particles are rigid spheres adopted in the numerical model, which is not in accordance with the mechanical properties of actual geomaterials.

In short, the mesoscopic mechanism of the soil samples' macroscopic properties, especially the evolution laws of the internal real meso structure and its meso stress, need to be further studied. To address the issue, this paper introduced an image-finite-element method (IFEM) on the basis of previous achievements [19]. It incorporated a real meso image and a finite-element model, respectively, for investigating the evolution of the deflection angles and the internal stresses from a mesoscopic perspective on the unconfined compression simulation test. Due to the large magnification of the microscopic imaging system, the acquisition field of view is small and it is difficult to locate exactly the position of the initiation of the shear band. Therefore, the evolution of the internal stresses from the mesoscopic perspective in the non-shear zone was studied in this paper. As for the evolution of the internal stresses in the shear zone, it needs to be studied after the equipment is improved in the next step.

2 UNCONFINED-COMPRESSION SIMULATION TEST

Because the unconfined-compression (UC) test is by far the most popular technique for soil shear testing, this paper uses the UC test and the mesoscopic image-acquisition system to form a set of soil samples for the macro and micro test equipment (see Figure 1), which cannot only obtain the clay meso image conveniently, but also carry out the macroscopic compression test at the same time. In this way, the numerical results and the experimental results can be compared and analyzed.

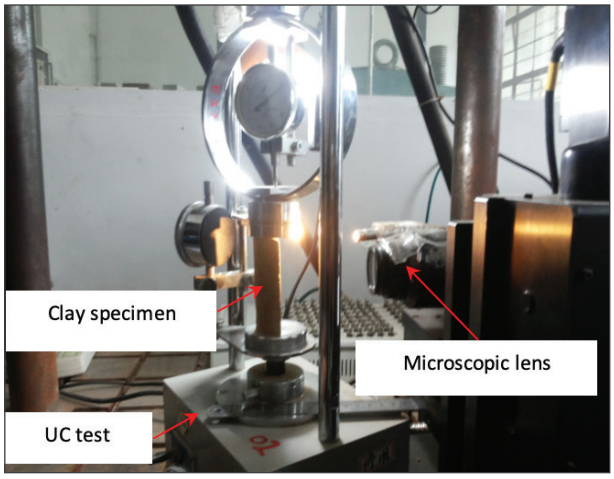

Figure 1. Equipment combining microscopic lens and UC test.

2.1 Clay sample preparation

The materials used in the test were clay, which was quarried from a construction site around the Nanjing Institute of Technology. Its plastic limit and liquid limit values were 18.36 and 39.14, respectively. The traditional cylindrical clay sample was divided into two parts from the symmetrical surface and the semi-cylindrical shape was taken as the test object (see Figure 2). The semi-cylindrical clay sample was placed on the pedestal of the UC test, and the symmetrical plane was thrown directly at the microscopic lens.

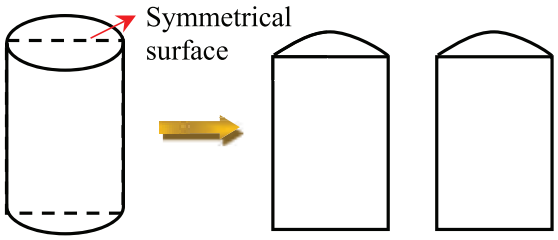

Figure 2. Schematic diagram of a clay sample divided into two parts.

2.2 Mesoscopic image acquisition

Since the surface of the cylindrical clay sample is curved, it is not convenient to collect images using the mesoscopic acquisition system with a microscopic lens and a CCD. According to the axisymmetric principle, the symmetrical surface of a semi-cylindrical clay sample was selected as the observation surface. This not only ensures that the observed area is plane, but also can collect the mesoscopic characteristics of the clay. So, the tests were carried out on the air-dried clay samples (not considering

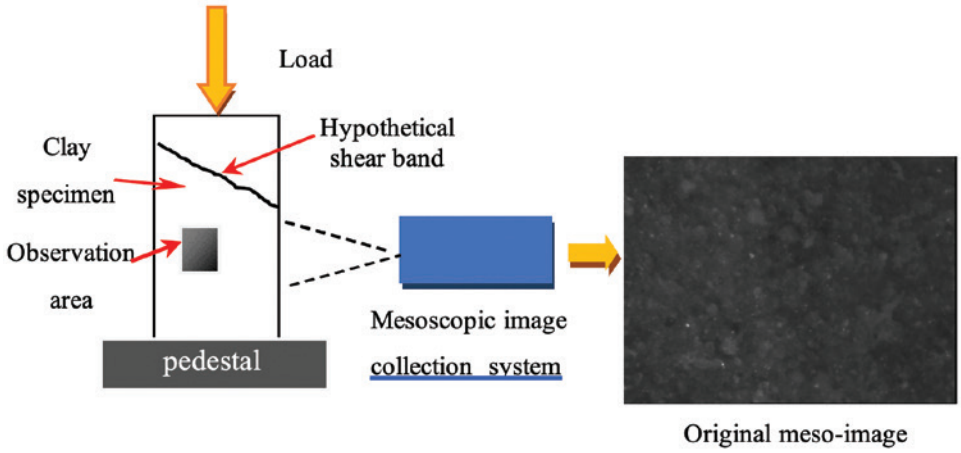

Figure 3. The original meso-image acquistion diagram.

the influence of pore water) with a 39.1-mm diameter and an 80-mm height. Then, the original images (768×576 pixels) with real mesoscopic features before loading were obtained using the mesoscopic acquisition system. Figure 3 shows a schematic diagram of the image collected by the mesoscopic acquisition system (the image has a physical resolution of 0.0014 mm).

2.3 Image processing

The original meso image contains the true distribution characteristics of the clay particle aggregates and pores, which is the basis for establishing the meso numerical model. In order to embody the mesoscopic information in the numerical model, it is also necessary to pre-process the meso image, including denoising and binarization. The image data can be affected by the noises from the device elements and the surrounding lights. Since the adaptive median filter algorithm can preserve the edges in an image, it was chosen for the de-noise operation in this paper. For studying the effects of internal stresses and pores, it is necessary to distinguish the particle aggregates from the pores, so the particle aggregates and pores were expressed in black and white using Otsu's binarization method, respectively. In fact, Otsu's method is an image binarization technique, which cannot only avoid the interference of artificial factors, but also automatically calculates the maximum threshold of intra-class variances. In this way, the real boundaries of the clay particle aggregates and pores were fully identified. The threshold of the meso image was obtained using the formula (1).

$$Q(k)=\frac{(Ave\times W(k)-Aver(k))^2}{W(k)\times(1-W(k))} \qquad (1)$$

where $Q(k)$ is the separation index of the grey class; *Ave* is the average of the grey-value; *Aver* and $W(k)$ are, respectively, the mean of the grey-level class and the sum of the grey-class histograms, which can be calculated via the equations

$$Aver(k)=\sum_{i=0}^{k}(i+1)Phs(i) \quad \text{and} \quad W(k)=\sum_{i=1}^{k}Phs(i)\ ;$$

$Phs(i)$ is the probability function of the grey level; i is the grey level, and $0 \le i \le 255$. When the $Q(k)$ value is the largest, the optimal threshold (T) is found. That is $T=k-1$. Obviously, the threshold values of the meso images are entirely different. In this study, the meso image threshold was 0.1775. So, the meso image can be processed using Otsu's method after the median filtering and the binary resultant image was obtained successfully (see Figure 4).

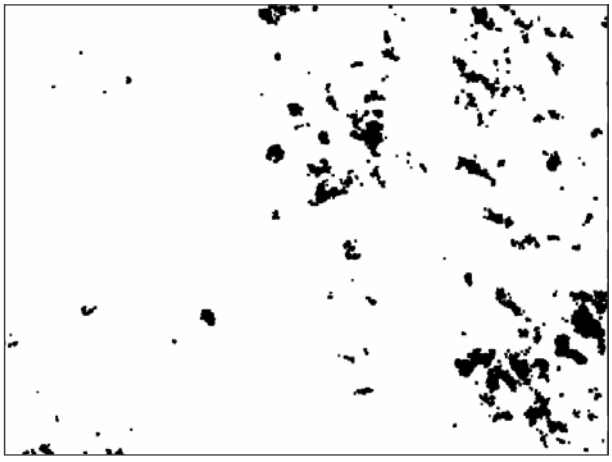

Figure 4. Binary resultant image.

2.4 Establishing the numerical model

Because the meso image is a digital image and cannot be identified by the finite-element software, it is necessary to vectorize the digital image. With the help of vector

software CorelDRAW, the digital image can be converted into a vector graph, and the numerical model containing the pore meso features can be established by importing the finite-element software (ABAQUS). In this way, the 2D numerical model with the clay real mesostructures was established successfully. Figure 5(a) shows the numerical model and Figure 5(b) gives the mesh result using the triangular element.

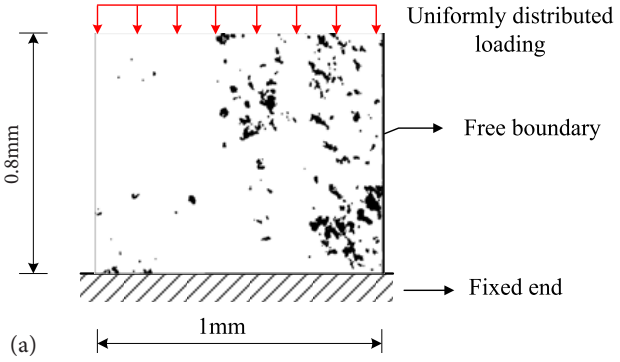

Figure 5. (a) Numerical model; (b) mesh resultant.

3 NUMERICAL ANALYSES AND RESULTS

3.1 Determination of the model parameters and the boundary conditions

In this paper, the internal stresses evolution of the air-dried clay under uniaxial compression considering the effect of pore meso characteristics is discussed. Therefore, it was assumed that the clay sample was in accordance with the Mohr-Coulomb model. The model is easy for obtaining the parameters of the material required by the finite-element software (ABAQUS) using the triaxial drained test: cohesion (c) and friction angle (φ, no dilatancy here), which is, respectively, adopted as 50 KPa and 28.51°. According to the UC test conditions, the boundary conditions of the numerical model were set up, as shown in Figure 5(a). Then, the compression process of the clay sample can be simulated by applying the same load as the UC test.

3.2 Simulation results

Based on the numerical results of the Mohr-Coulomb model, the partial regions (the red parts shown in Figure 6) present the shear yield. This is due to the fact that the shear stress in this part of the region exceeds the shear yield stress, while the others are still in an elastic state, such as the blue region shown in Figure 6. It can be seen that there is only a local yield and no through shear band in the observed region collected by the mesoscopic acquisition system, which qualitatively indicates that the numerical simulation results of the region are consistent with those of the UC test in the same region. In addition, it can be seen from Figure 6 that the yield regions are mostly like an "X" shape and mainly distributed near larger pores.

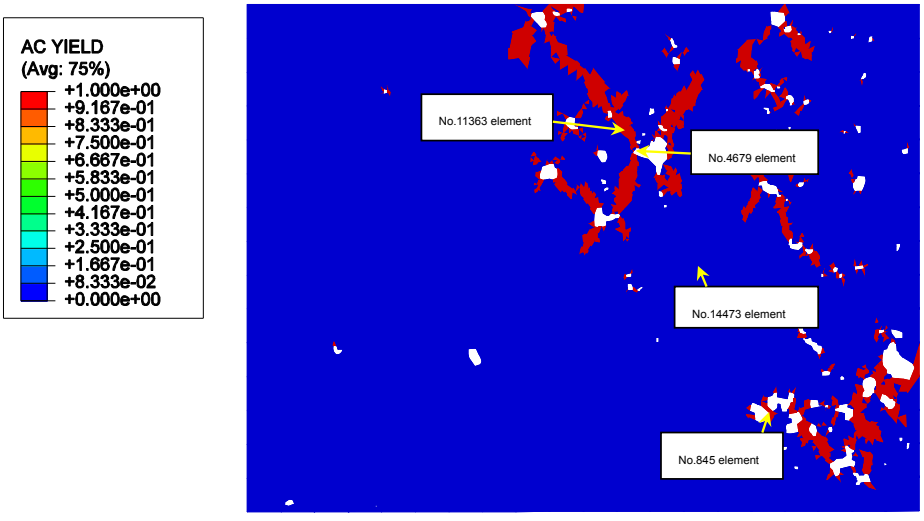

Figure 6. Profile of shear yield area.

In order to study the evolution of the internal stresses from the mesoscopic perspective, four typical points were selected, as shown in Figure 6. The first point is marked No. 4679 element in the blue region of a large pore boundary. The second point is labelled No. 845 element in a band of the red region between the two pores. The third point is located in the blue area away from the pores and labelled as the No.14473 element. The last one labelled No.11363 element is in the red region near a pore. Here are the quantitative results of the four points of the minor principle stress (σ_3), the major principle stress (σ_1), the shear stress (τ), the normal stress (σ), the shear strength (τ_f), and the deflection angle (θ).

By using the image-finite-element method, the minor principle stress, the major principle stress and the shear stress of the whole field in the observed area can be directly obtained. Tables 1 and 2 show the results at only four points. It can be seen from the data in the table that the stress values at each point are not only different but also positive and negative. It is shown that the stress states of each point are different from the mesoscopic perspective, which should be the result of the influence of the pore structures. Although it is also in the blue region, the major principle stress at point No. 4679 near the pore is about 2–2.5 times the value of the major principle stress at the No. 14473 point, far away from the pore. Similarly, even in the red region, the point No.

Table 1. Quantitative results of two points located in the red region.

Time (s)	NO. 845 element						NO. 11363 element					
	σ_3 (KPa)	σ_1 (KPa)	τ (KPa)	σ (KPa)	τ_f (KPa)	θ	σ_3 (KPa)	σ_1 (KPa)	τ (KPa)	σ (KPa)	τ_f (KPa)	θ
0.010	-0.47	-15.75	4.84	14.02	57.44	19.67	1.12	-6.11	1.34	5.72	53.04	16.31
0.020	-0.94	-31.41	9.69	27.92	64.82	19.77	2.26	-12.23	2.69	11.44	56.07	16.36
0.035	-1.60	-54.72	17.00	48.57	75.78	19.91	3.98	-21.42	4.73	20.03	60.63	16.44
0.058	-2.51	-89.27	28.01	79.02	91.94	20.12	6.61	-35.25	7.82	32.93	67.48	16.57
0.091	-4.13	-140.19	43.87	124.16	115.91	20.09	10.70	-56.13	12.56	52.34	77.78	16.80
0.104	-4.82	-159.22	49.74	141.06	124.88	20.07	12.35	-64.04	14.40	59.65	81.66	16.94
0.105	-4.81	-160.98	50.31	142.61	125.70	20.07	12.52	-64.79	14.57	60.35	82.03	16.95
0.105	-4.81	-161.02	50.32	142.64	125.72	20.07	12.52	-64.81	14.58	60.36	82.04	16.95
0.105	-4.81	-161.08	50.34	142.69	125.75	20.07	12.53	-64.83	14.58	60.39	82.06	16.95
0.105	-4.80	-161.17	50.37	142.77	125.79	20.07	12.54	-64.87	14.59	60.43	82.08	16.96
0.105	-0.57	-169.69	55.89	148.58	128.87	20.70	12.58	-64.94	14.62	60.48	82.10	16.99
0.105	-0.58	-169.73	55.91	148.60	128.88	20.70	12.60	-65.03	14.64	60.56	82.15	16.99
0.106	-0.60	-169.79	55.95	148.64	128.90	20.71	12.63	-65.16	14.67	60.68	82.21	16.99
0.106	-0.63	-169.88	56.00	148.69	128.93	20.73	12.67	-65.36	14.72	60.87	82.31	16.99
0.106	-0.68	-170.01	56.09	148.77	128.97	20.75	12.74	-65.66	14.79	61.14	82.46	17.00
0.107	-0.76	-170.22	56.21	148.89	129.04	20.79	12.84	-66.11	14.89	61.56	82.68	17.00
0.108	-0.86	-170.52	56.38	149.07	129.13	20.84	12.99	-66.79	15.04	62.19	83.01	17.01
0.110	-1.01	-170.95	56.63	149.32	129.26	20.91	13.21	-67.81	15.28	63.13	83.51	17.02
0.112	-1.23	-171.57	57.00	149.69	129.46	21.01	13.56	-69.34	15.63	64.55	84.26	17.05
0.116	-1.55	-172.48	57.52	150.22	129.74	21.16	14.07	-71.63	16.16	66.67	85.39	17.09
0.121	-0.86	-170.52	58.56	147.06	128.06	21.84	14.87	-75.09	16.97	69.85	87.08	17.16
0.129	-0.31	-168.96	58.83	145.05	126.99	22.13	16.08	-80.29	18.21	74.63	89.61	c
0.142	-0.20	-168.65	59.52	144.01	126.44	22.50	17.97	-88.15	20.09	81.83	93.44	17.47
0.160	-0.51	-169.53	60.57	143.95	126.41	22.90	21.12	-100.40	23.03	93.03	99.38	17.77
0.164	-0.66	-169.94	60.79	144.20	126.54	22.96	22.54	-104.11	24.05	96.26	101.10	18.08
0.169	-0.78	-170.28	60.98	144.38	126.64	23.02	22.16	-105.47	24.46	97.53	101.77	17.99
0.176	-0.65	-169.92	60.11	144.86	126.90	22.64	23.57	-101.51	27.15	90.50	98.04	22.09

Table 2. Quantitative results of two points located in the blue region.

Time (*s*)	NO. 4679 element						NO. 14473 element					
	σ_3 (KPa)	σ_1 (KPa)	τ (KPa)	σ (KPa)	τ_f (KPa)	θ	σ_3 (KPa)	σ_1 (KPa)	τ (KPa)	σ (KPa)	τ_f (KPa)	θ
0.010	-16.82	-13.59	3.94	12.10	56.42	20.72	-0.03	-5.46	0.18	5.45	52.89	1.87
0.020	-33.89	-27.20	7.94	24.17	62.83	20.92	-0.07	-10.91	0.36	10.90	55.79	1.91
0.035	-60.05	-47.67	14.05	42.22	72.41	21.21	-0.12	-19.10	0.65	19.08	60.13	1.97
0.058	-100.57	-78.48	23.46	69.17	86.72	21.66	-0.19	-31.39	1.12	31.35	66.64	2.06
0.091	-157.27	-121.25	37.54	105.55	106.03	22.69	-0.30	-49.90	1.90	49.82	76.45	2.20
0.104	-171.82	-133.87	42.52	115.48	111.30	23.40	-0.32	-56.88	2.22	56.80	80.15	2.25
0.105	-173.01	-135.16	43.11	116.40	111.79	23.52	-0.33	-57.55	2.25	57.46	80.50	2.25
0.105	-173.04	-135.19	43.13	116.43	111.80	23.53	-0.33	-57.56	2.25	57.47	80.51	2.25
0.105	-173.08	-135.24	43.15	116.46	111.82	23.53	-0.33	-57.58	2.25	57.50	80.52	2.25
0.105	-173.14	-135.31	43.18	116.51	111.84	23.54	-0.33	-57.62	2.25	57.53	80.54	2.25
0.105	-172.02	-135.73	43.58	116.62	111.91	23.68	-0.31	-57.67	2.28	57.58	80.56	2.28
0.105	-172.15	-135.87	43.65	116.73	111.96	23.70	-0.31	-57.75	2.28	57.65	80.60	2.28
0.106	-172.33	-136.10	43.76	116.88	112.04	23.72	-0.31	-57.86	2.29	57.77	80.67	2.28
0.106	-172.61	-136.44	43.92	117.12	112.17	23.76	-0.31	-58.04	2.29	57.95	80.76	2.28
0.106	-173.03	-136.94	44.17	117.47	112.35	23.81	-0.31	-58.30	2.31	58.21	80.90	2.28
0.107	-173.64	-137.70	44.54	117.99	112.63	23.88	-0.31	-58.69	2.33	58.60	81.11	2.29
0.108	-174.56	-138.84	45.09	118.78	113.05	24.00	-0.31	-59.29	2.35	59.19	81.42	2.29
0.110	-175.91	-140.54	45.91	119.94	113.67	24.17	-0.31	-60.18	2.40	60.09	81.90	2.30
0.112	-177.86	-143.06	47.15	121.66	114.58	24.43	-0.32	-61.53	2.46	61.43	82.61	2.30
0.116	-181.47	-146.74	48.75	124.38	116.02	24.66	-0.32	-63.55	2.55	63.45	83.68	2.31
0.121	-188.86	-151.37	50.43	128.08	117.99	24.80	-0.32	-66.60	2.69	66.49	85.29	2.33
0.129	-197.46	-158.94	53.50	133.86	121.06	25.13	-0.33	-71.17	2.91	71.05	87.72	2.36
0.142	-209.74	-169.86	58.06	142.01	125.38	25.64	-0.31	-78.11	3.27	77.97	91.39	2.41
0.160	-227.86	-185.52	64.78	153.39	131.42	26.40	-0.25	-88.83	3.84	88.66	97.06	2.49
0.164	-232.24	-190.16	67.05	156.40	133.02	26.74	-0.20	-91.58	4.00	91.40	98.52	2.51
0.169	-237.63	-194.77	69.31	159.33	134.58	27.09	-0.11	-94.39	4.19	94.20	100.00	2.55
0.176	-245.24	-200.93	72.57	162.86	136.45	27.69	0.22	-98.73	4.56	98.52	102.30	2.65

845 is significantly larger than the major principle stress at point No. 11363 because it is in a structure similar to a"slender column".

Then, using the following equation (2), which is transformed from the formula $\tau = \frac{\sigma_1 - \sigma_3}{2} sin\, 2\, \theta$, the deflection angle θ at four points can be solved at every loading state.

$$\theta = \frac{1}{2} arcsin \frac{2\tau}{\sigma_1 - \sigma_3} \qquad (2)$$

Figure 7 (a), (b), (c) and (d) are the evolution curves of the deflection angles inclined in the direction of the major principal plane, respectively. As shown in Figure 7, we can learn that, in both the red and blue regions, the deflection angles of the four points increase with the increasing load. Obviously, when the load is increased from 0 to 50% loads, although the initial deflection angle of each point is different, the evolution curve is an increasing trend, but the slope is different. This suggests that the equilibrium of the internal and external forces of the clay sample at this stage is realized by the clay particles' deflection. This is an interesting phenomenon. The deflection angle at point No. 845 is almost unchanged between 25% and 50% of the load, which may be a sign that the "slender column" reached a critical equilibrium. But, as the load continues to increase, the deflection angle at point No. 845 suddenly jumps significantly, and then increases rapidly until the maximum load. A small jump occurs at the point No. 4679 near the pore at 50% loads, like the point No. 845,

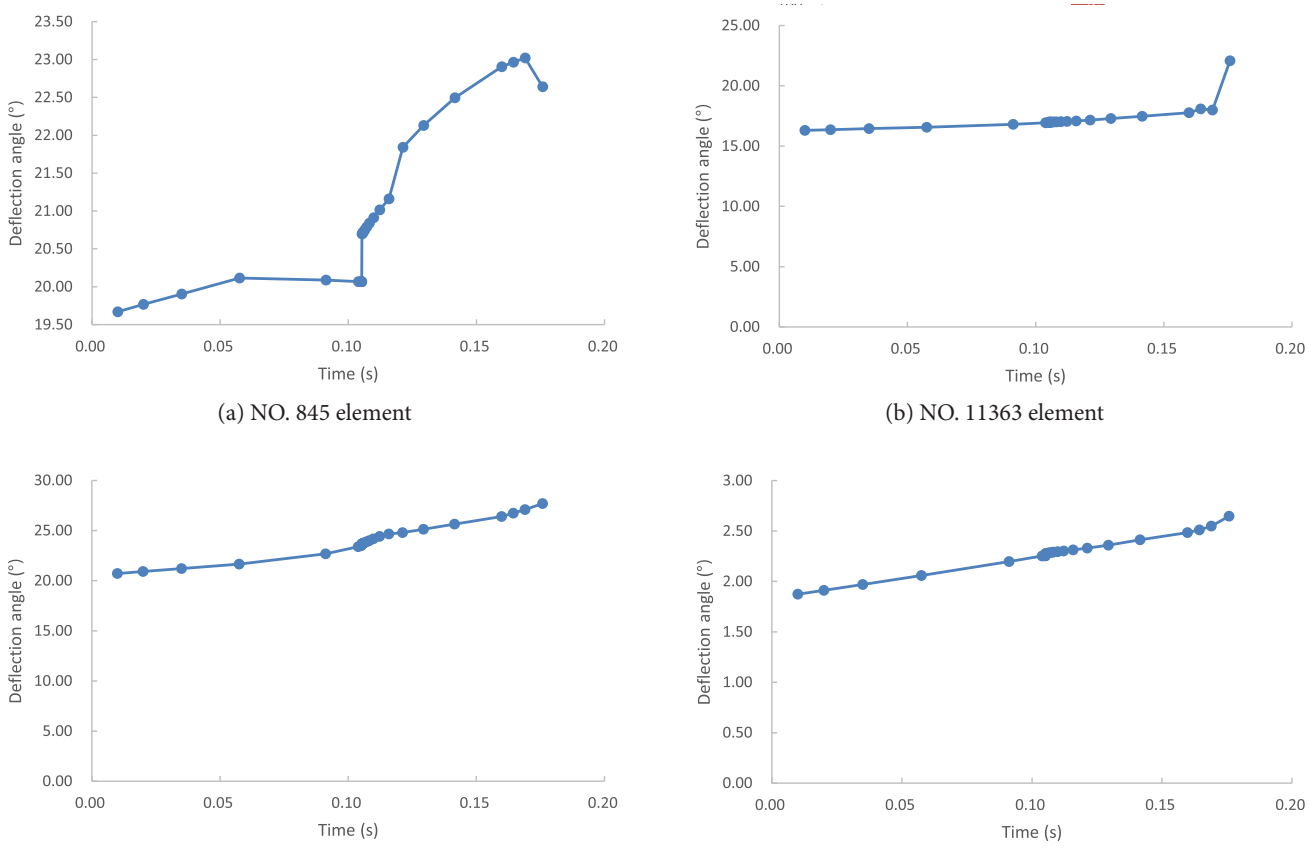

Figure 7. Evolution curves of deflection angle.

but not at the other two points. It can be seen that the mesoscopic pore characteristics will affect the movement of the clay particles. The curve slope of the point No. 845 after 50% loads is obviously higher than that of the other points, and the deflection angle is shifted from 20 degrees to 23 degrees. This indicates that there is a lack of effective constraints on the "slender column" in the area, which makes the clay particles deflect easily, thus exacerbating the growth of the major principal stress and the meso shear stress and making the region enter the plastic zone very quickly. Moreover, until near the maximum load, the deflection angle at the point No.11363 suddenly increased by 4 degrees, indicating that there might be a large dislocation at this point to cause small cracks. This might be due to the continued expansion of the local band plastic zone in which the point No. 11363 is located, as can be seen from Figure 6. In addition, the change in trend of the deflection angles at the two points No.4679 and No. 14473 in the blue region is relatively gentle, and the amplitude is not large. It can be seen that the blue part of the observed region is the main force-bearing body, which is called the main carrier, while the red part is the secondary carrier. From the above analysis, it can be concluded that the secondary carrier first enters the plastic zone under the action of the load, and gradually affects the main carrier through the adjustment until a new secondary carrier is formed. The main reason is that there are a number of weak structures in the clay sample, which are formed by the existence of pores.

Further, the normal stresses at the four points, given in Tables 1 and 2, were calculated using the following equation (3).

$$\sigma_n = \frac{\sigma_1+\sigma_3}{2} + \frac{\sigma_1-\sigma_3}{2} cos\, 2\,\theta \qquad (3)$$

Next, according to the Mohr-Coulomb yield theory, the shear strength at the four points can be drawn easily using the formula $\tau_f = c+\sigma_n \tan\varphi$. Figure 8 (a), (b), (c) and (d) show the curves of the meso shear stresses and the meso shear strengths at the four points with the increasing of loads, respectively. Figure 8 also describes the relationship between the meso shear stress and the meso shear strength at the same point. It can be seen from Figure 8 that the meso shear strength is obviously greater than that of the meso shear stress, indicating that the clay particle aggregates in the observed area are still able to withstand external loads. From Figure 8 (a) it can

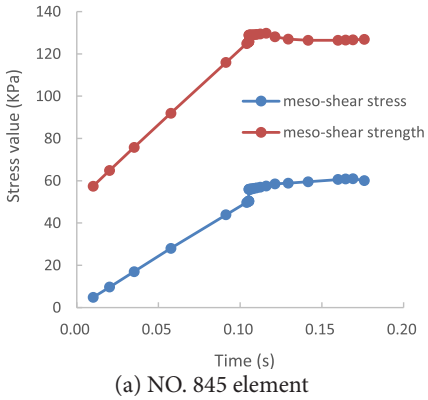

(a) NO. 845 element

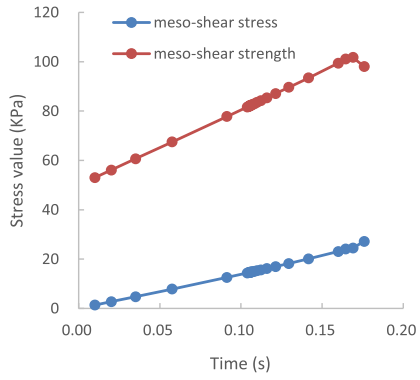

(b) NO. 11363 element

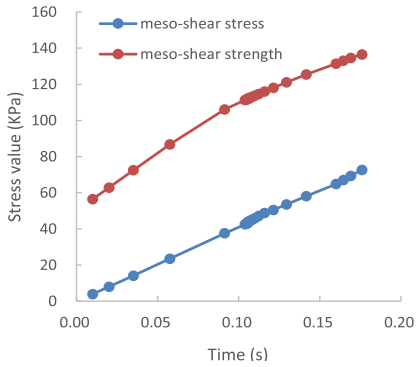

(c) NO. 4679 element

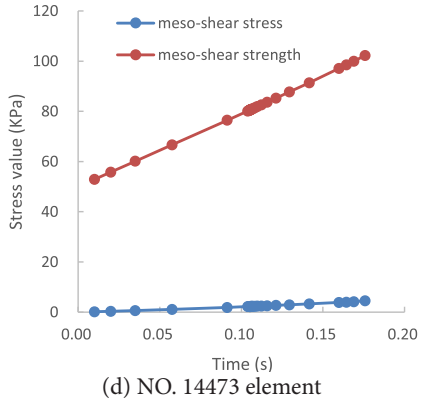

(d) NO. 14473 element

Figure 8. Profiles of meso shear stress and meso shear stress with load.

be seen that the variation curve of the meso shear stress and the meso shear strength at the point No.845 after 50% loads tends to be horizontal, which indicates that the stress state of the point No. 845 is no longer changing. Because there are pores on both sides of the site, the secondary carrier cannot affect the main carrier, and can only be connected with the main carrier through both ends. Therefore, after a certain degree of stress, the middle part cannot continue to bear a larger load. Figure 8 (b) shows that the meso shear strength at the point No.11363 begins to decrease near the maximum load, while the meso shear stress still keeps increasing. It can be seen that the dislocation of the clay particles can lead to the initiation of tiny cracks, but it does not cause damage. This is consistent with the previous conclusion. The curve slope of meso shear stress and meso shear strength at the point No.4679 is almost the same, shown in Figure 8 (c), and the final meso shear stress value is similar to that of the point No.845, which is related to the compactness degree of the clay particles weakened by its unilateral pores. A significant difference from the other points is that the meso shear stress at the point No.14473 is very slow to reach about 5 KPa (see Figure 8 (d)), which is slightly smaller than the shear strength 12 KPa of the clay sample obtained by the UC test. This indicates that the clay particle aggregates far away from pores are the main carrier, and the meso shear stress and the shear strength of the clay samples are basically in the order of magnitude. But the internal cause of shear failure of the clay samples is the evolution of secondary carriers. In short, some of the secondary carriers undergo adjustment, yielding to cracking until multiple subcarriers are connected to a single through shear band and destroyed. In fact, the meso numerical model is capable of withstanding loads, and mainly depends on the stress network intertwined by main carriers and secondary carriers. The evolution of the stress and strength in shear band should be further studied by improving the testing equipment and material parameters.

4 CONCLUSIONS

In this paper, a two-dimensional numerical analysis method for clay is proposed, which reflects the real mesoscopic characteristics, and it can also be extended to other materials. The method is to convert the digital image containing meso features information into a numerical model for the calculation and analysis. With the powerful post-processing function of the finite-element software (ABAQUS), not only can the yield position in the observed area be obtained, but also the principal stress and meso shear stress of the whole field can be easily obtained.

The evolution laws of deflection angles and meso shear stresses at four points are different in the compression process. The change of deflection angle for each point is to adapt to the external loads, they all increase with the increasing of loads, but the change range near the pores is larger, and the plastic zone is prone to dislocations appearing. Moreover, the variation of the meso shear stress and the meso shear strength at each point is also affected by the internal pore characteristics. The weak structure formed by the pores is prone to the plastic zone, which leads to the evolution of secondary carriers. Obviously, the pore structures play a significant role in the evolution of the deflection angles and the meso shear stresses, especially around the larger and denser pores.

Clay samples depend on a stable backbone of the stress network with main and secondary carriers before failure. Once multiple secondary carriers form a through shear band, the clay samples will be destroyed.

The evolution of meso stress and the influence of pore characteristics in the shear band need further study.

REFERENCES

[1] Borja, R.I., Song, X.Y., Wu, W. 2013. Critical state plasticity. Part VII: Triggering a shear band in variably saturated porous media. Compu. Meth. Appl. Mech. Eng. 261–262, 66–82. DOI: 10.1016/j.cma.2013.03.008

[2] Lu, X. B., Yang, Z.S. 1999. Development of the shear band in saturated soil. Journal of Shanghai University 3, 199. DOI:10.1007/s11741-999-0058-8

[3] Gutierrez, M.S. 2007. Effects of constitutive parameters on shear band formation in granular soils. Soil Stress-Strain Behaviour: Measurement, Modelling and Analysis, Dordrecht, 146, 691-706. DOI: 10.1007/978-1-4020-6146-2_50

[4] Kumar, N., Luding, S., Magnanimo, V. 2014. Macroscopic model with anisotropy based on micro-macro information. Acta Mech., 225, 2319-2343. DOI: 10.1007/s00707-014-1155-8

[5] Shan, Y., Mo, H.H., Yu, S.M., Chen, J.S. 2016. Analysis of the maximum dynamic shear modulus and particle arrangement properties of saturated soft clay soils. Soil Mechanics and Foundation Engineering 53(4), 226-232. DOI: 10.1007/s11204-016-9390-8

[6] Bo, M.W., Arulrajah, A., Sukmak, P., Horpibulsuk, S., Leong, M. 2016. Mineralogy and geotechnical properties of ultrasoft soil from a nearshore mine tailings sedimentation pond. Marine Georesources and Geotechnology 34(8), 782-791. DOI: 10.1080/1064119X.2015.1094158

[7] Zhang, W., Liang, X.L., Tang, X.Y., Shi, B., Xu, Y.D., Xiao, R. 2017. Fine characterization of pore structure of Nanjing silty sand using micro-CT. Chinese Journal of Geotechnical Engineering 39(4), 683-689. DOI: 10.11779/CJGE201704013

[8] Wang, F.H., Xiang, W., Corely, T., Yeh J.T., Yuan, Y.F. 2018.The influences of freeze-thaw cycles on the shear strength of expansive soil treated with ionic soil stabilizer. Soil Mechanics and Foundation Engineering 55(3), 195-200. DOI: 10.1007/s11204-018-9525-1

[9] Xing, H.Z., Zhang, Q.B., Braithwaite, C.H., Pan, B., Zhao, J. 2017. High-speed photography and digital measurement techniques for geomaterials: fundamentals and applications. Rock Mech Rock Eng. 50, 1611-1659. DOI: 10.1007/s00603-016-1164-0

[10] Wang, P.P., Sang, Y., Shao, L.T., Guo, X.X. 2018. Measurement of the deformation of sand in a plane strain compression experiment using incremental digital image correlation. Acta Geotechnica 5,1-11. DOI : 10.1007/s11440-018-0676-z(0

[11] Yue, Z.Q., Chen, S., Tham, L.G. 2003. Finite element modelling of geomaterials using digital image processing. Computers and Geotechnics 30, 375-397. DOI: 10.1016/S0266-352X(03)00015-6

[12] Ghalehjough, B.K., Akbulut, S., Celik S. 2018. Effect of particle roundness and morphology on the shear failure mechanism of granular soil under strip footing. Acta Geotechnica Slovenica 1, 43-53. DOI: 10.18690/actageotechslov.15.1.43-53.2018

[13] Shao, L.T., Guo, X.X., Zhao, B.Y. 2018. Digital image measurement system for soil specimens in triaxial tests. Proceedings of China-Europe Conference on Geotechnical Engineering, pp 611-614. DOI: 10.1007/978-3-319-97112-4_136

[14] Amy, L.R., Sara, A., Olivier, C., Andrés, D.O. 2011. Characterization of mesoscale instabilities in localized granular shear using digital image correlation. Acta Geotechnica 6(4), 205-217. DOI: 10.1007/s11440-011-0147-2

[15] Jiang, M.J., Liu, J., Shen, Z.F. 2018. Investigating the shear band of methane hydrate-bearing sediments by FEM with an elasto-plastic constitute model. Bulletin of Engineering Geology and the Environment 77(3), 1015-1025. DOI:10.1007/s10064-017-1109-1

[16] Bayesteh, H., Ghasempour, T. 2018. Role of the location and size of soluble particles in the mechanical behaviour of collapsible granular soil: a DEM simulation. Computational Particle Mechanics 1-15. DOI: 10.1007/s40571-018-00216-x

[17] Nicot, F., Sibille, L., Hicher, P.Y. 2015. Micro-macro analysis of granular material behaviour along

proportional strain paths. Continuum Mechanics and Thermodynamics 27(1-2), 173-193. DOI: 10.1007/s00161-014-0347-8

[18] Li, B., Zhang, F.S., Gutierrez, M. 2015. A numerical examination of the hollow cylindrical torsional shear test using DEM. Acta Geotechnica 10, 449-467. DOI: 10.1007/s11440-014-0329-9

[19] Wang, W., He, P.L., Zhang, D.H. 2014. Finite element simulation based on soil mesostructures extracted from digital image. Soil Mechanics and Foundation Engineering 51(1), 17-22. DOI: 10.1007/s 11204-014-9248-x

SOIL BASED DESIGN OF HIGHWAY GUARDRAIL POST DEPTHS USING PENDULUM IMPACT TESTS

ZASNOVA GLOBINE STEBRA AVTOCESTNE OGRAJE GLEDE NA LASTNOSTI TAL Z UPORABO UDARNIH PREIZKUSOV Z NIHALOM

Murat Örnek *(corresponding author)*
Iskenderun Technical University,
Faculty of Engineering and Natural Sciences,
Civil Engineering Department
31200, Iskenderun, Hatay, Turkey
E-mail: murat.ornek@iste.edu.tr

Ali Osman Atahan
Istanbul Technical University,
Civil Engineering Faculty,
Civil Engineering Department
34469, Istanbul, Turkey
E-mail: atahana@itu.edu.tr

Yakup Türedi
Iskenderun Technical University,
Faculty of Engineering and Natural Sciences,
Civil Engineering Department
31200, Iskenderun, Hatay, Turkey
E-mail: yakup.turedi@iste.edu.tr

M. Musab Erdem
Iskenderun Technical University,
Faculty of Engineering and Natural Sciences,
Civil Engineering Department
31200, Iskenderun, Hatay, Turkey
E-mail: musab.erdem@iste.edu.tr

Murat Büyük
Sabancı University,
Integrated Manufacturing Technologies R&A Center
34956, Istanbul, Turkey
E-mail: muratbuyuk@sabanciuniv.edu

DOI https://doi.org/10.18690/actageotechslov.16.2.77-89.2019

Keywords

guardrail; post; post embedment depth; soil properties; post-soil interaction; pendulum test

Ključne besede

ograja; steber; globina vpetja; lastnosti tal; interakcija steber-tla; preizkus z nihalom

Abstract

Guardrails are passive road restraint systems (RRS) used at roadsides and medians to improve road safety. In the case of inadequate post embedment depth of soil driven posts may not function as intended and design cannot provide adequate safety nor security for the impacting vehicles. In general, the height of the steel guardrails varies between 1600 and 2400mm. However, the characteristics of the soil where the guardrails are driven are not taken into consideration. In other words, a constant depth of guardrail is used regardless of the type of soil. Post embedment depths (PED) in steel guardrail systems are currently determined based on strong soil properties. The crash performance of these designs may not be appropriate for locations where soil conditions are weaker than tested conditions.

In this study, a series of field impact tests were performed on soil embedded posts to determine optimum PED for

Izvleček

Varovalne ograje so pasivni cestni zadrževalni sistemi (RRS), ki se uporabljajo ob robovih in na sredini cest za izboljšanje varnosti v cestnem prometu. V primeru nezadostne globine vpetja stebrov, vtisnjenih v zemljino, se lahko zgodi, da ne delujejo kot je predvideno, zato konstrukcija ne more zagotoviti zadostne varnosti ali varnosti za vozila, ki udarijo v njo. Na splošno je višina jeklene varnostne ograje med 1600 in 2400 mm. Vendar pa se lastnosti tal, v katerih so vgrajene varnostne ograje, praviloma ne upoštevajo. Z drugimi besedami, ne glede na vrsto tal, se izvaja konstantna globina vpetja stebrov zaščitne ograje. Globine vpetja stebrov (PED) v sistemih jeklenih zaščitnih ograj so trenutno določene na podlagi visokih trdnosti tal. Zmogljivost teh modelov za trk ni primerna za lokacije, kjer so trdnostne karakteristike tal nižje od predpostavljenih v osnovnem izračunu.

V tej študiji so bili opravljeni terenski udarni preizkusi na stebre vpete v tla, da bi določili optimalno globino vpetja

three different soil conditions, namely hard, medium hard and soft soil. A pendulum device is used to perform dynamic impact tests on C type (C120x60x4), H type (H150x90x6) and S type (S100x50x4.2) posts. Seven different PED values were used for each type of soil. A total of 63 impact tests proved that increased soil stiffness resulted reduction in PED for the posts. Optimum PED values are determined based on energy absorption of posts. With the use of optimum length guardrail posts considerable amount of installation time, labor and material savings are expected.

stebrov za tri različne trdnostne razmere v tleh, in sicer trdo, srednje trdo in mehko zemljino. Nihalno napravo uporabljamo za izvedbo dinamičnih udarnih preizkusov na stebrih tipa C (C120x60x4), H (H150x90x6) in S (S100x50x4.2). Za vsako vrsto tal je bilo uporabljenih sedem različnih vrednosti globin vpetja stebrov. Skupno je bilo tako izvedenih 63 udarnih preizkusov, s čimer se je dokazalo, da je povečana togost tal povzročila zmanjšanje globine vpetja stebrov. Optimalne vrednosti globine vpetja stebrov se določijo na podlagi absorpcije energije stebrov. Z uporabo optimalne dolžine stebrov zaščitne ograje se pričakuje precej prihranka pri času za vgradnjo, delu in materialu.

1 INTRODUCTION

The roadside can be defined as the area between the outside shoulder edge of a road and the right-of-way limits [1]. The utilization of engineering treatments in this area to improve traffic safety is referred to as roadside safety design and guardrails are one of the most widely used passive safety devices for roadsides.

Most guardrail designs in the world are made out of steel or concrete. Concrete barrier designs usually do not contain a foundation and they are simply placed on the road surface. Thus soil-barrier interaction is not an issue for concrete barriers. However, this is not the case for steel designs. Posts of the steel guardrail designs have to be either bolted to a concrete deck or driven into the soil. Therefore, the connection and any details of this connection have to be designed properly for a steel guardrail to perform as intended.

Steel-guardrail designs are mostly installed in soil, since the number of bridges in a standard highway project is limited. For steel guardrails' post-soil interaction the properties of the soil and the extent of the post embedment depth (PED) become essential parameters affecting the impact performance [2,5,6]. With a lack of post-soil interaction or an inadequate PED a steel guardrail might not function as intended and the design cannot provide adequate safety nor security for the impacting vehicles. In general, the height of the steel guardrails varies between 1600 and 2400 mm. However, the characteristics of the soil where the guardrails are driven are not taken into consideration. In other words, a constant depth of guardrail is used, regardless of the type of soil. Unfortunately, the PEDs in steel guardrail systems are currently determined based on strong soil properties [3]. The crash performance of these designs might not be appropriate for locations where the soil conditions are weaker than the tested conditions.

The European crash-test standard EN131 is a performance-based standard. In other words, regardless of the properties of the guardrail elements, only the impact-response behavior of the guardrail is considered [4]. The adequacy of guardrail systems is evaluated using the EN1317 standard and successful designs receive certification for highway use. This standard has been mandatory in Turkey since 2011 and it provides crash-test procedures and acceptance criteria for crash tests. Even though the guardrail post-soil interaction and the soil properties are of importance in crash tests, EN1317 does not provide detailed information on this topic. There are not many studies in the literature about the post-soil interaction based on experimental or numerical analyses. This is why the crash-test standards do not contain any details or details of the soil properties. The behavior of sigma-type posts under semi-static and dynamic loading on gravel soil were investigated with experimental and numerical modeling by Wu and Thomson [6]. They used a standard PED in the tests and modelled in the numerical analyses. Atahan and Cansız [2] analyzed the crash tests of the guardrails of circular wooden posts used in the United States. Full-scale crash-test results were simulated and detailed LS-DYNA analyses were carried out. It is recommended that the PED can be reduced in order to improve the behavior of the guardrail system and energy absorption. The behavior of a vehicle impacted guardrails applied on surfaces with variable inclination was investigated by Atahan [7]. The study was based on the crash effect of the vehicle existing in the slopes. In the study, the slopes are modelled as 1:1, 2:1, 4:1, 6:1, 8:1 and 10:1 (horizontal: vertical) and the stability of the vehicle and the adequacy of the guardrail system during the vehicle crash are examined using a software LS-DYNA program. The results showed that vehicles on 4:1 and more slopes could interact more securely with the guardrail system. A similar study was carried out by Marzougui et al. [8]. The purpose of this study is to investigate the use of rope guardrails in safety zones. The rope guardrails with different geometries, vehicles and surface inclinations

were studied as variables using the LS-DYNA program. Vehicle safety was studied and used to determine the most suitable configurations for rope guardrails. Polivka et al. [9] investigated the vehicle stability by driving a 2:1 (horizontal: vertical) slope guardrail system. The study involved an actual crash test and the guardrail system was able to stop the crashing vehicle safely. A study was conducted by Reid [5] to demonstrate road safety using the LS-DYNA program. In this study it was shown that how efficient the LS-DYNA program is and how accurately it can predict the dynamic interactions. Sheikh and Bligh [10] conducted a study on the effect of the inclination of the refugees on vehicle behavior and accordingly the selection of the concrete barrier locations. An optimization study was carried out on the selection of the location of concrete barriers for different slopes using the LS-DYNA program. In addition, Bonin et al. [11] and Atahan et al. [3] conducted a structural efficiency analysis of many road-safety structures using the LS-DYNA program. The structures examined in these studies are crossing guardrails, bridge barriers, energy-absorbing crash posts and guardrails. The effects of water content, lime content and compaction energy on the compaction characteristics of lime-treated loess highway embankments were investigated using laboratory and in-situ compaction tests [14]. The maximum dry density and the optimum water content of loess with different lime contents were determined. The results indicate that the maximum dry density increases due to the increase of the water content. It was also reported that a higher water content and compaction energy is needed for the optimum compaction. Woo et al. [15] used the conventional 3D finite-element approach and the hybrid approach that combines Lagrange and SPH (smoothed particle hydrodynamics) elements to evaluate the response of a laterally loaded single guardrail post with a square tube embedded in the sloping ground. They reported that these approaches seem to be suitable to model the ground slope, as well as to obtain the response of the soil-post system dominated by bending deformations. El-Maaty [16] investigated the effect of including different reinforcement types on reducing the rapid accumulation of pavement damage caused by freeze–thaw cycles or the low strength of a silty pavement foundation. The CBR strength and freeze-thaw behavior were tested with the inclusion of randomly distributed fibers, chemical additives and waste or by-product materials. It is concluded that the unsubmerged samples reinforced with waste materials provided a significant improvement in the CBR strength and the best performance was observed with the submerged samples treated with chemical additives of 10%. Grouting is an effective way to improve the strength characteristics significantly and can also contribute to the stabilization of sand. Gamil et al. [17] developed a simulation and instrumental setup to be used for cement grouting. The shear strength of the sand was recorded before and after the grouting procedure. They reported that the shear strength increased after injecting the sand with cement and the setup produced accurate grouted samples with an even distribution of the cement mix. Hussain [18] examined the effect of the compaction energy of the engineering properties, i.e., compaction characteristics, unconfined compressive strength, California bearing ratio and the swell percentage of the soil. Substantial improvements in these properties were obtained in the tests. It is reported that compacting the soil at higher compaction energy levels can provide an effective approach to the stabilization of expansive soils up to a particular limit. The swell potential is increased due to the reduction in the permeability of the soil when the soil is compacted more than this limit.

As seen from studies in the literature, the design of the guardrail systems are planned without soil conditions. In general, a constant depth of guardrail is used regardless of the type of soil. Actually, the soil conditions directly affect the post embedment depths (PEDs) in steel guardrail systems. In other words, it is not a proper engineering approach to use the same PEDs for different soil characteristics. This study focused directly on the performance of the guardrails under different soil conditions. In this study, a series of field pendulum-impact tests were conducted in Iskenderun, Hatay, Turkey. These tests were performed on soil embedded posts to determine the optimum PED for three different soil conditions, i.e., hard, medium-hard and soft soil. A pendulum device was used to perform the dynamic impact tests on C-type (C120×60×4), H-type (C150×90×6) and S-type (S100×50×4.2) posts. Seven different PED values were used for each type of soil. These values are varied from 600 mm to 900 mm for C-type posts; varied from 700 mm to 1300 mm for H-type and S-type posts. A total of 63 impact tests performed proved that the increased soil stiffness resulted a reduction in the PED for the posts. Optimum PED values were determined based on the energy absorption of the posts. With the use of optimum-length guardrail posts a considerable amount of installation time, labor and material savings are expected.

2 FIELD TESTS

2.1 Site Characterization

Three different soil pits were prepared for the field impact testing. The dimensions of these pits were 1.0 m wide × 60.0 m long × 1.5 m deep, as shown in Figure 1. A total of 63 posts with 1.0 m spacing were installed

Figure 1. Preparation of soft, medium hard and hard soil pits for post installation.

in these three soil pits. The dimensions of the soil pits were selected based on the largest PED used in the study, potential post removal during tests, prevention of any interaction between posts and economic considerations.

The soil used in the pits represents the standard base granular material used by the Turkish Road Authorities [12]. To determine the geotechnical properties of the granular material to be used in these pits a series of laboratory tests, such as grain-size analysis, moisture content, field density, unit weight, shear box, standard and modified proctor tests were performed. The results of these experiments are presented in Table 1. The grading curve of the granular material used in the tests is given in Figure 2. After the laboratory tests, selected granular materials were used to construct the pits. Sand Cone and California Bearing Ratio tests were used to verify the density of the granular material for hard, medium-hard and soft soil conditions. The results of these field tests are listed in Table 2. As shown, acceptable soil stiffness levels were reached before the initiation of the post-installation procedure. At the same time, the density indices of the soil pits are 80%, 88% and 95% for the loose, medium-hard and hard soil conditions, respectively.

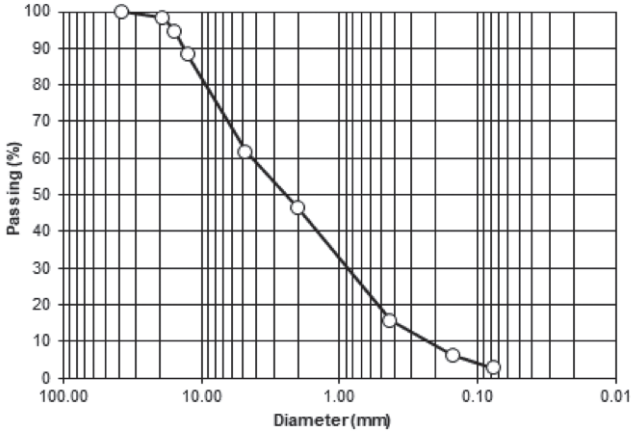

Figure 2. Grading curve of the granular material used in the tests.

Table 1. Geotechnical properties of the soil from laboratory tests.

Parameter	Property
Soil classification	SP (USCS); A3 (AASHTO); Sand (triangular classification)
Water content	4 %
Dry density	max: 21.0 kN/m^3; min: 16.0 kN/m^3
Particle density	25.3 kN/m^3
Internal friction angle	soft: 36°; medium hard: 44°; hard: 48°
Max. dry density and optimum water content (standard proctor test)	γ_{kmax} = 21.0 kN/m^3; ω_{opt} = 8%
Max. dry density and optimum water content (modified proctor test)	γ_{kmax} = 22.0 kN/m^3; ω_{opt} = 7%

Table 2. Geotechnical properties of the soil from field tests.

Name	Test Result
Sand Cone Test	Loose: 17.0 kN/m^3 Medium dense: 18.5 kN/m^3 Dense: 20.0 kN/m^3
CBR Test	Loose: 36% Medium dense: 64% Dense: 95%

2.2 Details of guardrail posts used and experimental setup

Three different shaped posts, i.e., C-type (C120×60×4), H-type (H150×90×6) and S-type (S100×50×4.2) are used in this study. Typical views of the posts are given in Figure 3. As shown in Tables 3–5, the PED ranged from 650 mm to 900 mm for C-type posts, ranged from 700 mm to 1300 mm for H-type and S-type posts for all three soil conditions. In this table from the test codes, the letter gives the soil type and the numbers indicate the PED values. The posts were driven into the soil using a post-installation machine and a picture of the installation procedure is shown in Figure 4. To deliver the impact forces to the posts, a 1 kg pendulum device was

(a) C type posts

(b) H type posts

(c) S type posts

Figure 3. Typical views of the posts used in the study.

used. The pendulum was raised 1.5 m using an electric motor and the impacted posts about 550 mm above ground level. This distance represents the bumper height of an average small car. In this test setup, the pendulum applied 14.7 kJ of kinetic energy to the posts. A picture of the pendulum used in this study is shown in Figure 5. An accelerometer was installed on the pendulum to measure the acceleration-time history during impact. As shown in Figure 6, a data-acquisition system is setup to transfer the acceleration data in the *x*, *y* and *z* directions from the accelerometer to an 8-channel data collector and from there to a computer. The acceleration-time histories for all 63 impact tests are recorded in Excel format. This history is used to calculate the velocity-time and eventually the displacement-time histories. The force is calculated based on the mass multiplied by the measured acceleration. Eventually, a force-displacement history is obtained from all 63 impact cases. The area under these curves represented the work done, in other words, the energy absorbed by the post-soil interaction.

Table 3. Details of guardrail posts tested (C type).

Post Designation	PED (mm)	Soil Characterization	Code
C120x60x4	600	H (Hard)	H-600
	650		H-650
	700		H-700
	750		H-750
	800		H-800
	850		H-850
	900		H-900
	600	M (Medium Hard)	M-600
	650		M-650
	700		M-700
	750		M-750
	800		M-800
	850		M-850
	900		M-900
	600	S (Soft)	S-600
	650		S-650
	700		S-700
	750		S-750
	800		S-800
	850		S-850
	900		S-900

Table 4. Details of guardrail posts tested (H type).

Post Designation	PED (mm)	Soil Characterization	Code
H150x90x6	700	H (Hard)	H-700
	800		H-800
	900		H-900
	1000		H-1000
	1100		H-1100
	1200		H-1200
	1300		H-1300
	700	M (Medium Hard)	M-700
	800		M-800
	900		M-900
	1000		M-1000
	1100		M-1100
	1200		M-1200
	1300		M-1300
	700	S (Soft)	S-600
	800		S-650
	900		S-700
	1000		S-750
	1100		S-800
	1200		S-850
	1300		S-900

Table 5. Details of guardrail posts tested (S type).

Post Designation	PED (mm)	Soil Characterization	Code
S100x50x4.2	700	H (Hard)	H-700
	800		H-800
	900		H-900
	1000		H-1000
	1100		H-1100
	1200		H-1200
	1300		H-1300
	700	M (Medium Hard)	M-700
	800		M-800
	900		M-900
	1000		M-1000
	1100		M-1100
	1200		M-1200
	1300		M-1300
	700	S (Soft)	S-600
	800		S-650
	900		S-700
	1000		S-750
	1100		S-800
	1200		S-850
	1300		S-900

Figure 4. Installation of posts in soil.

Figure 5. Pendulum test device used in dynamic impact tests with three dimensional accelerometer.

Figure 6. Data acquisition setup used during dynamic pendulum testing (1) data cable between accelerometer and data collector box, (2) 8-channel data collector, (3) recording data in a computer.

3 TEST RESULTS AND DISCUSSION

3.1 Visual inspections

A total of 63 impact tests were performed using the pendulum device. Each of the test results was recorded visually and analytically. The general views for the different soil conditions (soft-S, medium hard-M and hard-H soil) after the tests where C-type posts were used are given in Figure 7. And then a qualitative evaluation of all the tests is presented in Tables 6-8. In general, when an insufficient PED is used the posts exhibited an upwards movement and in some cases were almost completely removed from the soil. On the other hand, when sufficient PED is used, the posts remained in the soil with minimal upward motion and in some cases post buckling was observed.

Table 6. Qualitative evaluation of the pendulum test results (C-type post).

PED (mm	Soil Stiffness		
	Hard (H)	Medium hard (M)	Soft (S)
600	1 The post moved upwards in the ground, but was not completely removed from the soil. The soil body is collapsed. The pendulum slowed down after impact	Same as H-600	The post moved upwards in the ground and completely removed from the soil. The soil body is collapsed. The pendulum movement continued.
650	The post movement in the soil is less than H-600, but the soil body is collapsed. The pendulum stopped after the impact.	Same as M-600	Same as S-600
700	The post's upwards movement is not observed and minimal soil movement occurred. The post-soil interaction and energy absorption are acceptable.	Somewhat improvement compared to the M-650 case. The soil body is collapsed. The pendulum stopped after the impact.	Same as H-600
750	Due to sufficient PED, slight post buckling is observed. Post-soil interaction and energy absorption are acceptable.	Same as H-700	Same as M-700
800	Post buckling becomes more visible. Post-soil interaction and energy absorption is acceptable.	Same as H-750	Same as H-700
850	Same as H-800	Same as H-800	Same as H-800
900	Same as H-800	Same as H-800	Same as H-800

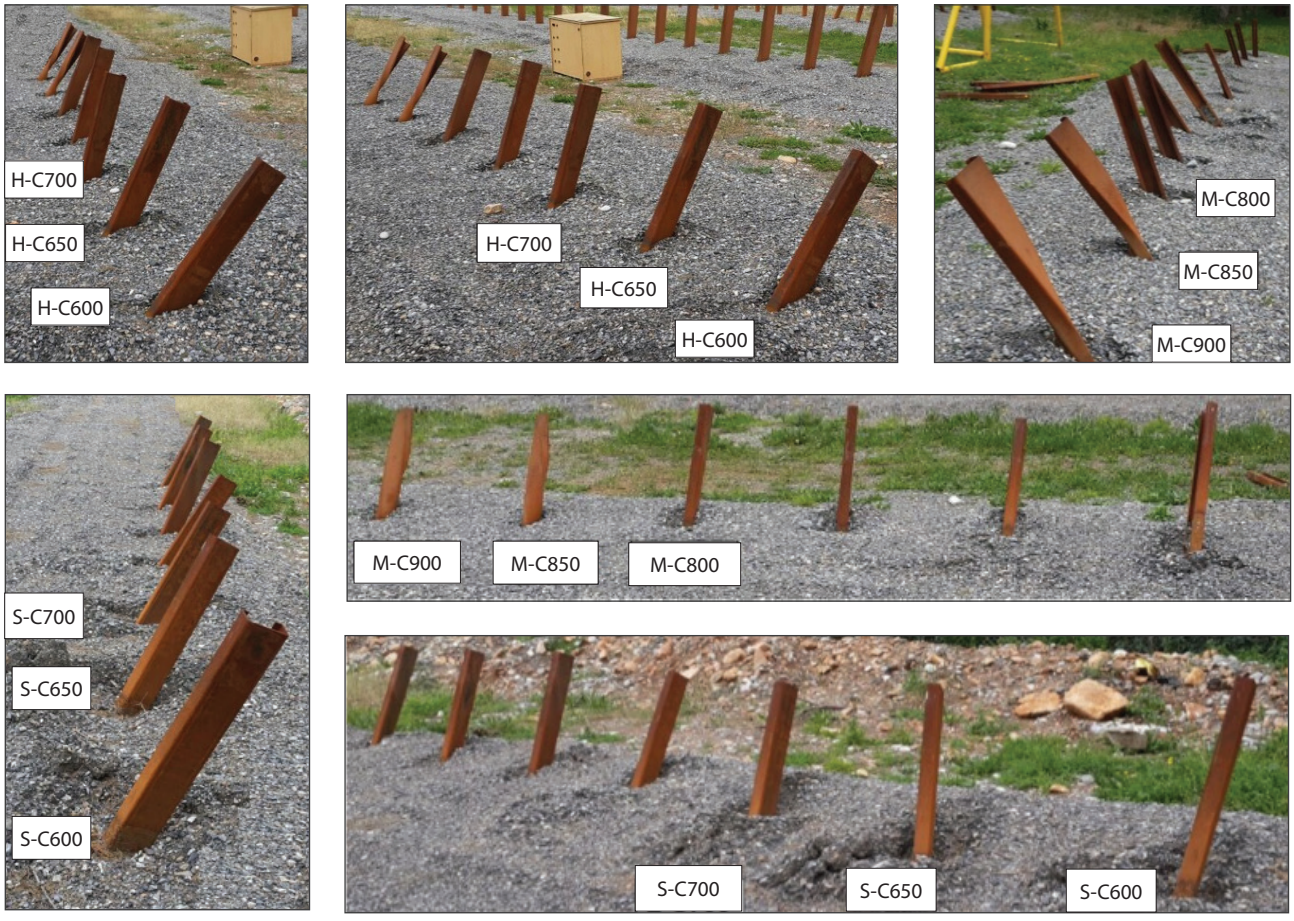

Figure 7. General views of the soil for C-type posts after the impact tests.

Table 7. Qualitative evaluation of the pendulum test results (H-type post).

PED (mm	Soil Stiffness		
	Hard (H)	Medium hard (M)	Soft (S)
700	The post moved upwards in the ground but was not completely removed from the soil. The soil body is collapsed. The pendulum movement continued.	The post moved upwards in the ground and the soil body collapsed. The pendulum movement continued.	The maximum post movement was observed and the soil body collapsed. The pendulum movement continued.
800	The post movement in the soil is less than H-700, but the soil body is collapsed. The pendulum stopped after the impact.	The post movement in the soil is less than M-700 and the soil body is collapsed. The pendulum stopped after the impact.	The post movement in the soil is less than S-700 and the soil body is collapsed.
900	Due to sufficient PED, slight post buckling is observed. Post-soil interaction and energy absorption are acceptable.	Due to sufficient PED, slight post buckling is observed. Post-soil interaction and energy absorption are acceptable.	Due to sufficient PED, slight post buckling is observed. The post movement in soil is great compared with hard and medium-hard soil types.
1000	Post-soil interaction and energy absorption are acceptable.	Same as H-1000	Same as H-1000
1100	Same as H-1000	Same as H-1000	Same as H-1000
1200	Same as H-1000	Same as H-1000	Same as H-1000
1300	Same as H-1000	Same as H-1000	Same as H-1000

Table 8. Qualitative evaluation of the pendulum test results (S-type post).

PED (mm	Soil Stiffness		
	Hard (H)	Medium hard (M)	Soft (S)
700	The post moved upwards in the ground, but was not completely removed from the soil. The soil body is collapsed. The pendulum movement continued.	Same as H-700	The maximum post movement was observed and the soil body collapsed. The pendulum movement continued.
800	The post movement in the soil is less than H-700, but the soil body collapsed. The pendulum stopped after impact.	Same as H-800	The post movement in the soil is less than S-700 and the soil body collapsed. The pendulum movement continued.
900	The post's upwards movement is not observed and minimal soil movement occurred. Post-soil interaction and energy absorption are acceptable.	Same as H-900	The post movement in the soil is less than S-800, but the soil body is collapsed. The pendulum stopped after the impact.
1000	Due to sufficient PED, slight post buckling is observed. Post-soil interaction and energy absorption are acceptable.	Same as H-1000	Same as H-1000
1100	Post buckling becomes more visible. Soil movement is negligible.	The post's upwards movement is not observed and minimal soil movement occurred.	Same as H-1100
1200	Post buckling becomes more visible.	Due to sufficient PED, slight post buckling is observed.	Same as M-1100
1300	Same as H-1200	Same as H-1200	Same as M-1200

3.2 Analytical Calculations

The maximum measured accelerations and the energy absorbed, calculated using the area under the force-deformation curve for all 63 impact tests, are presented in Table 9. In the pendulum test, the mass of 750kg was lifted 1.5m each time and then released free. A kinetic energy of 11.04 kJ was applied to the posts by the pendulum. This value was determined using the standard kinetic energy formula after calculating the velocity that the post had just before the impact. Compared to the energy levels applied to the guardrail systems by the vehi-

Table 9. Maximum energy absorption and acceleration calculations for the pendulum tests.

Post type	PED (mm)	Soil Stiffness					
		Hard (H)		Medium hard (M)		Soft (S)	
		Max. Energy Absorbed (kJ)	Max. Accel. (g)	Max. Energy Absorbed (kJ)	Max. Accel. (g)	Max. Energy Absorbed (kJ)	Max. Accel. (g)
C120×60×4 (C)	600	0.72	- 2.88	0.66	- 2.06	0.49	- 1.08
	650	2.93	- 4.05	2.11	- 2.90	1.77	- 2.45
	700	3.27	- 4.52	2.35	- 3.25	2.14	- 2.96
	750	4.58	- 6.33	3.29	- 4.55	2.89	- 3.99
	800	5.75	- 11.95	4.14	-10.72	3.31	- 7.93
	850	6.86	- 18.48	4.94	-16.83	4.01	- 13.54
	900	7.92	- 25.85	6.13	-24.47	5.19	- 18.87
C150×90×6 (H)	700	10.03	-34.81	9.56	-33.21	8.89	-31.65
	800	10.65	-35.05	10.12	-34.54	9.34	-32.68
	900	11.04	-35.26	10.74	-35.12	10.01	-33.84
	1000	11.04	-35.32	11.04	-35.51	10.71	-34.82
	1100	11.04	-35.45	11.04	-35.47	11.04	-35.21
	1200	11.04	-35.41	11.04	-35.61	11.04	-35.52
	1300	11.04	-35.56	11.04	-35.55	11.04	-35.49
C100×50×4.2 (S)	700	3.32	-4.59	3.07	-4.24	0.92	-1.27
	800	5.31	-7.34	5.11	-7.06	2.22	-3.07
	900	6.61	-9.14	6.39	-8.83	2.95	-4.08
	1000	7.51	-10.38	7.17	-9.91	3.61	-8.99
	1100	8.05	-18.13	7.77	-17.74	4.26	-15.89
	1200	8.44	-19.67	8.01	-18.07	6.03	-16.84
	1300	9.61	-25.28	8.31	-23.21	7.93	-21.75

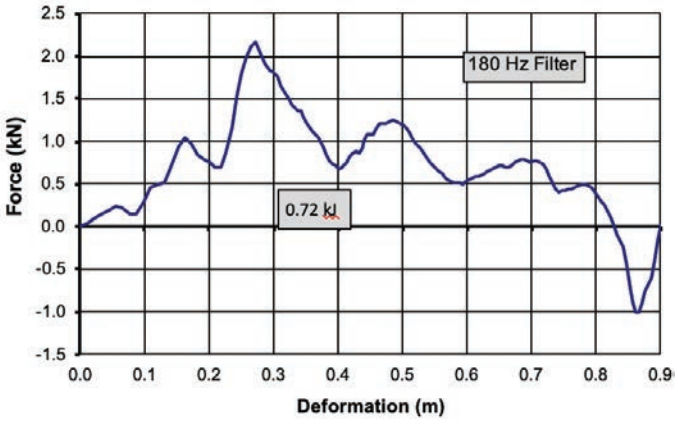

Figure 8. Typical force-deformation curve after the impact test.

cles in the actual crash tests, the 11.04 kJ is a reasonable energy level that can be used to determine the impact behavior of the post driven into the soil. The following equations were used to calculate the energy level.

$$m\,g\,h = 0.5\,m\,V^2 \qquad (1)$$

$$V = (2\,g\,h)^{0.5} = (2 \times 9.81 \times 1.5)^{0.5} = 5.43 \text{ m/s} \qquad (2)$$

$$E = 0.5\,m\,V^2 = 0.5 \times 750 \times 5.43^2 = 11.04 \text{ kJoule} \qquad (3)$$

During the impact, this energy is absorbed by the post and the absorption depends directly on the post material's strength, the PED and the soil properties. The impact of the pendulum on the posts means that all its energy transmits to the post. A typical force-deformation curve is given in Figure 8 for the C-type posts, 600mm of PED and the hard-soil condition.

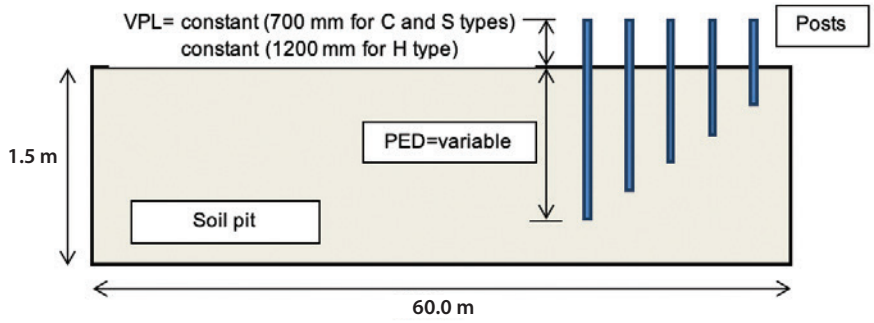

Figure 9. Cross-sections of the soil pits and the PEDs.

4 EVALUATION OF FIELD TEST RESULTS

In this study, three different post shapes, i.e., C type (C120×60×4), H type (H150×90×6) and S type (S100×50×4.2) are used. The PED ranged from 650 mm to 900 mm for the C-type posts and ranged from 700 mm to 1300 mm for the H-type and S-type posts for all three soil conditions. The visible post length (VPL) above the soil was kept constant at 700 mm for the C- and S-type posts and 1200 mm for the H-type post. Figure 9 shows cross-sections of the soil pits and PEDs.

The posts were embedded in soft, medium-hard and hard soil conditions, for which the soil properties are given above. The relations of the post embedment depth/visible post length (PED/VPL), energy-absorption capacity (EAC) for different soil (soft, medium-hard and hard) and post types (C, H and S type) are given in Figure 10. As shown in this figure, there is a linear relationship between the PED/VPL ratio and the magnitude of the energy-absorption capacity increases when the PED/VPL ratio increases for all the types of soil and post. For the C-type posts given in Figure 10a, the energy-absorption capacity increases from 4.44% to 47.01% when the PED increases from 600 mm to 900 mm in a soft-soil environment. Similarly, in the case of medium-hard soil, when the PED increases from 600 mm to 900 mm, the energy-absorption capacity increases from 5.98% to 55.53%. In the hard-soil conditions, this value increases from 6.52% to 71.74%. Similar observations are obtained for the H-type and S-type posts, given in Figure 10b and c.

The internal friction angle of the soil (ϕ) – EAC (%) relation of the C-, H- and S-type posts that embedded in soft, medium-hard and hard soils are presented in Figure 11. These relationships are given for different PED values. In these figures, the soft, medium-hard and hard soils are represented by internal friction angles of 36°, 44° and 48°, respectively. As shown in these figures there is a linear relationship between the internal fric-

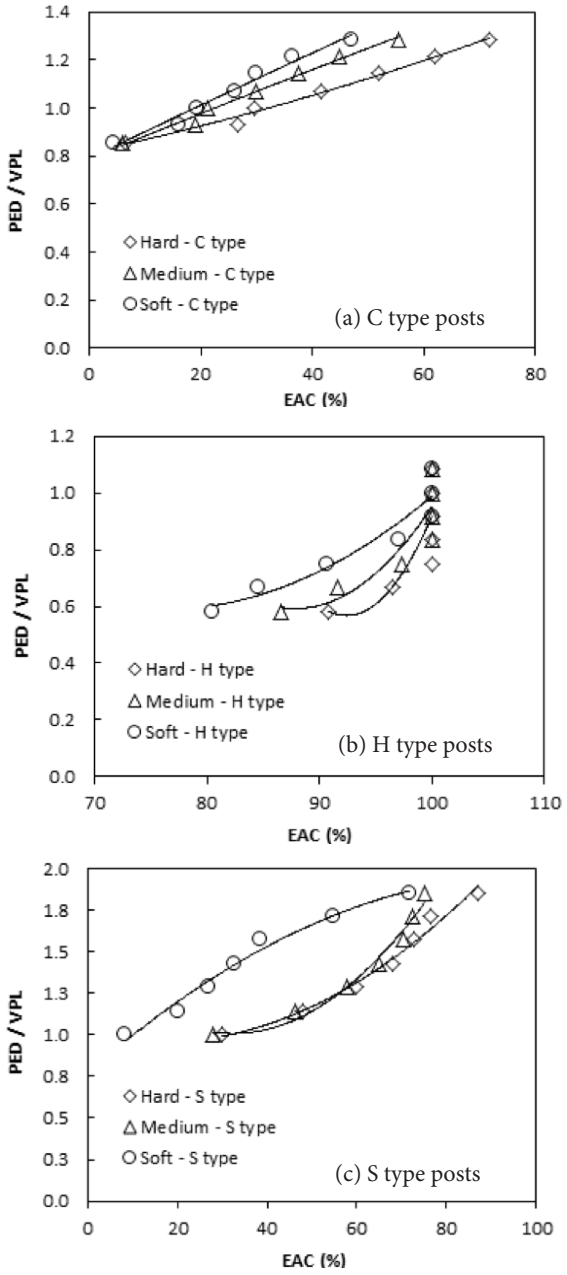

Figure 10. EAC-PED/VPL relationship according to the soil conditions.

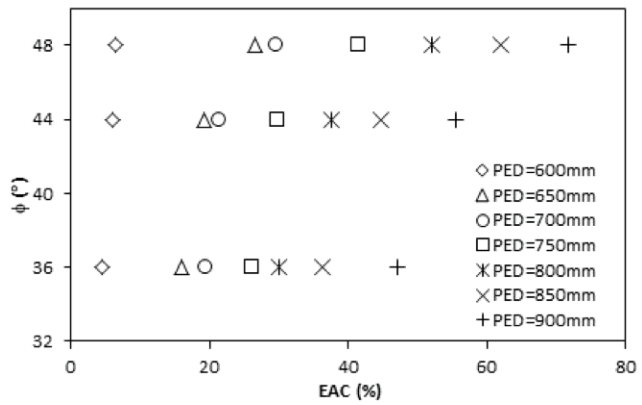

(a) C type posts

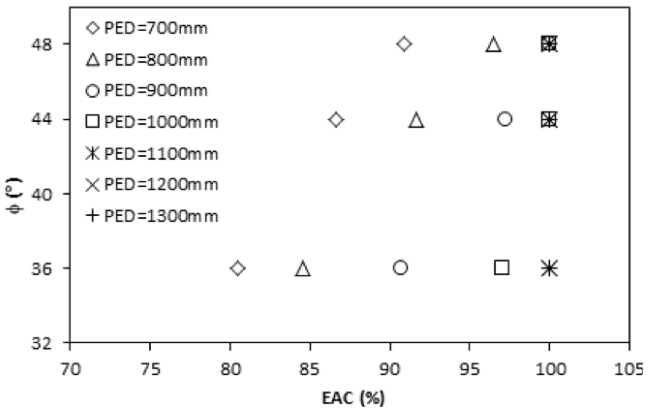

(b) H type posts

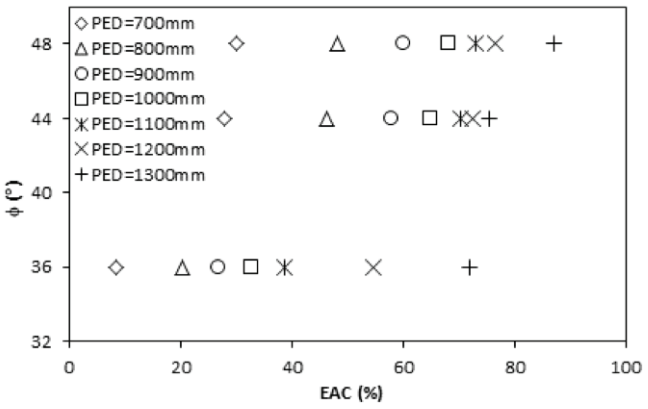

(c) S type posts

Figure 11. EAC-ϕ relationship according to the PED values.

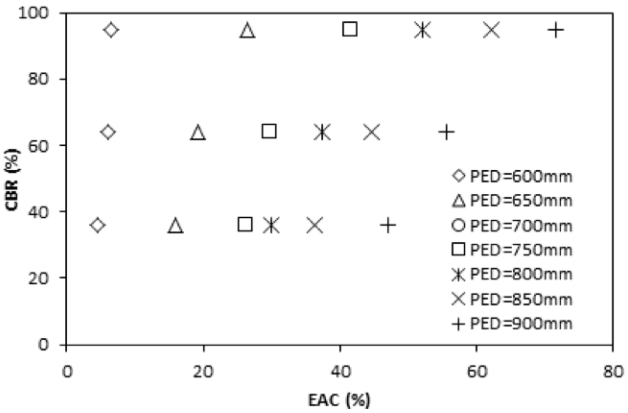

(a) C type posts

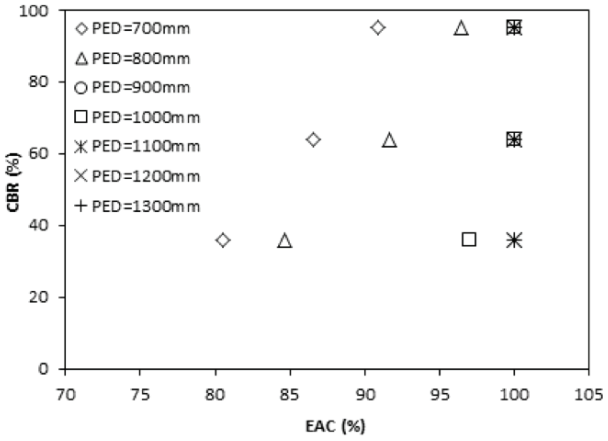

(b) H type posts

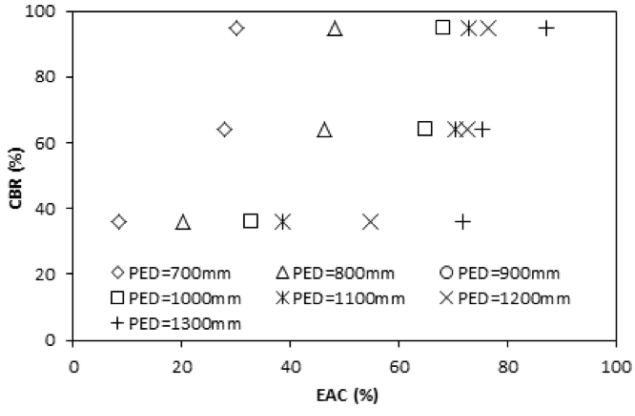

(c) S type posts

Figure 12. EAC-CBR relationship according to the PED values.

tion angle and the magnitude of the energy-absorption capacity. Note that the EAC increases when ϕ increases for all the types of soil and post. For the H-type posts given in Figure 11b, the energy-absorption capacities are 97.01%, 100.0% and 100.0%, for the soft (ϕ=36°), medium-hard (ϕ=44°) and hard (ϕ=48°) soil conditions, respectively. For the same soil stiffness (for example, ϕ=48°) the energy-absorption capacity increases with an increase in a certain value of the PED and then it remains constant. For the H-type posts, for PED values 700 mm, 1000 mm and 1300 mm, the EAS are 90.85%, 100.0% and 100.0%, respectively.

The European crash-test standard EN1317 is a performance-based standard. In other words, the impact-response behavior of the guardrail designs are considered, regardless of the guardrail material, geometry or soil properties. This study focused on this phenomenon and evaluated the safety performance of the guardrail posts when they are installed into various soil types, such as soft, medium-hard and hard. In this study it is agreed that the post behaves in a similar way to laterally loaded piles [13]. In the case of axially loaded piles, loads are transferred to the soil by shaft friction and base resistance. This total resistance resulted from the shaft resistance and end-bearing resistance, providing the equilibrium conditions. In the end-bearing piles, it is essential to have the pile base inserted into a stronger soil layer, such as dense sand, stiff clay or rock. If no such strong layer is available at the site, then the loads are carried only by the shaft friction. In the laterally loaded pile phenomenon, piles behave as transversely loaded beams. The lateral load is transferred to the surrounding soil mass by using the lateral resistance of the soil. A part or complete pile tends to shift horizontally in the direction of the applied load, causing pile bending, pile rotation or pile translation, depending on the post's stiffness, load value and soil property. The soil mass lying in the direction of the applied load generates compressive and shear stresses and strains in the soil that offers resistance to the pile movement. The soil-based results are interpreted in terms of the laterally loaded pile mechanism. In the current study, dynamic pendulum tests were performed to determine the optimum PED values for different soil conditions. Based on a total of 63 test results, the suggested optimum PED values for different types of soil and posts are given in Table 10, including the application standard. As seen clearly from Table 10, the optimum PEDs suggested in this study are smaller than the applied ones, especially in the hard and medium-hard soil conditions.

Table 10. Suggested and applied PED values.

Post	Optimum post embedment depth (PED_{opt})		
	Hard soil	Medium-Hard soil	Soft soil
	$PED_{suggested}$ / $PED_{applied}$		
C type	750mm / 950mm	850mm / 950mm	950mm / 950mm
S type	1000mm / 1200mm	1100mm / 1200mm	1200mm / 1200mm
H type	800mm / 1230mm	900mm / 1230mm	1000mm / 1230mm

Table 11 gives the amount of saving percentages for one post for each type of post and soil used. It was determined that significant savings were made, especially in C- and H-type posts and also for hard-soil conditions. Considering the optimum length in the guardrail post design, significant savings can be achieved for a mile of road. In other words, with the use of the optimum length of guardrail posts, a considerable amount of installation time, labor and material savings are expected. This study has shown that the optimum embedment depths of the guardrail posts can be decided by determining the soil properties in the light of the standard geotechnical experiments to be performed on the roads where the guardrail post is to be installed.

Table 11. Amount of savings according to PED_{opt}.

Post	Hard soil	Medium-Hard soil	Soft soil
C type	21.05%	10.53%	0.00%
S type	16.67%	8.33%	0.00%
H type	34.96%	26.83%	18.70%

5 CONCLUSIONS

In this study a series of field pendulum-impact tests were performed on soil-embedded posts to determine the optimum PED for three different soil conditions, namely, hard, medium-hard and soft soil. A pendulum device was used to perform the dynamic impact tests on C-type (C120×60×4), H-type (C150×90×6) and S-type (S100×50×4.2) posts with seven different PED values used for each type of soil. Based on the research findings, the following specific conclusions can be drawn:

- Dynamic pendulum tests proved that an increased soil stiffness resulted in a reduction in PED for the posts due to an improved post-soil interaction.
- It is determined that the posts tend to move upwards, get out of the soil quickly and thus could not provide enough resistance when the PED is insufficient.
- Soil stiffness has an important effect on the impact--response behavior of the guardrail posts. There is a linear relationship between the internal friction angle and the magnitude of the energy-absorption capacity increases when ϕ increases for all the types of soil and post. Similar behavior was observed from a CBR perspective.
- It has been determined that significant savings have been made, especially in C- and H-type posts and also for hard soil conditions.
- When comparing the optimum values with the standards, the savings obtained for hard soils can reach up to 35% for H-type posts. These savings are about 20% for C-type posts and about 15% for S-type posts.
- Considering the larger PED in similar guardrail systems in use today, designs with optimum PED will help save a considerable amount of installation time, labor and material.

Acknowledgments

The work presented in this paper was carried out with funding from TUBITAK (Scientific and Technological Research Council of Turkey), Grant No. 213M516.

REFERENCES

[1] AASHTO. 2014. Roadside design guide. American Association for State Highway and Transportation Officials. 4th Edition, Washington, D.C.

[2] Atahan, A.O., Cansız, Ö.F. 2005. Improvements to G4(RW) strong-post round-wood W-beam guardrail system. ASCE Journal of Transportation Engineering 131(1), 63-73. DOI: 10.1061/(asce)0733-947x(2005)131:1(63)

[3] Atahan, A.O., Bonin, G., Cicinnati, L., Yaşarer, H.I. 2008. Development of a crashworthy end terminal TWINY for thrie-beam guardrail. ASCE Journal of Transportation Engineering 133(4), 467-476. DOI: 10.1061/(ASCE)0733-947X(2008)134:11(467)

[4] CEN. 2017. European Crash Testing Standard EN1317. Performance classes, impact test acceptance criteria and test methods for safety barriers, Brussels.

[5] Reid, J.D. 2004. LS-DYNA simulation influence on roadside hardware. Transportation Research Board Annual Meeting, Paper No. 04-2619, Washington D.C. DOI: 10.3141/1890-04

[6] Wu, W., Thomson, R.A. 2007. A study of the interaction between a guardrail post and soil during quasi-static and dynamic loading. International Journal of Impact Engineering 34, 883-98. DOI: 10.1016/j.ijimpeng.2006.04.004

[7] Atahan, A.O. 2003. Impact behavior of G2 steel weak-post W-beam guardrail on nonlevel terrain. Heavy Vehicle Systems, A series of the International Journal of Vehicle Design 10(3), 209-223. DOI: 10.1504/IJHVS.2003.003207

[8] Marzougui, D., Mohan, P., Kan, C.D., Opiela, K.S. 2007. Performance evaluation of low tension three strand cable median barriers, Transportation Research Board Annual Meeting, Washington D.C. DOI: 10.3141/2025-03

[9] Polivka, K.A., Sicking, D.L., Faller, R.K., Bielenberg, R.W. 2000. Development of a W-beam guardrail system for use on a 2:1 Slope. Transportation Research Record 1743, 80-87.

[10] Sheikh, N.M., Bligh, R.P. 2006. Analysis of the impact performance of concrete median barrier placed on or adjacent to slopes, Report No. FHWA/TX-06/0-5210-1, Texas A&M University, Texas.

[11] Bonin, G., Cantiasani, G., Loprencipe, G., Ranzo, A., Atahan, A.O. 2009. Retrofit of an existing Italian bridge rail for H4a containment level using simulation, Heavy Vehicle Systems, A series of the International Journal of Vehicle Design 16(1/2), 258-270. DOI: 10.1504/IJHVS.2009.023864

[12] TRA. 2016. Handbook of properties of road construction materials. General Directorate of Turkish Roads, Turkish Road Association, Ankara, Turkey.

[13] Teng, T.L., Liang, C.C., Hsu, C.Y., Shih, C.J., Tran, T.T. 2016. Effect of soil properties on safety performance of Wbeam guardrail. International Conference on Advanced Material Science and Environmental Engineering (AMSEE 2016), 34-36. DOI: 10.2991/amsee-16.2016.10

[14] Zhang, Y., Ye, W., Wang, Z. 2017. Study on the compaction effect factors of lime-treated loess highway embankments. Civil Engineering Journal 3(11), 1008-1019. DOI: 10.28991/cej-030933

[15] Woo, K.W., Lee, D.W., Ahn, J.S. 2018. Impact behavior of a laterally loaded guardrail post near slopes by hybrid SPH model. Advances in Civil Engineering, Article ID 9479452, 12 pp. DOI: 10.1155/2018/9479452

[16] El-Maaty, A.E. 2016. Enhancing the CBR strength and freeze–thaw performance of silty subgrade using three reinforcement categories. Civil Engineering Journal 2(3), 73-85.

[17] Gamil, Y., Bakar, I., Ahmed, K. 2017. Simulation and development of instrumental setup to be used for cement grouting of sand soil. Italian Journal of Science and Engineering 1(1), 16-27.

[18] Hussain, S. 2017. Effect of compaction energy on engineering properties of expansive soil. Civil Engineering Journal 3(8), 610-646. DOI: 10.28991/cej-030988

NAVODILA AVTORJEM

Vsebina članka

Članek naj bo napisan v naslednji obliki:

- Naslov, ki primerno opisuje vsebino članka in ne presega 80 znakov.
- Izvleček, ki naj bo skrajšana oblika članka in naj ne presega 250 besed. Izvleček mora vsebovati osnove, jedro in cilje raziskave, uporabljeno metodologijo dela, povzetek izidov in osnovne sklepe.
- Največ 6 ključnih besed, ki bi morale biti napisane takoj po izvlečku.
- Uvod, v katerem naj bo pregled novejšega stanja in zadostne informacije za razumevanje ter pregled izidov dela, predstavljenih v članku.
- Teorija.
- Eksperimentalni del, ki naj vsebuje podatke o postavitvi preiskusa in metode, uporabljene pri pridobitvi izidov.
- Izidi, ki naj bodo jasno prikazani, po potrebi v obliki slik in preglednic.
- Razprava, v kateri naj bodo prikazane povezave in posplošitve, uporabljene za pridobitev izidov. Prikazana naj bo tudi pomembnost izidov in primerjava s poprej objavljenimi deli.
- Sklepi, v katerih naj bo prikazan en ali več sklepov, ki izhajajo iz izidov in razprave.
- Vse navedbe v besedilu morajo biti na koncu zbrane v seznamu literature, in obratno.

Dodatne zahteve

- Vrstice morajo biti zaporedno oštevilčene.
- Predložen članek ne sme imeti več kot 18 strani (brez tabel, legend in literature); velikost črk 12, dvojni razmik med vrsticami. V članek je lahko vključenih največ 10 slik. Isti rezultati so lahko prikazani v tabelah ali na slikah, ne pa na oba načina.
- Potrebno je priložiti imena, naslove in elektronske naslove štirih potencialnih recenzentov članka. Urednik ima izključno pravico do odločitve, ali bo te predloge upošteval.

Enote in okrajšave

V besedilu, preglednicah in slikah uporabljajte le standardne označbe in okrajšave SI. Simbole fizikalnih veličin v besedilu pišite poševno (npr. *v*, *T* itn.). Simbole enot, ki so sestavljene iz črk, pa pokončno (npr. Pa, m itn.). Vse okrajšave naj bodo, ko se prvič pojavijo, izpisane v celoti.

Slike

Slike morajo biti zaporedno oštevilčene in označene, v besedilu in podnaslovu, kot sl. 1, sl. 2 itn. Posnete naj bodo v katerem koli od razširjenih formatov, npr. BMP, JPG, GIF. Za pripravo diagramov in risb priporočamo CDR format (CorelDraw), saj so slike v njem vektorske in jih lahko pri končni obdelavi preprosto povečujemo ali pomanjšujemo.

Pri označevanju osi v diagramih, kadar je le mogoče, uporabite označbe veličin (npr. *v*, *T* itn.). V diagramih z več krivuljami mora biti vsaka krivulja označena. Pomen oznake mora biti razložen v podnapisu slike.

Za vse slike po fotografskih posnetkih je treba priložiti izvirne fotografije ali kakovostno narejen posnetek.

Preglednice

Preglednice morajo biti zaporedno oštevilčene in označene, v besedilu in podnaslovu, kot preglednica 1, preglednica 2 itn. V preglednicah ne uporabljajte izpisanih imen veličin, ampak samo ustrezne simbole. K fizikalnim količinam, npr. *t* (pisano poševno), pripišite enote (pisano pokončno) v novo vrsto brez oklepajev. Vse opombe naj bodo označene z uporabo dvignjene številke[1].

Seznam literature

Navedba v besedilu

Vsaka navedba, na katero se sklicujete v besedilu, mora biti v seznamu literature (in obratno). Neobjavljeni rezultati in osebne komunikacije se ne priporočajo v seznamu literature, navedejo pa se lahko v besedilu, če je nujno potrebno.

Oblika navajanja literature

V besedilu: Navedite reference zaporedno po številkah v oglatih oklepajih v skladu z besedilom. Dejanski avtorji so lahko navedeni, vendar mora obvezno biti podana referenčna številka.

Primer: »..... kot je razvidno [1,2]. Brandl and Blovsky [4], sta pridobila drugačen rezultat…«

V seznamu: Literaturni viri so oštevilčeni po vrstnem redu, kakor se pojavijo v članku. Označimo jih s številkami v oglatih oklepajih.

Sklicevanje na objave v revijah:

[1] Jelušič, P., Žlender, B. 2013. Soil-nail wall stability analysis using ANFIS. Acta Geotechnica Slovenica 10(1), 61-73.

Sklicevanje na knjigo:
[2] Šuklje, L. 1969. Rheological aspects of soil mechanics. Wiley-Interscience, London
Sklicevanje na poglavje v monografiji:
[3] Mitchel, J.K. 1992. Characteristics and mechanisms of clay creep and creep rupture, in N. Guven, R.M. Pollastro (eds.), Clay-Water Interface and Its Rheological Implications, CMS Workshop Lectures, Vol. 4, The clay minerals Society, USA, pp. 212-244..
Sklicevanje na objave v zbornikih konferenc:
[4] Brandl, H., Blovsky, S. 2005. Slope stabilization with socket walls using the observational method. Proc. Int. conf. on Soil Mechanics and Geotechnical Engineering, Bratislava, pp. 2485-2488.
Sklicevanje na spletne objave:
[5] Kot najmanj, je potrebno podati celoten URL. Če so poznani drugi podatki (DOI, imena avtorjev, datumi, sklicevanje na izvorno literaturo), se naj prav tako dodajo.

Podatki o avtorjih

Članku priložite tudi podatke o avtorjih: imena, nazive, popolne poštne naslove, številke telefona in faksa, naslove elektronske pošte. Navedite kontaktno osebo.

Sprejem člankov in avtorske pravlce

Uredništvo si pridržuje pravico do odločanja o sprejemu članka za objavo, strokovno oceno mednarodnih recenzentov in morebitnem predlogu za krajšanje ali izpopolnitev ter terminološke in jezikovne korekture. Z objavo preidejo avtorske pravice na revijo ACTA GEOTECHNICA SLOVENICA. Pri morebitnih kasnejših objavah mora biti AGS navedena kot vir.

Vsa nadaljnja pojasnila daje:

Uredništvo
ACTA GEOTECHNICA SLOVENICA
Univerza v Mariboru,
Fakulteta za gradbeništvo, prometno inženirstvo in arhitekturo
Smetanova ulica 17, 2000 Maribor, Slovenija
E-pošta: ags@um.si

INSTRUCTIONS FOR AUTHORS

Format of the paper

The paper should have the following structure:

- A Title, which adequately describes the content of the paper and should not exceed 80 characters;
- An Abstract, which should be viewed as a mini version of the paper and should not exceed 250 words. The Abstract should state the principal objectives and the scope of the investigation and the methodology employed; it should also summarise the results and state the principal conclusions;
- Immediately after the abstract, provide a maximum of 6 keywords;
- An Introduction, which should provide a review of recent literature and sufficient background information to allow the results of the paper to be understood and evaluated;
- A Theoretical section;
- An Experimental section, which should provide details of the experimental set-up and the methods used to obtain the results;
- A Results section, which should clearly and concisely present the data, using figures and tables where appropriate;
- A Discussion section, which should describe the relationships shown and the generalisations made possible by the results and discuss the significance of the results, making comparisons with previously published work;
- Conclusions, which should present one or more conclusions that have been drawn from the results and subsequent discussion;
- A list of References, which comprises all the references cited in the text, and vice versa.

Additional Requirements for Manuscripts

- Use double line-spacing.
- Insert continuous line numbering.
- The submitted text of Research Papers should cover no more than 18 pages (without Tables, Legends, and References, style: font size 12, double line spacing). The number of illustrations should not exceed 10. Results may be shown in tables or figures, but not in both of them.
- Please submit, with the manuscript, the names, addresses and e-mail addresses of four potential referees. Note that the editor retains the sole right to decide whether or not the suggested reviewers are used.

Units and abbreviations

Only standard SI symbols and abbreviations should be used in the text, tables and figures. Symbols for physical quantities in the text should be written in Italics (e.g. *v*, *T*, etc.). Symbols for units that consist of letters should

be in plain text (e.g. Pa, m, etc.).
All abbreviations should be spelt out in full on first appearance.

Figures

Figures must be cited in consecutive numerical order in the text and referred to in both the text and the caption as Fig. 1, Fig. 2, etc. Figures may be saved in any common format, e.g. BMP, JPG, GIF. However, the use of CDR format (CorelDraw) is recommended for graphs and line drawings, since vector images can be easily reduced or enlarged during final processing of the paper.

When labelling axes, physical quantities (e.g. *v*, *T*, etc.) should be used whenever possible. Multi-curve graphs should have individual curves marked with a symbol; the meaning of the symbol should be explained in the figure caption. Good quality black-and-white photographs or scanned images should be supplied for the illustrations.

Tables

Tables must be cited in consecutive numerical order in the text and referred to in both the text and the caption as Table 1, Table 2, etc. The use of names for quantities in tables should be avoided if possible: corresponding symbols are preferred. In addition to the physical quantity, e.g. *t* (in Italics), units (normal text), should be added on a new line without brackets.
Any footnotes should be indicated by the use of the superscript[1].

LIST OF references

Citation in text

Please ensure that every reference cited in the text is also present in the reference list (and vice versa). Any references cited in the abstract must be given in full. Unpublished results and personal communications are not recommended in the reference list, but may be mentioned in the text, if necessary.

Reference style

Text: Indicate references by number(s) in square brackets consecutively in line with the text. The actual authors can be referred to, but the reference number(s) must always be given:

Example: "... as demonstrated [1,2]. Brandl and Blovsky [4] obtained a different result ..."

List: Number the references (numbers in square brackets) in the list in the order in which they appear in the text.

Reference to a journal publication:
[1] Jelušič, P., Žlender, B. 2013. Soil-nail wall stability analysis using ANFIS. Acta Geotechnica Slovenica 10(1), 61-73.

Reference to a book:
[2] Šuklje, L. 1969. Rheological aspects of soil mechanics. Wiley-Interscience, London

Reference to a chapter in an edited book:
[3] Mitchel, J.K. 1992. Characteristics and mechanisms of clay creep and creep rupture, in N. Guven, R.M. Pollastro (eds.), Clay-Water Interface and Its Rheological Implications, CMS Workshop Lectures, Vol. 4, The clay minerals Society, USA, pp. 212-244.

Conference proceedings:
[4] Brandl, H., Blovsky, S. 2005. Slope stabilization with socket walls using the observational method. Proc. Int. conf. on Soil Mechanics and Geotechnical Engineering, Bratislava, pp. 2485-2488.

Web references:
[5] As a minimum, the full URL should be given and the date when the reference was last accessed. Any further information, if known (DOI, author names, dates, reference to a source publication, etc.), should also be given.

Author information

The following information about the authors should be enclosed with the paper: names, complete postal addresses, telephone and fax numbers and E-mail addresses. Indicate the name of the corresponding author.

Acceptance of papers and copyright

The Editorial Committee of the Slovenian Geotechnical Review reserves the right to decide whether a paper is acceptable for publication, to obtain peer reviews for the submitted papers, and if necessary, to require changes in the content, length or language.
On publication, copyright for the paper shall pass to the ACTA GEOTECHNICA SLOVENICA. The AGS must be stated as a source in all later publication.

For further information contact:

Editorial Board
ACTA GEOTECHNICA SLOVENICA
University of Maribor,
Faculty of Civil Engineering, Transportation Engineering and Architecture
Smetanova ulica 17, 2000 Maribor, Slovenia
E-mail: ags@um.si

NAMEN REVIJE

Namen revije ACTA GEOTECHNICA SLOVENICA je objavljanje kakovostnih teoretičnih člankov z novih pomembnih področij geomehanike in geotehnike, ki bodo dolgoročno vplivali na temeljne in praktične vidike teh področij.

ACTA GEOTECHNICA SLOVENICA objavlja članke s področij: mehanika zemljin in kamnin, inženirska geologija, okoljska geotehnika, geosintetika, geotehnične konstrukcije, numerične in analitične metode, računalniško modeliranje, optimizacija geotehničnih konstrukcij, terenske in laboratorijske preiskave.

Revija redno izhaja dvakrat letno.

AIMS AND SCOPE

ACTA GEOTECHNICA SLOVENICA aims to play an important role in publishing high-quality, theoretical papers from important and emerging areas that will have a lasting impact on fundamental and practical aspects of geomechanics and geotechnical engineering.

ACTA GEOTECHNICA SLOVENICA publishes papers from the following areas: soil and rock mechanics, engineering geology, environmental geotechnics, geosynthetic, geotechnical structures, numerical and analytical methods, computer modelling, optimization of geotechnical structures, field and laboratory testing.

The journal is published twice a year.

AVTORSKE PRAVICE

COPYRIGHT

ODGOVORNOST

RESPONSIBILITY

9771854017001

University of Maribor
Faculty of Civil Engineering, Transportation Engineering and Architecture
www.fgpa.um.si

University of Ljubljana
Faculty of Civil and Geodetic Engineering
Faculty of Natural Sciences and Engineering
www.fgg.uni-lj.si
www.ntf.uni-lj.si

SLOVENSKO GEOTEHNIŠKO DRUŠTVO
SLOVENIAN GEOTECHNICAL SOCIETY
www.sloged.si

SLOVENSKO DRUŠTVO ZA PODZEMNE GRADNJE
SLOVENIAN SOCIETY FOR UNDERGROUND STRUCTURES
www.ita-slovenia.si